Nuclear Magnetic Resonance Experiments using Laser-Polarized Noble Gas

A thesis presented

by

Glenn Patrick Teen Chung Wong

to

The Department of Physics

in partial fulfillment of the requirements

for the degree of

Doctor of Philosophy

in the subject of

Physics

Harvard University

Cambridge, Massachusetts

June 2001

Advisor: Dr. Ronald Walsworth Author: Glenn Patrick Teen Chung Wong

Nuclear Magnetic Resonance
Experiments using Laser-Polarized Noble Gas

Abstract

Three different nuclear magnetic resonance (NMR) experiments using laser-polarized noble gas are reported. The first experiment demonstrates the feasibility of fast low magnetic field ($\sim$ 20 G) magnetic resonance imaging (MRI) with comparable resolution and signal-to-noise of conventional high magnetic field ($\sim$ 1 T) MRI. In addition, advantages of low field imaging over high field imaging are shown for certain applications. The second experiment uses NMR to observe the phenomenon known as "persistence" (i.e., the probability that a spin has not changed sign up to time t) in the diffusion of laser-polarized noble gas. The result obtained is consistent with theory and numerical simulations, and is the first measurement of persistence in 1-D diffusion in any system. The final NMR experiment examines the spin relaxation of polarized ^{129}Xe in coated glass cells. In particular, a "double resonance" method is employed to enhance the coupling between ^{1}H atoms in the surface coating and ^{129}Xe adsorbed onto the surface.

Contents

Acknowledgments

We must remember that intelligence is not enough. Intelligence plus character – that is the goal of true education. The complete education gives one not only power of concentration but worthy objectives upon which to concentrate. The broad education will, therefore, transmit to one not only the accumulated knowledge of the race but also the accumulated experience of social living.

– Martin Luther King, Jr.

First, I would like to thank my advisor Ron Walsworth, who has provided me with unflagging support, guidance, and inspiration. His enthusiasm and commitment to my research has been steadfast, and I am very grateful for the opportunity to learn and work with him. I am also indebted to the numerous scientists in our group who have helped me at various stages of my graduate career. Eddie Oteiza and Rick Stoner shared with me their technical expertise and scientific knowledge. Ross Mair taught me the elegance of NMR "choreography" and kept me amused with his dry wit. Ching-Hua Tseng and David Phillips have been, and will continue to be, both outstanding scientific mentors and good friends. And apart from our research group, I am fortunate to have had outstanding collaborators and mentors to work with, such as David Cory at MIT. Many thanks to you all.

Down in the trenches, I am lucky to share the company of some outstanding students. Leo Tsai and Ruopeng Wang have been great to work with, and I want to especially thank them for their assistance and patience over the past year. David Bear also deserves special note as a colleague and friend; I have sorely missed his company in the year since his graduation, and look forward to joining him in "the world beyond the Ph.D." I am also indebted to Marc Humphrey – he has gone beyond the call of duty to bring me my usual Friday lunch of Bangkok Fried Rice even as I write this.

Outside of the lab, I have been enriched by many experiences I have had as a Resident Tutor at Eliot House. I am incredibly fortunate to be part of this wonderful community, and am indebted to Steve Mitchell and Kristine Forsgard for inviting me in and leading the House so well for so many years. I count many friends among the staff, tutors, and students, and couldn't possibly name them all here. They have all contributed so much to my happiness and interests over the course of my graduate studies, and I recall with fondness many light-hearted and serious meals in the dining hall, IM sports triumphs and defeats, moments of great human kindness, and the infrequent party that I had the duty, but not necessarily the joy, of breaking up. To those at Eliot House, I hope to show my appreciation in a fashion more fitting than a written statement found in a Ph.D. thesis; nonetheless, they deserve mention and thanks here for the role they played in my graduate experience.

I would like to end by acknowledging the role my family and friends have played. "Uncle Jack" (Professor John Mitchell of UVA) encouraged me to pursue a career in physics many years ago, and I would not be writing this dissertation were it not for his wisdom and belief in my abilities. Nor would I have completed my Ph.D. without the full and unwaivering love and support of my family. My parents have been especially supportive, and I hope they take my accomplishment as an extension of their own. Finally, my deepest thanks go to my wife Harriet. For all your understanding and patience, I am deeply grateful and forever yours.

List of Figures

List of Tables

Chapter 1

Introduction

In this chapter, I describe the development of laser-polarized noble gas nuclear magnetic resonance (NMR) and magnetic resonance imaging (MRI) applications. In particular, I review the early efforts to polarize noble gases, highlight the features that make laser-polarized noble gases unique for NMR and MRI experiments, and survey the rich variety of research in the field. Within this context, I describe and motivate the research presented in this dissertation.

For typical NMR or MRI experiments, the polarization P of nuclear spins relies on the thermal Boltzmann distribution; in the high temperature limit where $k_B T \gg \mu B$,

$$P \approx \mu B / k_B T \tag{1.1}$$

where μ is the nuclear magnetic moment, B is the applied magnetic field, k_B is Boltzmann's constant, T is the temperature, and a spin-1/2 nuclei is assumed. For ^{1}H at a field of 1.5 tesla (a common field strength used in clinical MRI), $P \sim 0.00051\%$. Nonetheless, such small polarization yields detectable signals in relatively dense media such as proton-rich H_2O (for example, standard MRI scans used by

doctors and radiologists essentially map the proton density within the body, and thus pick out fluids and tissues). In contrast, gases are typically 1000× less dense than liquids and solids, and have been infrequently used for NMR purposes. Optical pumping techniques that enhance the polarization of noble gases by 4 to 5 orders of magnitude have therefore caused a great deal of recent interest, spurring researchers to develop applications that could benefit from such novel NMR nuclei.

Among the many distinct advantages that polarized noble gas NMR offers are the independence of polarization on the applied magnetic field and the rapid diffusion of the gas. Both of these characteristics are important for the research presented in this dissertation: the first allowed us to perform MRI of laser-polarized ^{129}Xe at a magnetic field 700× smaller than that of standard clinical scanners, thus obviating the need for a superconducting magnet. The second property allowed us to make the persistence measurement described in Chapter 5.

Optical pumping of noble gases and NMR/MRI are well established research fields; however, it was only recently that they have been combined in an especially fruitful manner. In particular, it is a combination of both *imaging* and *multidisciplinary* applications that have led to a much broader interest in using polarized noble gases for NMR/MRI experiments[1], and in the remainder of this chapter I briefly recount some of the steps leading to the present research efforts.

1.1 Review: optical pumping and noble gases

In 1960, Bouchiat, Carver, and Varnum reported the first demonstration of enhanced ^{3}He nuclear polarization due to spin exchange with optically pumped rubidium (Rb) [1]. Although the achieved polarization was $\sim 0.01\%$, it was four orders

[1] One could also argue that the availability of affordable high-power diode lasers at useful wavelengths has also been a contributing factor.

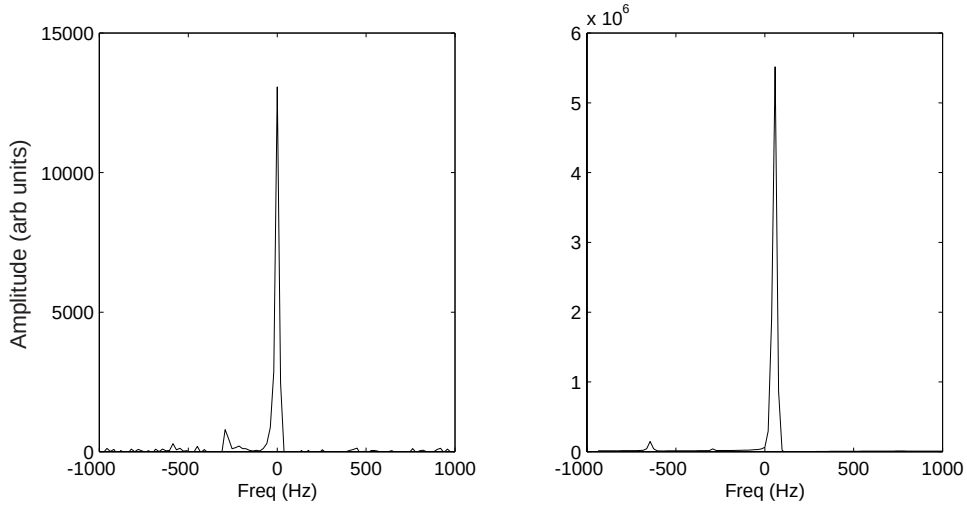

Figure 1.1: Comparison between thermal and laser-polarized ^{129}Xe spectra at 4.7 T (^{129}Xe Larmor frequency $\sim$ 55.345 MHz). Both were acquired from similar samples of 90% enriched ^{129}Xe gas (3 atm, $\sim$ 300 cc) with identical acquisition parameters. For the thermal spectrum on the left, a 90° flip angle was used; for the polarized sample, only a 10.5° flip angle was used. Nonetheless, the polarized sample yields $\sim 400\times$ more signal with the smaller flip angle. At 4.7 T, $P_{thermal\ Xe} \sim 0.00045\%$ while in this case, $P_{polarized\ Xe} \sim 1\%$. The small peak on the left of each plot is the zero frequency (DC) artifact (the x axes have been rescaled so that the gas peaks are centered at 0 Hz).

of magnitude greater than the thermal Boltzmann distribution at their operating magnetic field strength (123 G) and was readily detectable via NMR techniques. Soon thereafter, Colegrove, Schearer, and Walters demonstrated that enhanced ^{3}He nuclear polarization was possible by metastability exchange with optically pumped metastable ^{3}He [2]; furthermore, they achieved much higher polarizations ($\sim$ 40%) than previously obtained [3, 4]. A key difference, however, is that metastable optical pumping requires low ^{3}He pressures ($\sim$ few Torr), and mechanical compression of the gas after polarization to reach useful densities ($\sim$ few hundred Torr). On the other hand, spin exchange optical pumping can be performed with high ($\sim$ few thousand Torr) pressures.

Since then, there has been comprehensive research – both theoretical and experimental – to further our understanding of the nuclear polarization process and its application to other nuclei. For example, it was initially believed that spin exchange between ^{3}He and Rb occurred as a result of a dipolar coupling; that view was later corrected when Gamblin and Carver showed it is the scalar hyperfine interaction between the nuclear and electronic spins which results in the larger-than-expected interaction cross sections observed [5].

In 1965, Herman calculated spin exchange cross sections between optically pumped Rb and a variety of "foreign gas nuclei" [6], but it wasn't until 1978 that Grover experimentally polarized noble gas nuclei other than ^{3}He (namely, ^{21}Ne, ^{83}Kr, ^{129}Xe, and ^{131}Xe) via spin exchange [7]. In the last three decades, basic understanding of the spin exchange polarization process has been expounded by Happer and colleagues in a number of papers (e.g., [8–10]). Experimentally, much of the work has focussed on polarized ^{3}He and ^{129}Xe, since they possess spin-1/2 nuclei and are easily detectable using NMR techniques. Chapter 2 of this dissertation describes our present understanding of spin exchange optical pumping and presents the experimental details for polarizing noble gases.

The *use* of polarized gases has long been dominated by the nuclear physics community. In particular, it was recognized very early that a highly polarized sample of ^{3}He gas would be useful for nuclear scattering experiments [11]. That is because the spin-singlet state of ^{3}He (where the proton spins are anti-aligned) accounts for $\sim$ 90% of the ^{3}He ground state; thus a polarized ^{3}He nucleus is effectively a polarized neutron, and is ideal as both a target to probe electromagnetic structure of the neutron and as a neutron beam polarizer/analyzer (e.g., [12]).

More recently, polarized noble gases have been used for a number of precision physics experiments. For example, in 1990 Chupp and Hoare tested the linearity of

quantum mechanics by observing the coherences between the four Zeeman sublevels of polarized ^{21}Ne [13]. In 1996, a collaboration between our group and Professor Chupp at the University of Michigan demonstrated a two-species (^{129}Xe and ^{3}He) noble gas maser which could be used to search for an electric dipole moment in ^{129}Xe [14, 15]; such a device was later used by our group to place the best limit to date on violations of Lorentz symmetry and CPT for the neutron [16].

1.2 Breaking out of physics: NMR applications

Figure 1.2: MRI of laser-polarized ^{3}He in normal human lung. Courtesy of the University of Virginia.

In the last decade, there has been a dramatic surge of interest in the study and use of polarized noble gases *outside* of the traditional physics community. One

explanation for this trend is that the NMR community has recognized the utility of such highly-polarized nuclei in performing a variety of experiments that had been previous difficult or impossible to perform using only "thermally" polarized nuclei[2]. As early as 1990, multidisciplinary groups such as Alex Pines' at UC Berkeley had begun to use polarized ^{129}Xe as a means to study amorphous materials via NMR spectroscopy [17]. In 1994, Albert *et al.* published the first MRI of polarized ^{129}Xe injected into mouse lungs [18]. This sparked the imagination of a number of scientists from different fields and introduced polarized noble gases into a wider range of NMR applications that now include chemistry, materials science, and biomedical research. One of the most exciting prospects is in clinical human lung imaging. On-going research and clinical trials are proving that polarized gas lung imaging can aid doctors in diagnosing lung diseases such as Chronic Obstructive Pulmonary Disease (COPD), one of the leading causes of death in the United States. Figure 1.2 shows an example of a healthy lung image using polarized ^{3}He; such an image offers resolution unparalleled by any other clinical lung imaging method to date.

Much of the interest using polarized noble gases has focussed on two isotopes in particular: the spin-1/2 species ^{3}He and ^{129}Xe. Tables 1.1 and 1.2 list the unique properties that distinguish them from other common NMR nuclei such as ^{1}H or ^{13}C.

These different properties have prompted the many recent multidisciplinary NMR applications of polarized noble gases. For example, rapid gaseous diffusion has led to novel work in our group to measure the *tortuosity* (i.e., inter-pore connectivity) of porous media, which has been heretofore impossible with liquid-based NMR methods [19]. The large chemical shift of ^{129}Xe when it dissolves into liquids

[2]Polarization due to a Boltzmann distribution is considered "thermal"; nuclei with enhanced polarization due to optical pumping techniques have been variously labeled as "laser-polarized," "hyperpolarized," or simply "polarized." All three labels are used interchangeably in this dissertation.

- ^{3}He and ^{129}Xe are both stable, spin-1/2 nuclei
  - Inert and weakly interacting
  - long longitudinal (T_1) relaxation times
- Gaseous at room temperature
  - rapid diffusion ($\sim 1000\times$ larger diffusion coefficient than liquids)
  - fills pores and cavities easily
- ^{129}Xe exhibits a large chemical shift ($\sim$ 200 ppm) in certain environments
- Can be polarized via optical pumping techniques
  - in a non-flowing system, nuclear polarization is non-renewable; hence requires new NMR techniques
  - does not require large applied magnetic field to achieve detectable signal

Table 1.1: Unique properties of the noble gases ^{3}He and ^{129}Xe for NMR applications

Isotope	Larmor Frequency (MHz/T)	Natural Abundance (%)	Magnetic Moment (μ_N)
^{1}H	42.577	99.984	2.79270
^{3}He	32.434	1.3×10^{-4}	-2.1274
^{13}C	10.705	1.108	0.70216
^{129}Xe	11.78	26.24	-0.7726

Table 1.2: Properties of selected spin-1/2 nuclei

or tissues allowed our group and collaborators to track the temporal dynamics of inhaled ^{129}Xe as it passed into living tissue [20]; similarly, Swanson *et al.* have utilized the chemical shift to selectively image polarized ^{129}Xe as it enters different organs such as the brain [21]. There is also a large chemical shift when Xe condenses into a liquid, and in our group we have successfully imaged both the liquid and gaseous phases of Xe in samples near the boiling point and undergoing convection [22, 23]. And as a final example, Pines' group has demonstrated that it is possible to transfer a fraction of the high ^{129}Xe polarization to other spin-1/2 nuclei through internuclear dipole interactions; for example, polarized ^{129}Xe dissolved in benzene results in an enhanced ^{1}H NMR signal [24, 25].

1.3 Rethinking NMR for polarized noble gases

Although NMR and MRI are rather mature fields, using such "exotic" nuclei as polarized ^{3}He and ^{129}Xe has required a rethinking of standard NMR techniques. One particularly challenging aspect of these gases is the non-renewable nature of the polarization. In order to obtain an NMR signal, an experiment effectively depletes some fraction of the gas polarization; when enough experiments are performed, the gas polarization returns to its near-zero thermal polarization. However, unlike thermally-polarized samples, relaxation does not return a polarized gas to its initially high polarization. This is an important factor when designing the so-called "pulse-sequences" which guide an NMR experiment. For many standard NMR measurements, only slight modifications are required to make the pulse sequences suitable for the finite polarization available. However, in other cases researchers have come up with creative new pulse sequences to avoid restrictions imposed by finite polarization or to exploit the highly polarized nature of these gases. For example, Peled *et al.* have shown it is possible to make a diffusion measurement with only a single excitation pulse applied to a sample of polarized gas [26]. Another example is described in Chapter 5 of this dissertation, where I describe a cumulative k-space encoding scheme to create "quasi-random" patterns in polarized noble gases, which can then be imaged in real-time and analyzed to determine a diffusive persistence exponent.

In addition to pulse sequence modification, NMR hardware has also required adaptation to work with polarized noble gases. With commercial magnets and scanners, this has included the straightforward reconfiguring of the frequency synthesizers and computer console to operate at the appropriate Larmor frequencies of the noble gas nuclei. What is slightly more difficult is constructing (or purchasing)

an appropriately tuned radio-frequency (RF) coil for excitation pulse transmission and signal detection (e.g., in appendix A I present the design of a transverse solenoid coil tuned to 55.34 MHz – the ^{129}Xe NMR frequency at 4.7 T – which was used for the persistence experiments).

Another important and special feature of polarized noble gas is that it does not need a large applied magnetic field to create a detectable magnetization. Hence, NMR and MRI experiments can be performed without the use of commercially available superconducting magnets. Chapters 4 and 6 describe a low field magnet and associated NMR instrumentation constructed in our lab. With this magnet, we have demonstrated the ability to produce high quality images of polarized noble gases and explored some of the advantages of operating at this relatively low field strength. Double resonance experiments described in Chapter 6 were also performed using our low field magnet.

1.4 Dissertation overview

In the chapters that follow, I describe the theory and practice of polarized noble gas NMR and the experimental efforts I have undertaken. In particular, Chapter 2 summarizes the basics of spin exchange optical pumping, from the present theoretical understanding to practical aspects of its realization in the lab. An important component of this topic is the availability (and affordability) of high power laser diode arrays which provide our polarizing light, and a section is devoted to the characterization studies we performed on our high power ($\sim$ 15 W) lasers.

As mentioned earlier, many standard NMR and MRI pulse sequences have been modified to work with polarized noble gas. In Chapter 3, I describe some of these modified pulse sequences.

Chapter 4 details the development and demonstration of low field MRI with polarized noble gas. In particular, I describe both the enabling technology and experimental results, which include the first images at low field of a biological sample (excised rat lungs) and investigations of radiation damping in low-field NMR experiments. Furthermore, I compare and contrast this mode of imaging to typical high field proton imaging and suggest potential future benefits.

In Chapter 5, I summarize our diffusive persistence measurement. Persistence is an idea first introduced by the statistical physics community to ascertain the probability that a given spin remains unchanged (i.e., "persists") while undergoing stochastic processes in an initially random environment. Much of the literature on this subject has been theoretical in nature, indicating a universal power-law behavior, with the exponent depending on the system dimensionality and the specific stochastic process. To date, only a small handful of experiments have sought to observe persistence. Our results are both the first to be made on a diffusive system and a 1-D system. Included in this chapter is an explanation of the "quasi-random" encoding sequence developed for the persistence measurement and the "k-space" formalism that is useful for understanding this and other NMR techniques. Numerical simulations to test model the NMR experiment are also presented.

Finally, Chapter 6 describes a novel double resonance experiment that probes the coupling between wall coating protons and polarized ^{129}Xe. By matching the Rabi frequency of ^{1}H to the Larmor frequency of ^{129}Xe, we are able to enhance the ^{129}Xe relaxation rate and show that ^{1}H-^{129}Xe dipolar coupling is a contributing relaxation mechanism. However, contrary to expectations it is not the *dominant* relaxation mechanism, and we discuss possible explanations for this surprising result.

Chapter 2

Polarizing Noble Gases via Spin Exchange Optical Pumping

This chapter describes the nuclear spin polarization of the spin-1/2 noble gases ^{3}He and ^{129}Xe via spin exchange with optically pumped rubidium (Rb) vapor. The dominant determinants of this process are the flux of resonant D1 photons, the rate of spin-exchange, and the rates of various relaxation mechanisms. For reference, Figure 2.1 shows the "leaky bucket" model occasionally used to describe spin exchange optical pumping[1]. Although obviously simplified, this model captures the essence of the process. In particular, the net polarization of both the Rb valence electron spins and the noble gas nuclear spins depend on how much resonant (laser) light is available. In the gas mixtures we typically prepare, the Rb relaxation rate is much faster than the spin exchange rate of either ^{3}He or ^{129}Xe, so the net Rb polarization is a function of the available light and the relaxation mechanisms. On the other hand, the noble gas polarization depends not only on its own relaxation rate and the spin exchange rate, but also on the overall Rb polarization. A more detailed

[1]This model was used by Dr. Gordon Cates at a talk I heard a few years ago.

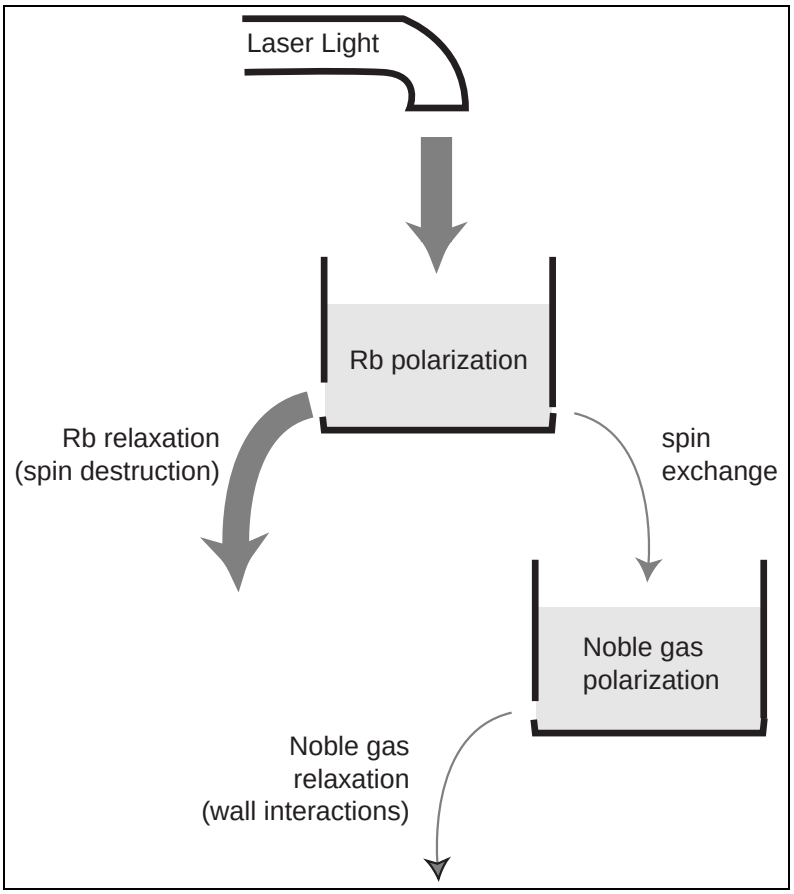

Figure 2.1: The "Leaky Bucket" model of spin exchange optical pumping. This cartoon shows the basic relationships between the available photons, spin exchange, and relaxation mechanisms.

description of the polarization process and the dominant relaxation mechanisms are the focus of sections 2.1 and 2.2.

The practical realization of spin exchange optical pumping are described in sections 2.3.1 and 2.3.2 of this chapter, including characterization studies of the high-power laser diode arrays (LDAs) used in the laboratory and preparation procedures for the glass cells used to contain the gas mixtures.

For the interested reader, Professor William Happer of Princeton University is widely regarded as the authority on the topics covered in this chapter, and a number

of reviews by him and his colleagues delve into the spin exchange optical pumping process in much greater detail (i.e., [8–10, 27]).

2.1 Optical pumping of Rubidium

In our experiments, Rb is polarized by depopulation optical pumping. For example, circularly polarized σ^+ light resonant with the Rb D1 transition (794.7 nm) is absorbed only by atoms with $m_s = -\frac{1}{2}$; however, the excited state decays back into both m_s states ($\pm\frac{1}{2}$). Consequently, over time the $m_s = -\frac{1}{2}$ state is depleted and the atom is polarized in the $m_s = +\frac{1}{2}$ state. In effect, the angular momentum of the photons is transferred to Rb, resulting in a polarized electron spin.

The two naturally occurring isotopes of rubidium, ^{85}Rb (72.17%) and ^{87}Rb (27.83%), have nuclear spins $I = \frac{5}{2}$ and $\frac{3}{2}$, respectively. The ground state hyperfine splittings are correspondingly 3036 MHz and 6835 MHz. As described by Wagshul [28, 29], the hyperfine interaction does not change the achievable Rb polarization; rather the nuclear spin acts as a store of angular momentum, and will slow both the pumping and relaxation processes. This "slowing factor" is unimportant in the experiments we conducted for a number of reasons. First, the densities of Xe, He, or N_2 that we typically use cause the D1 line to be broadened over 20 GHz[2], which is broader than the hyperfine splittings mentioned above. Similarly, the laser diode arrays we used emit light with an equivalent linewidth of over 900 GHz, thus averaging out any hyperfine splittings. Finally, as we discuss below, the polarization of Rb is a process that occurs on millisecond timescales even with the hyperfine-induced slowing factor, while the polarization of ^{3}He and ^{129}Xe occur over tens of

[2]Buffer gases such as ^{3}He, ^{4}He, N_2, and Xe are known to pressure broaden the Rb D1 line by $\sim$ 17.8, 18.0, 18.7, and 18.9 GHz/amagat, respectively [30]. 1 amagat is the density of an atmosphere of ideal gas at 273K, i.e., 2.689×10^{19} cm^{-3}.

minutes to hours. Any slowing of the Rb polarization is still very fast compared to the spin exchange times for the noble gases. Therefore, it is sufficient to discuss the optical pumping of Rb in terms of the electron spin m_s only.

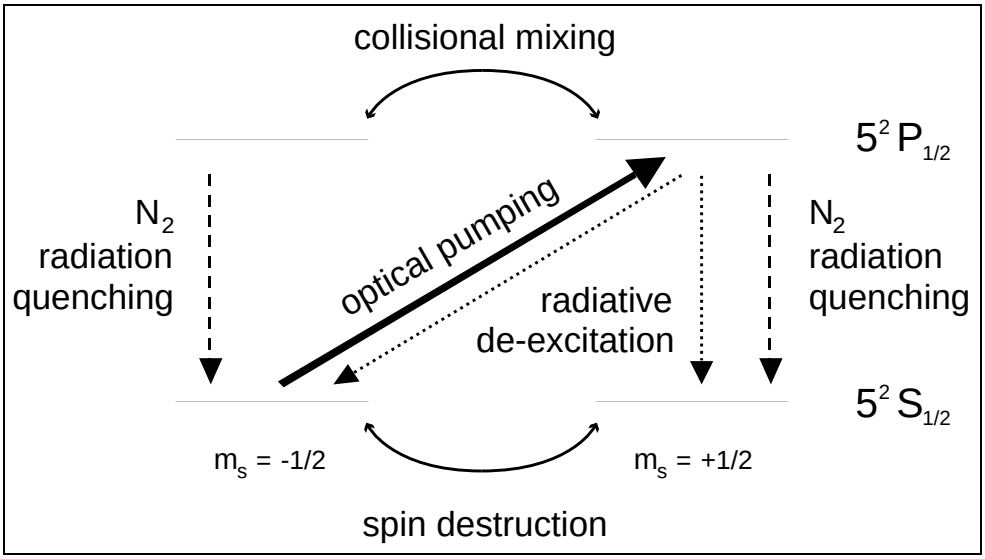

Figure 2.2: A simplified schematic of depopulation optical pumping of Rb with σ^+ light, showing the relevant pumping and relaxation pathways. Relaxation by radiative decay (dotted lines) is effectively quenched by small amounts of nitrogen (dashed lines). Spin destruction is predominantly due to a spin rotation interaction with Xe, but in the absence of that noble gas, Rb-Rb or Rb-(buffer gas) collisions are important.

Figure 2.2 shows the simplified 2-level diagram representing Rb when the hyperfine splittings are ignored. As mentioned earlier, the illustrated example of absorbing σ^+ D1 light requires that $\Delta m_s = +1$; consequently, only ground state atoms in the $m_s = -\frac{1}{2}$ state are excited. Depopulation optical pumping eventually polarizes the atom into the $m_s = +\frac{1}{2}$ ground state[3]. The Rb polarization P_{Rb} can be expressed

[3]It is straightforward to polarize Rb atoms into the $m_s = -\frac{1}{2}$ state using σ^- D1 light by reversing the polarizing optics or rotating the static magnetic field by 180°. The higher energy Zeeman level is the $m_s = +\frac{1}{2}$ state because of the negative electron gyromagnetic ratio. Thus, optical pumping with σ^+ light into the $m_s = +\frac{1}{2}$ state is most commonly used for creating a noble gas Zeeman population inversion [14]; in contrast, optical pumping with σ^- light into the $m_s = -\frac{1}{2}$ state is best suited for pulsed NMR noble gas experiments.

as

$$P_{Rb} = \frac{n_+ - n_-}{n_+ + n_-} \tag{2.1}$$

where the populations of the ground states $m_s = \pm\frac{1}{2}$ are denoted by $n_\pm$. The time dependence of P_{Rb} is given in the rate equation:

$$\frac{dP_{Rb}}{dt} = (1 - P_{Rb})\gamma_{opt} - P_{Rb}\Gamma_{Rb} \tag{2.2}$$

where γ_{opt} is the optical pumping rate and Γ_{Rb} is the spin destruction rate.

2.1.1 Optical pumping process

The optical pumping rate γ_{opt} depends on both the Rb absorption cross section $\sigma(\nu)$, and the flux of resonant photons $\Phi(\mathbf{r}, \nu)$. When Rb is in a cell with N_2, He, or Xe, $\sigma(\nu)$ is pressure broadened by roughly 18 GHz per amagat of the gas. $\Phi(\mathbf{r}, \nu)$ is position dependent due to spatial variations of the incident light as well as the attenuation of the light as it propagates in (and is absorbed by) the Rb vapor. Consequently, γ_{opt} is also position dependent, and can be expressed as follows:

$$\gamma_{opt}(\mathbf{r}) = \int \Phi(\mathbf{r}, \nu)\sigma(\nu)d\nu \tag{2.3}$$

Continuing to use the example of σ^+ optical pumping light, relaxation from the excited $5^2P_{1/2}$ $m_s = +\frac{1}{2}$ state by photon emission (radiative decay) in the absence of buffer gases returns the Rb atom back into both $m_s = -\frac{1}{2}$ and $m_s = +\frac{1}{2}$ states, with probabilities 2/3 and 1/3, respectively, as given by the Clebsch-Gordon coefficients for those transitions. Thus, it takes 3 photons on average to polarize a Rb atom into the ground $m_s = +\frac{1}{2}$ state. The situation is further complicated by the fact that the re-radiated photon is linearly polarized ($\Delta m = 0$) one third of the time and can

cause depolarization of other (polarized) Rb atoms. This "radiation trapping" can be alleviated by using a small quantity (~ 0.13 amagat[4]) of nitrogen. Collisions with N_2 then quench excited Rb more rapidly than spontaneous emission, transferring the energy into rotational and vibrational modes of the nitrogen molecule[5].

Collisions with nitrogen and other buffer gases (e.g., noble gases) also increase the optical pumping efficiency by mixing the excited P states[6]. Thus there are equal probabilities that the two ground states will be repopulated, and on average only 2 photons are required to polarize a Rb atom.

Fortunately, collisions between ground state Rb atoms and buffer gases can occur $\sim 10^9$ times before Rb is depolarized. Therefore, an additional benefit of buffer gases is that they limit the diffusion of Rb to the walls. Rb atoms that are adsorbed on the walls are considered 100% depolarized due to their relatively long interactions with nuclei on the surfaces. However, aside from a thin layer ($\sim \sqrt{D_{Rb}/\gamma_{opt}}$, where D_{Rb} is the diffusion coefficient of Rb in the buffer gases) along the walls of unpolarized Rb atoms, the bulk of the Rb vapor is shielded from any adverse wall effects.

2.1.2 Rb spin destruction

A number of mechanisms exist to depolarize the ground state of Rb, some of which we have briefly mentioned (e.g., radiation trapping and interactions with the walls). The use of a buffer gas such as N_2 negates those processes, but may lead to three-body collisions that create relatively long-lived van der Waals molecules, especially

[4] 0.13 amagat is approximately 100 Torr at room temperature.

[5] For reference, the quenching cross section of Rb due to collisions with N_2 is approximately 58 Å^2 [31]. Thus, with typical N_2 densities at optical pumping cell temperatures of ~ 100 ˚C, the quenching rate is 10^9 sec^{-1}, which is fast compared to the radiative lifetime τ_1 of the excited Rb $5^2P_{1/2}$ state ($\tau_1^{-1} = 3.6 \times 10^7$ sec^{-1} [32, 33]).

[6] Collisional depolarization cross sections for Rb 5 $^2P_{1/2}$ have been measured by Bulos and Happer for He, Ne, Ar, and Kr [34]. For He, the depolarization cross section is 23 Å^2.

between Rb and heavy noble gas atoms such as Xe. For Xe pressures below ~ 350 Torr[7], such molecules can play an important role in spin exchange and spin relaxation [9, 35, 36]. However, at the multi-atmosphere pressures we typically operate at, the lifetimes of such molecules are very short ($\mathcal{O}(10^{-11}$ sec)) [10] and their contribution to Γ_{Rb} is negligible. Thus, in our work the dominant source of Rb spin destruction is the spin-rotation interaction for a binary collision [37–39].

The Hamiltonian is simply:

$$H_{SR} = \gamma \mathbf{N} \cdot \mathbf{S} \tag{2.4}$$

where $\mathbf{N}$ is the rotational angular momentum of the colliding pair about its center of mass and $\mathbf{S}$ is the Rb valence electron spin. γ is a spin-rotation coupling constant that depends on the internuclear separation of the pair.

The spin destruction rate Γ_{Rb} can be expressed as follows:

$$\Gamma_{Rb} = \sum_X k_{SR(Rb-X)}[X] \tag{2.5}$$

where X denotes another atomic species interacting with Rb, $k_{SR(Rb-X)} = \langle \sigma_{Rb-X} \overline{v} \rangle$ is the velocity-averaged rate constant in units [cm^3/s], and $[X]$ is the number density of species X.

Table 2.1 gives a list of the spin rotation rate constants for common gases we mix with Rb. Although the Rb-Rb interaction has the largest rate constant, the densities of Rb for a typical experiment are five orders of magnitude lower than the densities

[7]Whenever I state a gas pressure, assume it is at room temperature unless otherwise specified.

[8]Bouchiat *et al.* in fact measured the Rb depolarization cross section $\sigma_{Rb-Xe} = 1.641 \times 10^{-19}$ cm^2. The value of $k_{SR(Rb-Xe)} = \langle \sigma_{Rb-Xe} \overline{v} \rangle$ given in the table is calculated with a mean relative velocity $\overline{v} = 4.4 \times 10^4$ cm/s between the Xe and Rb atoms at a typical pumping temperature of 100 ℃.

X	$k_{SR(Rb-X)}$ [cm^3/s]	*refs*
Rb	8.11×10^{-13}	*[29]*
N_2	9.38×10^{-18}	*[29]*
^{3}He	$\leq 2.29 \times 10^{-18}$	*[29]*
Xe	7.2×10^{-15}	*[39]*[8]

Table 2.1: Spin rotation rate constants of Rb and different nuclei X.

of other gases present. In situations when Xe is present in typical quantities, the term $k_{SR(Rb-Xe)}[Xe]$ dominates Γ_{Rb} and thus is the major contributor to Rb spin relaxation. Table 2.2 give some example gas cell configurations and the associated Rb spin relaxation rates.

Cell name	Densities [cm^{-3}]				Contribution to Γ_{Rb} [Hz]			
	Rb	N_2	^{3}He	Xe	Rb	N_2	^{3}He	Xe
TS2	1.0×10^{14}	3.5×10^{18}	7.3×10^{19}	–	130	33	$\leq$167	–
P-2	5.8×10^{12}	1.3×10^{19}	–	7.7×10^{19}	7	122	–	554,400
G7	1.0×10^{14}	5.1×10^{18}	1.8×10^{19}	1.4×10^{19}	130	48	$\leq$41	100,800

Table 2.2: Spin rotation rates for different experimental gas cells. Cell TS2 is a ^{3}He and N_2 filled cell used for low field magnet calibration (due to the high polarization achievable). Cell P-2 is an enriched ^{129}Xe cell used for the persistence measurements described in Chapter 5. Cell G7 is a ^{3}He-^{129}Xe cell made for future experiments. Rb densities were calculated using eq. 2.15 assuming typical cell temperatures of T=100 ℃ for pumping P-2, and T=150 ℃ for TS2 and G7.

Note that spin exchange with noble gas nuclei is also a relaxation mechanism for Rb. However, as we will see in section 2.2.1, the rates are considerably slower, and not an important contributor to the relaxation of polarized Rb.

2.2 Noble Gas Polarization

The rate equation which describes noble gas nuclear spin polarization P_{ng} via spin exchange is analogous to eq. 2.2 for Rb polarization:

$$\frac{dP_{ng}}{dt} = (P_{Rb} - P_{ng})\gamma_{SE} - P_{ng}\Gamma_{ng}. \tag{2.6}$$

As we discuss below, the spin exchange rates γ_{SE} for ^{3}He and ^{129}Xe are much slower than γ_{opt} or Γ_{SR} for rubidium optical pumping. Therefore, P_{Rb} is effectively constant during the spin exchange process, and the time evolution of P_{ng} (assuming 0 initial polarization) is given by:

$$P_{ng}(t) = \left(\frac{\gamma_{SE}}{\gamma_{SE} + \Gamma_{ng}}\right) P_{Rb}\left(1 - e^{-(\gamma_{SE}+\Gamma_{ng})t}\right). \tag{2.7}$$

Section 2.2.1 below discusses the spin exchange process and gives example values for γ_{SE}; section 2.2.2 describes some of the important relaxation mechanisms that affect the noble gas nuclear spins.

2.2.1 Spin Exchange

The transfer of angular momentum from a polarized Rb valence electron to the nuclear spin of a noble gas atom occurs via the spin-exchange hyperfine interaction, as first suggested by Herman [6]:

$$H_{SE} = -2\gamma_n\mu_n\mu_B \sum_i \left[\frac{\mathbf{I}\cdot\mathbf{S_i}}{r_i^3} - 3\frac{(\mathbf{I}\cdot\mathbf{r_i})(\mathbf{S_i}\cdot\mathbf{r_i})}{r_i^5} + \frac{8\pi}{3}\delta(r_i)\mathbf{S_i}\cdot\mathbf{I}\right] \tag{2.8}$$

where γ_n is the gyromagnetic ratio of the noble gas nuclei, μ_n and μ_B are the nuclear and Bohr magnetons, respectively, $\mathbf{I}$ is the noble gas nuclear spin, $\mathbf{S_i}$ is the

constant	^{3}He	^{129}Xe
γ_M	–	2.92×10^4 sec^{-1}
ζ	–	0.0949 ($P_{Rb} \to 1$) – 0.1791 ($P_{Rb} \to 0$)
$\langle \sigma v \rangle_{SE}$	6.7×10^{-20} cm^3/s	3.7×10^{-16} cm^3/s
refs	[40]	[36]

Table 2.3: Summary of spin exchange constants between Rb and (^{3}He, ^{129}Xe).

i^{th} electron spin (of the Rb valence electron and all noble gas electrons), and r_i is the distance from the noble gas nucleus to the i^{th} electron. The scalar Fermi contact potential (third term in eq. 2.8) is the dominant contributor to spin-exchange. Furthermore, due to the indistinguishability of the many electrons and the peak in the s-state electron wavefunction at the noble gas nucleus, there is a substantial enhancement factor η which increases in magnitude for heavier noble gases. For He and Xe, Herman originally estimated that $\eta = -7$ and -23, respectively, but a more recent calculation by Walker yields $\eta = -9.5$ and -50 [10]. In any case, it is this rather large interaction term that results in high polarization transfer to the noble gas nuclei from polarized Rb.

The spin exchange rate can be expressed as

$$\gamma_{SE} = k_{SE}[Rb] \tag{2.9}$$

where the rate constant is given by [36]

$$k_{SE} = \left(\frac{\gamma_M \zeta}{[X]} + \langle \sigma v \rangle_{SE} \right). \tag{2.10}$$

The first term is due to spin exchange in Rb-(noble gas) van der Waals molecules, and is inversely proportional to the number density of X (the third body in a molecule-forming collision, usually N_2 or Xe). Although such molecules play a negligible

Cell name	T_{pump} ($^{\circ}$C)	[Rb] (cm^3/s)	$\gamma_{SE(^3He)}$ (Hz)	$\gamma_{SE(^{129}Xe)}$ (Hz)
TS2	150	1.0×10^{14}	6.7×10^{-6}	–
P-2	100	5.8×10^{12}	–	$(2.4 - 2.5) \times 10^{-3}$
G7	150	1.0×10^{14}	6.7×10^{-6}	$(5.7 - 7.4) \times 10^{-2}$

Table 2.4: Spin exchange rates for different experimental gas cells. See Table 2.2 for gas mixtures used in cells TS2, P-2, and G7.

role in Rb relaxation at high buffer pressures (as mentioned in sec. 2.1.2), they do contribute to the polarization of the ^{129}Xe nuclear spin in particular (for ^{3}He polarization such molecules are inconsequential [10, 41]). γ_M is a constant that depends on the rate of van der Waals molecule formation and contact interaction strength between Rb and the noble gas (i.e., Xe), while ζ is a constant that depends on the polarization and isotopic composition of Rb. During optical pumping, we can expect P_{Rb} to be high, and hence the smaller of the ζ values is applicable when calculating the spin exchange rates between ^{129}Xe and polarized Rb.

The second term of eq. 2.10 is simply the velocity-averaged cross section for binary Rb-(noble gas) spin exchange. A summary of the constants is provided in Table 2.3[9]. For comparison, Table 2.4 gives the calculated spin exchange rates for some of our experimental cells.

2.2.2 Relaxation mechanisms for noble gas nuclear spins

Interactions between noble gas nuclei and the cell walls are widely believed to be the dominant source of nuclear spin depolarization. However, these interactions are not fully understood. In 1965, Gamblin and Carber suggested the following: [5]:

Since the relaxation time seems to be independent of various nonmag-

[9]Note, the ^{3}He value for $\langle \sigma v \rangle_{SE}$ listed in Table 2.3 (taken from ref. [40]) is a factor of 2 smaller than an earlier value measured by Coulter *et al.* [42]. No explanation of the difference is given or suggested.

netic wall materials, one can perhaps only guess at the mechanism of relaxation as being adsorbed impurities on the wall surface.

More recently, Walker states in his 1997 review of spin exchange optical pumping [10]:

The detailed physical mechanisms of wall relaxation are poorly understood at present.

Actually, there is a fair amount of research on the subject of wall relaxation and although questions still remain, the basic principles for increasing the noble gas nuclear spin relaxation times are generally known.

^{3}He wall relaxation is believed to arise from two mechanisms: (i) relaxation due to diffusion of ^{3}He through the glass, and (ii) adsorption of ^{3}He on the glass surface [43–45]. In both cases the dominant depolarizing factor is the presence of paramagnetic impurities within the bulk glass and adsorbed on the glass surface. To minimize the wall relaxation rates, cells are made from glasses with low He permeability and low paramagnetic content[10], such as aluminosilicate glasses (e.g., Corning 1720 or Schott Supremax). In fact, assuming care is taken to clean the cell and ^{3}He gas, cells made from these materials have exhibited relaxation times that approach the bulk-limited ^{3}He-^{3}He dipole-dipole relaxation rate [46][11],

$$\frac{1}{T_{1_{dip-dip}}} = \frac{[^3He]}{744} hrs^{-1}. \tag{2.11}$$

One drawback of the aluminosilicate glasses is that they are notoriously difficult for glassblowers to work with, in contrast to borosilicates such as pyrex. Chupp

[10] Fe^{3+} is the major contributor to paramagnetic impurities in commercial glasses [45].

[11] Note that the long relaxation rates observed by Newbury *et al.* were in cells used for ^{3}He metastability pumping. Thus no Rb or N_2 were present, which is in contrast to spin exchange optical pumping. However, Rb is thought to be a benign surface coating for ^{3}He, and long relaxation times are similarly achievable.

and colleagues have shown that the borosilicate glass Corning 7056 (which has midrange paramagnetic impurity content and He permeability) yields cells with lifetimes similarly approaching the bulk dipole-dipole limited relaxation rates as given by eq. 2.11 [47].

For the much larger ^{129}Xe atom, permeability into the glass is not an issue. However, adsorption onto glass surfaces is quite significant because of the large ^{129}Xe polarizability. To address this issue, Zeng *et al.* showed that coating the cell walls with a siloxane-derivative dramatically increases the ^{129}Xe relaxation time [48]. For uncoated pyrex cells, they found the longitudinal relaxation time T_1 of polarized ^{129}Xe nuclei generally on the order of hundreds of seconds. In contrast, cells coated with SurfaSil[12] typically had much longer relaxation times, on the order of 20 minutes or more.

Driehuys *et al.* showed that in cells coated with SurfaSil, the dominant relaxation mechanism for ^{129}Xe is its dipolar coupling with protons in the coating [49]. Furthermore, they found that ^{129}Xe is trapped in the coating for surprisingly long times ($\tau > 10\ \mu s$). A motivating factor of the work presented in Chapter 6 is to determine whether the same coupling is the dominant relaxation mechanism for the coating we typically use, namely OTS[13].

Another relaxation mechanism for polarized noble gases is due to diffusion through inhomogeneous magnetic fields [5, 50] and is expressed as follows:

$$\frac{1}{T_1} = D_{ng}\frac{|\nabla B_\perp|^2}{B_z^2}\left(\frac{1}{1+\Omega_0^2\tau_c^2}\right), \tag{2.12}$$

[12]Pierce Scientific, Rockford, IL 61105. SurfaSil is primarily composed of dichlorooctamethyltetrasiloxane.

[13]*n*-octadecyltrichlorosilane.

where D_{ng} is the noble gas diffusion coefficient, $\nabla B_{\perp}$ is the transverse magnetic field, B_z is the main field strength, Ω_0 is the Larmor frequency of the noble gas, and τ_c is the mean collision time between atoms. In a careful examination of eq. 2.12, Cates *et al.* [51] showed that this expression is valid for cells at high pressure and high magnetic fields when the following is true:

$$\frac{\Omega_0 R^2}{D_{ng}} \gg 1. \tag{2.13}$$

R is a characteristic length scale of the cell (e.g., radius of a spherical cell).

In our multi-atmosphere gas cells, the inequality expressed in eq. 2.13 is easily fulfilled. Thus, to calculate the relative importance of inhomogeneous field relaxation, we begin by noting that the factor $(1+\Omega_0^2\tau_c^2)^{-1}$ of eq. 2.12 is nearly unity, since τ_c is on the order of 10^{-9} or 10^{-10} sec for gases at STP and field strengths are not commonly available for Larmor frequencies to be in the 10^9 sec^{-1} range. For ^{129}Xe at STP ($D_{Xe} = 0.057$ cm^2/s), and if we assume a 100 Hz linewidth in a 1 cm diameter spherical cell at 20 G (a worst-case scenario, implying $\nabla B_{\perp} \sim 0.1$ G/cm), we find that $1/T_{1\ inhomog} \sim 1.0 \times 10^{-6}$ Hz. Similarly, for ^{3}He at STP ($D_{He} = 1.96$ cm^2/s), the rate is $\sim 4.6 \times 10^{-6}$ Hz. In both cases, the contribution is small compared to the effects of wall relaxation.

2.3 Optical Pumping: experimental setup

Spin exchange optical pumping of ^{3}He and ^{129}Xe is performed using setups schematically show in Fig. 2.3. The key components are:

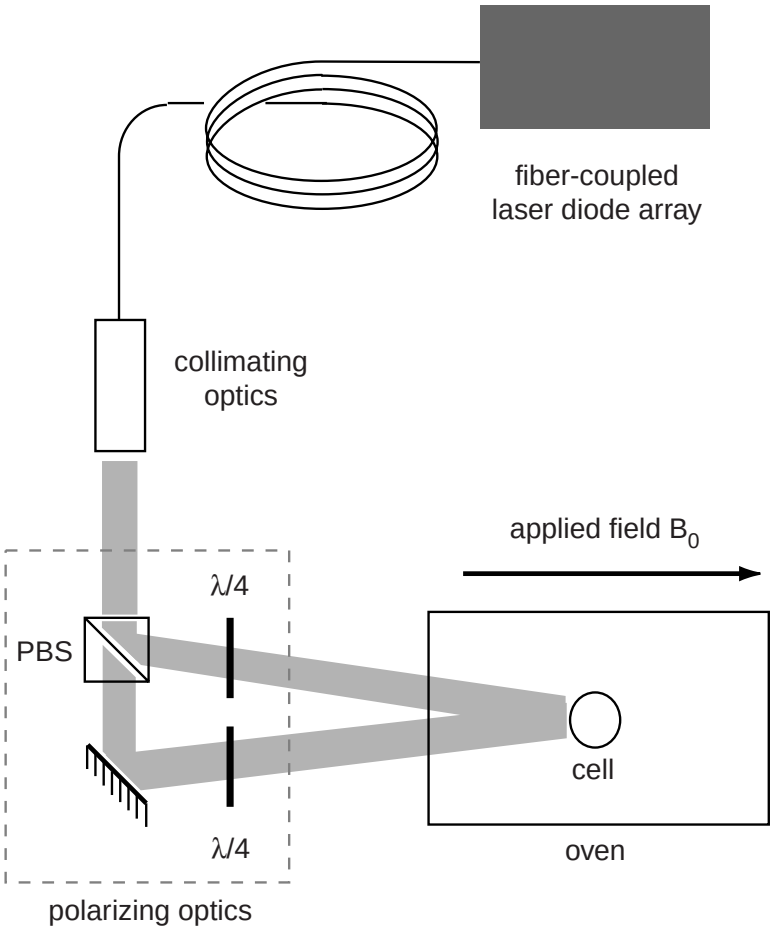

Figure 2.3: Schematic of the optical pumping apparatus.

- Rb D1 light source at 795 nm,
- collimating and polarizing optics,
- sample cell,
- oven, and
- main applied magnetic field B_0.

We typically use a 15 W Opto Power[14] fiber-coupled laser diode array (LDA) as our light source. A small set of collimating optics narrows the relatively divergent light from the LDA. A polarizing beam splitter cube[15] separates the light into two linearly polarized light beams (with orthogonal polarizations), which then pass through quarter-wave plates[16] to become circularly polarized light. A glass cell with a few mg of Rb, N_2, and noble gas(es) is placed inside an oven which is heated either by blown hot air or resistive heater tape[17]. The oven temperature is regulated by an Omega temperature controller[18] with a 100 Ω platinum RTD (resistance thermal device) placed within the oven as close as possible to the cell. Finally, the oven is situated in a magnetic field B_0 which provides the orientation axis for the atoms. In situations where we were working near a high-field (> 1 tesla) magnet (e.g., at MIT or the Brigham and Women's Hospital), we would use the fringe field of the magnet as B_0 (typically between 100-500 Gauss). In our lab at the CfA, we created B_0 with a low field solenoid at ~ 8 G.

The cell is placed in an oven to increase the Rb vapor density. Killian first

[14]model OPC-A015-FCPS, Spectra-Physics Semiconductor Lasers (formerly known as Opto Power Corp.), Tucson, AZ.

[15]CVI Laser Corp., Putnam, Connecticut.

[16]ibid.

[17]Heater tape is easier to use, since it does not require a source of compressed air. However, it does not generally heat the volume as uniformly as blown hot air. Of course, this also depends on the design of the oven.

[18]Series CN8500, Omega Engineering, Inc., P.O. Box 2284, Stamford, Connecticut.

measured the Rb vapor pressure $p(T)$ to yield the frequently cited result [52][19]:

$$\log_{10} p(T) = 9.55 - 4132/T \tag{2.14}$$

A more recent measurement, valid between the Rb melting point (39.31 °C) and 277 °C, is as follows [54, 55]:

$$\log_{10} p(T) = 9.318 - 4040/T. \tag{2.15}$$

In both cases, p is in pascals (N/m^2) and T is in kelvins. To calculate the rubidium density [Rb], one can simply use the ideal gas law $p = nRT$. In particular,

$$[Rb] = \frac{p}{(1.38 \times 10^{-17})T}, \tag{2.16}$$

where [Rb] is measured in cm^{-3}. The choice of which equation to use (2.14 or 2.15) is relatively unimportant in our experiments, since we do not know precisely the temperature of the Rb vapor owing to temperature gradients of a few degrees that exist within the ovens, between the RTD temperature sensor and the glass cell, and across the cell. For example, recent work using Raman scattering to determine the temperature inside a sample cell during optical pumping with a high-power laser diode array [56] indicates that the temperature may in fact be up to 10 °C higher within the cell than expected by measuring the oven temperature alone. The higher temperatures are probably due to the excess heating by the off-resonant laser light.

We usually heat cells to $\sim$ 100 °C for pumping ^{129}Xe cells, while ^{3}He cells are

[19] Killian's original paper gives the formula $\log_{10} p(T) = 10.55 - 4132/T$. However, Killian measures $p(T)$ in *(chemical) bars*, which was originally suggested in 1903 to denote a pressure of 1 dyne/cm^2, or 0.1 pascals. The common (meteorological) bar, introduced in 1910, is equivalent to 10^6 (chemical) bars [53].

heated to slightly higher temperatures, $\sim 150\,^{\circ}$C. Because of the slow Rb-^{3}He spin exchange rate, fast diffusion of ^{3}He, and long T_1 times of ^{3}He in well-prepared cells, optical pumping in an optically dense Rb vapor is desirable when polarizing ^{3}He and hence requires the elevated oven temperature. On the other hand, the faster Rb-^{129}Xe spin destruction and exchange rates, slower diffusion rate of ^{129}Xe, and the need to protect the wall coatings from high-temperature alkali attack call for greater optical transparency and thus lower oven temperatures when polarizing ^{129}Xe.

Polarizations between 1%–10% were easily and repeatedly achieved with our cells; variations from cell to cell were attributed to differences in coating quality and the purity of the gases used to fill the cell. Optically pumping a ^{129}Xe cell typically requires 20 minutes, while a ^{3}He cell needs several hours. Before conducting an experiment using the polarized noble gas, the cell would be cooled to room temperature – often by placing the cell into a bath of cool water.

In the sections that follow, I describe in detail the characteristics of the lasers we used and the procedure for coating and filling an optical pumping cell.

2.3.1 High-power laser diode arrays

The development of $Ga_{1-x}Al_xAs$ diode laser arrays has been a contributing factor to the growing interest in polarized noble gas research [57], primarily because they provide high-power near-infrared laser light that is both economical and easy to use. As previously mentioned, our primary sources of light at 795 nm are high-power fiber-coupled LDAs from Opto Power Corp. These units are composed of 24 diode arrays which are coupled to individual fiber optic cables via cylindrical microlenses. The 24 fibers (typically 1–5 meters in length) are bundled together and can deliver up to 15 Watts of power in a beam with a 12° divergence angle.

The applied current and mean temperature of the arrays are set via an external controller box. Each unit can be powered by a common 120 V AC outlet.

Distinct advantages of these devices include *(i)* high output power (15 W), *(ii)* low cost ($\sim$ \$10,000), *(iii)* portability, and *(iv)* ease of use. On the other hand, drawbacks of these lasers include *(i)* very broad linewidths ($\sim$ 2 nm or 1 THz) and *(ii)* poor systems engineering of the units, resulting in variable operating reliability. For example, we found that some of the units overheated when operating at full power if the room temperature was greater than $\sim$ 27 ℃ or if the unit was not in a well-ventilated space. Also, operating these LDAs in regions of magnetic fields $>$ 50 G (e.g., near NMR magnets) caused the cooling fans to malfunction, which led to overheating of the LDA system.

For comparison, the Spectra-Physics Titanium:Sapphire (Ti:Sapph) laser[20] we also have in the lab can produce $\sim$ 3 W of very narrow (FWHM[21] $<$ 40 GHz) light. However, it is expensive ($\sim$ \$100,000), bulky, and requires specialized installation (e.g., a chilled water supply). In terms of efficiency, the Opto Power lasers cost $\sim$ \$7,000 per Watt of resonant light (assuming only 10% of the light can be absorbed by pressure broadened Rb) while the Ti:Sapph is much more expensive, about \$33,000 per Watt of resonant light.

The tuning and output power of the Opto Power LDAs varies from unit to unit, and is dependent on both the applied current and temperature. In order to study these dependencies, we used the setup shown in Fig. 2.4 [58]. The laser spectrum was scanned using a Fabry-Pérot cavity[22] with a free spectral range (FSR) of 4 nm. With a telescope arrangement, we could image each fiber of the 24 fiber bundle onto a given plane and use a pin hole to admit light from only one of the fibers through

[20]Model 3900S, Spectra Physics, 1335 Terra Bella Ave., PO Box 7013, Mountain View, CA.
[21]Full Width Half Max.
[22]model RC-110, Burleigh Instruments, Inc., Burleigh Park, Fishers, New York.

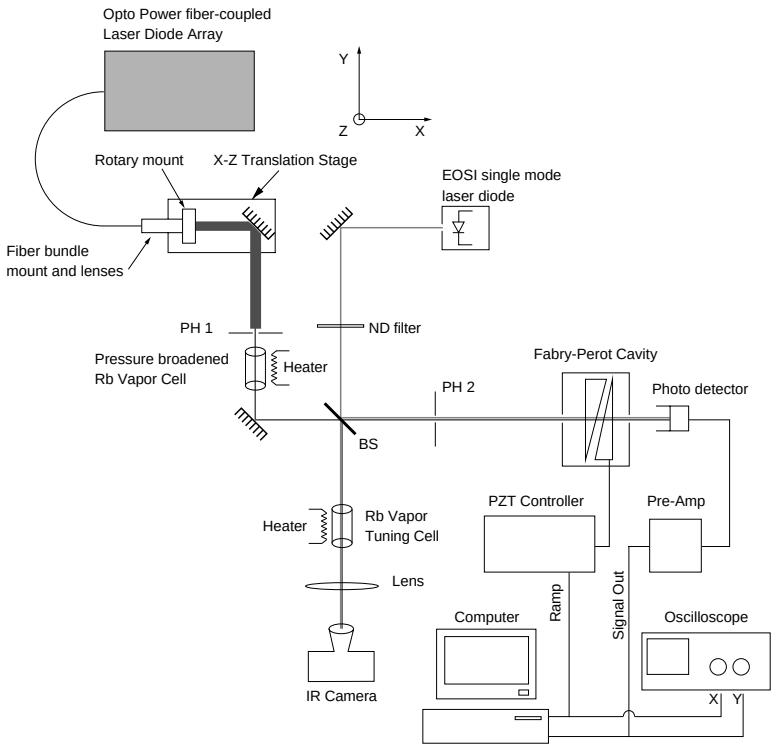

Figure 2.4: Schematic of the LDA characterization setup.

to the Fabry-Pérot cavity. A photodetector was placed by the output end of the cavity and an Apple Macintosh computer was used to record the spectrum. For spectral calibration we used a second, less intense single-mode diode laser[23] with a FWHM < 4 MHz, which is considerably less than the 20 GHz resolution of the cavity. To check the tuning of the single-mode laser, part of its light was directed through a Rb vapor cell, which fluoresced when the laser was on resonance with the Rb D1 line and could be detected by an infrared camera. To ensure we were measuring the LDA spectrum in the correct FSR, we had another Rb vapor cell (pressure broadened by ~ 1 atm of N_2) that could be placed in the optical path of the LDA light; we observed a noticeable "dip" in the spectrum when we were in the

[23]model LCU2010M, Newport TMS (formerly EOSI), 1501 South Sunset Street, Suite D, Longmot, Colorado.

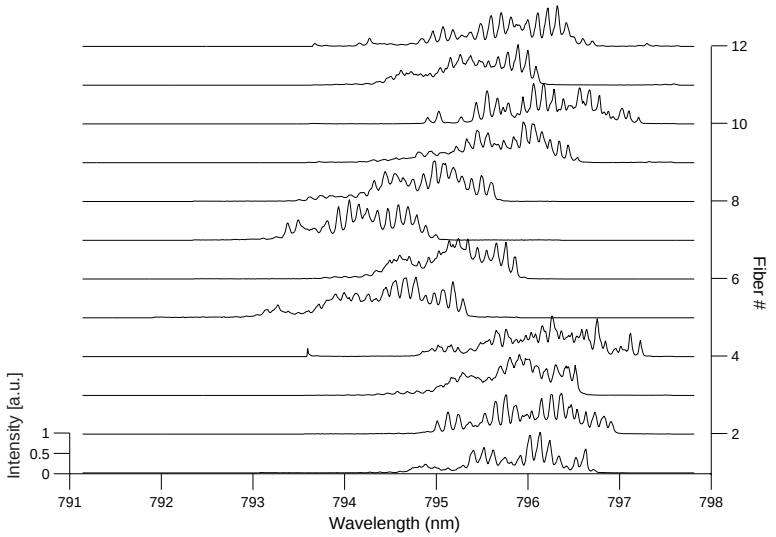

Figure 2.5: Spectra from 12 of the 24 fibers from Opto Power LDA P-205. Operating current=31.9 A and T=24.1 ℃.

correct FSR.

Fig. 2.5 gives an example of the various spectra emitted by individual fibers in the optic fiber bundle of an Opto Power LDA. Obviously, the individual diode arrays are manufactured to emit close to 795 nm, but process variations and differing operating conditions for each of the arrays results in the multi-mode, non-uniform spectra observed. When the spectra are summed together, as in Fig. 2.6, the result is a broad emission spectrum with a FWHM[24] of approximately 2 nm, as per manufacturer's specifications.

For the work presented in this dissertation, a number of different (but similar model) Opto Power LDA units were used for optical pumping. The characterization studies were important to determine the correct operating current and temperature that would maximize the available laser light about 795 nm. While each of the

[24]For the overall spectrum of an LDA, we defined the FWHM as the spectral width about the "peak wavelength" which yields an integrated intensity equal to 68% of the total integrated intensity. "Peak" (or "center") wavelength for a given spectra was defined to be the wavelength at which half of the integrated power was at lesser (greater) wavelengths.

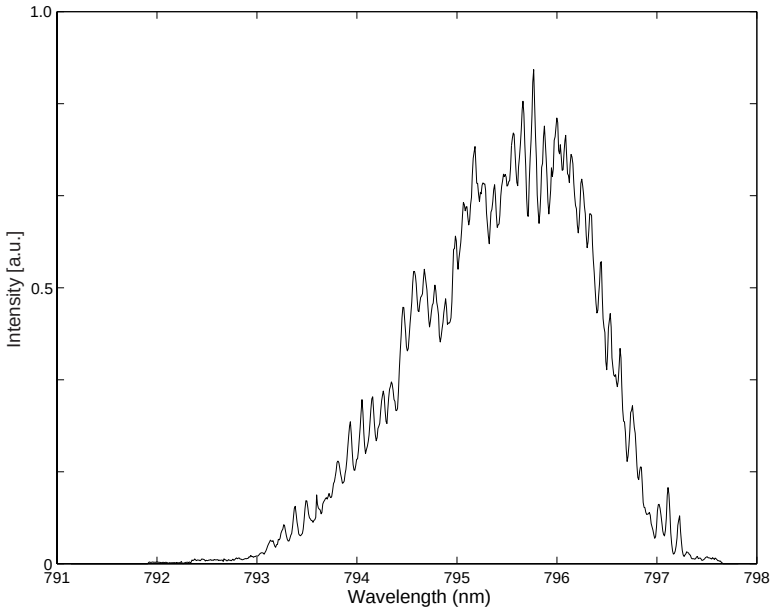

Figure 2.6: Sum of 12 individual fiber spectra from Opto Power LDA P-205 (shown in Fig. 2.5). The linewidth of this summed spectrum is $\sim$ 2 nm.

11 units we examined had different optimal settings, we determined that variations in total output power or optimal settings were uncorrelated with the age of the LDAs or with any other information provided by the manufacturer. Table 2.5 lists a summary of the average parameters measured; ref. [58] provides further details.

2.3.2 Polarization Cells

Important steps in polarizing ^{3}He and ^{129}Xe include the careful design, fabrication, and preparation of appropriate glass cells. ^{129}Xe-only cells are typically made from pyrex, which is an easy glass for glassblowers to work with (thus allowing a great deal of flexibility in cell design) and can be coated to prolong ^{129}Xe T_1 times. For cells containing ^{3}He we generally use a less He-permeable glass such as the borosilicate glass Corning 7056 or aluminosilicates such as Corning 1720 or 1724. For experiments that required delivery of the polarized gas to a sample (e.g., the lung

Property	average value	
Age (as of Feb, 1999)	21	months
Operating hours	2049	hours
Total Power	12.6	Watts
$\partial\lambda/\partial T$	0.31	nm/ ˚C
$\partial P/\partial T$	-0.25	W/ ˚C
$\partial\lambda/\partial I$	0.28	nm/A
$\partial P/\partial I$	0.46	W/A
Linewidth	1.9	nm

Table 2.5: Average operating parameters of Opto Power LDAs (see ref. [58]). Values quoted represent the average of 11 units examined.

imaging performed in Chapter 4), cells were fitted with valves. Figure 2.7 illustrates some of the polarization cells we used.

The ^{3}He-only cells used in our experiments were designed and made by our collaborators at the University of New Hampshire. They commonly work with aluminosilicate glasses and have a rigorous cleaning and ^{3}He filling regimen that has consistently produced high quality ^{3}He-polarization cells. A detailed description of their cell preparation regimen can be found in ref. [59]. In our lab, we specialized in producing ^{129}Xe, or mixed ^{129}Xe-^{3}He cells, which are slightly different from the ^{3}He-only cells in that they must also be coated with a silane- or siloxane-derivative. Below, we discuss the "recipe" used for cleaning and coating cells, and conclude with a discussion of the methods used to fill cells with the desired gas quantities.

Cleaning and Coating Procedure

The cleaning and coating procedures we used are outlined in Tables 2.6 and 2.7, and are adapted from Oteiza [60] with modifications suggested by Rosen [61]. As previously mentioned (i.e., in section 2.2.2), proper preparation of the cell surfaces can extend the polarization lifetimes of polarized ^{3}He and ^{129}Xe. For historic reasons,

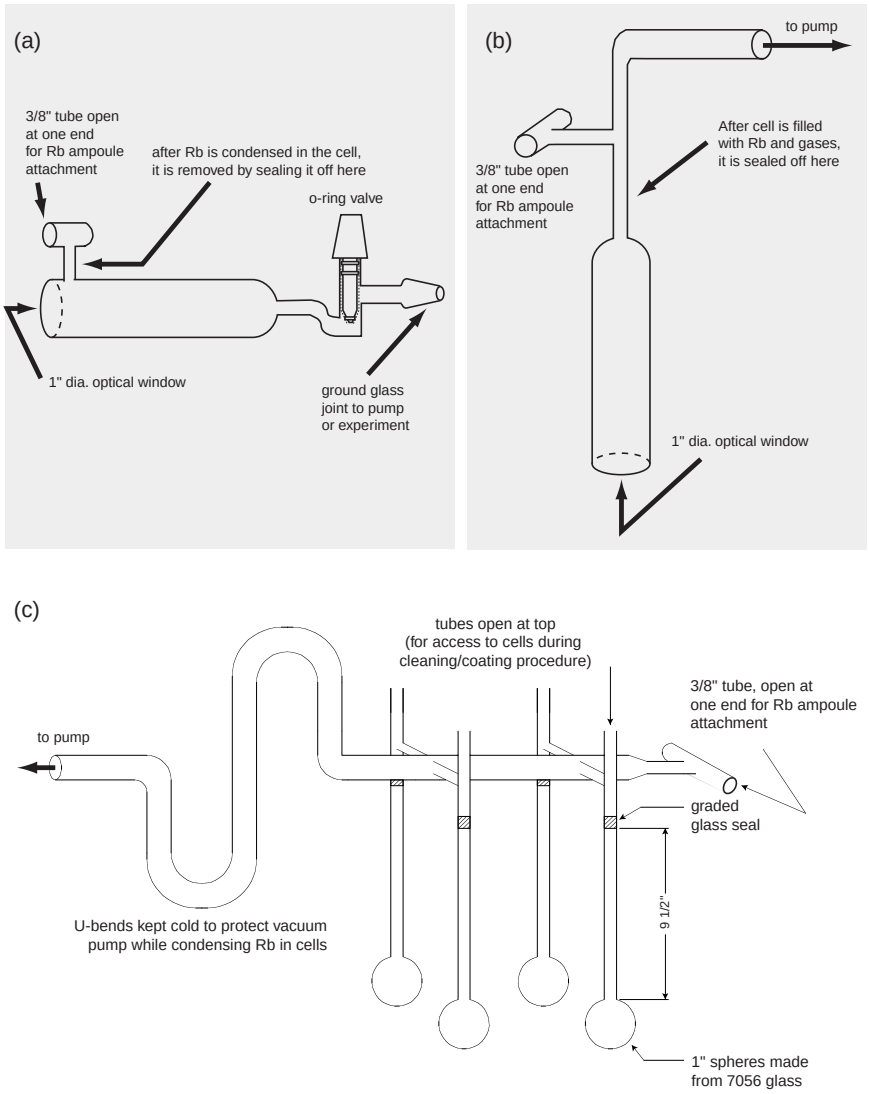

Figure 2.7: Glass cell designs. Three example cell designs are shown here: (a) a valved cell that allows the gas to be delivered to an experiment after it has been polarized; (b) a sealed cell for persistence experiments (We also used this design for a "thermal Xe" cell, which did not contain any Rb. Instead, we filled it with a Xe/O_2 mix that had a rapid T_1 ($\sim$ seconds) and at high field could be used to calibrate the polarization achieved through optical pumping); and (c) a manifold for making four 1" spherical sealed cells (The design must allow access for cleaning and coating, an attachment point for a Rb ampoule, and a port to attach to a pump station). Except for (c), all the cells were made from pyrex; for the 4-cell manifold, the body was made from pyrex, but the spheres were made of Corning 7056 glass. Our glasswork was handmade by Mr. Charles Raworth of Wilbur Scientific, Inc., 37 Leon Street, Boston, MA.

we coat our cells with OTS as opposed to SurfaSil, the latter being a common coating used by Happer and many of his students and colleagues. In comparing our typical ^{129}Xe longitudinal relaxation times (T_1) with published results in SurfaSil-coated cells, there appears to be little difference in using either coating. For example, we made an OTS-coated cell (P-2) that had a ^{129}Xe T_1 time greater than 3 hours ($>$ 10,800 sec) when left in a 4.7 T magnetic field; Breeze *et al.* report a ^{129}Xe T_1 of 10,300 sec for one of their SurfaSil-coated ^{129}Xe cells (SSD-1) measured at the same field strength [62]. However, these T_1 times are somewhat "best case" values, and the variance in different cells is usually attributed to paramagnetic impurities that may exist in the glass, or have contaminated the cell at some stage of its production. Furthermore, as we shall see in Chapter 6, at low magnetic fields ($<$ 100 G) the ^{129}Xe T_1 times vary as a function of the magnetic field.

step 1	Wash the cell with Alconox[25] mixed with distilled (DI) H_2O.
step 2	Rinse with DI H_2O.
step 3	Clean with *piranha* solution (3:7 ratio by volume of 20% H_2O_2 and concentrated H_2SO_4). Allow to sit for about an hour.
step 4	Rinse (3×) with DI H_2O.
step 5	Rinse (3×) with methanol.
step 6	Dry the cell (under rough vacuum, flowing N_2, or by heating the cell to drive off moisture from the surface).

Table 2.6: Cell cleaning protocol.

Figure 2.8 illustrates our general understanding of how the coating process occurs. After hydrolysis of the OTS molecule, hydrogen bonding occurs between the surface and the OTS molecule, and then again between neighboring OTS molecules. Ideally, these hydrogen bonds are all converted to covalent bonds with H_2O as a

[25] A detergent used to clean glassware, manufactured by Alconox Inc., New York, New York 10003.

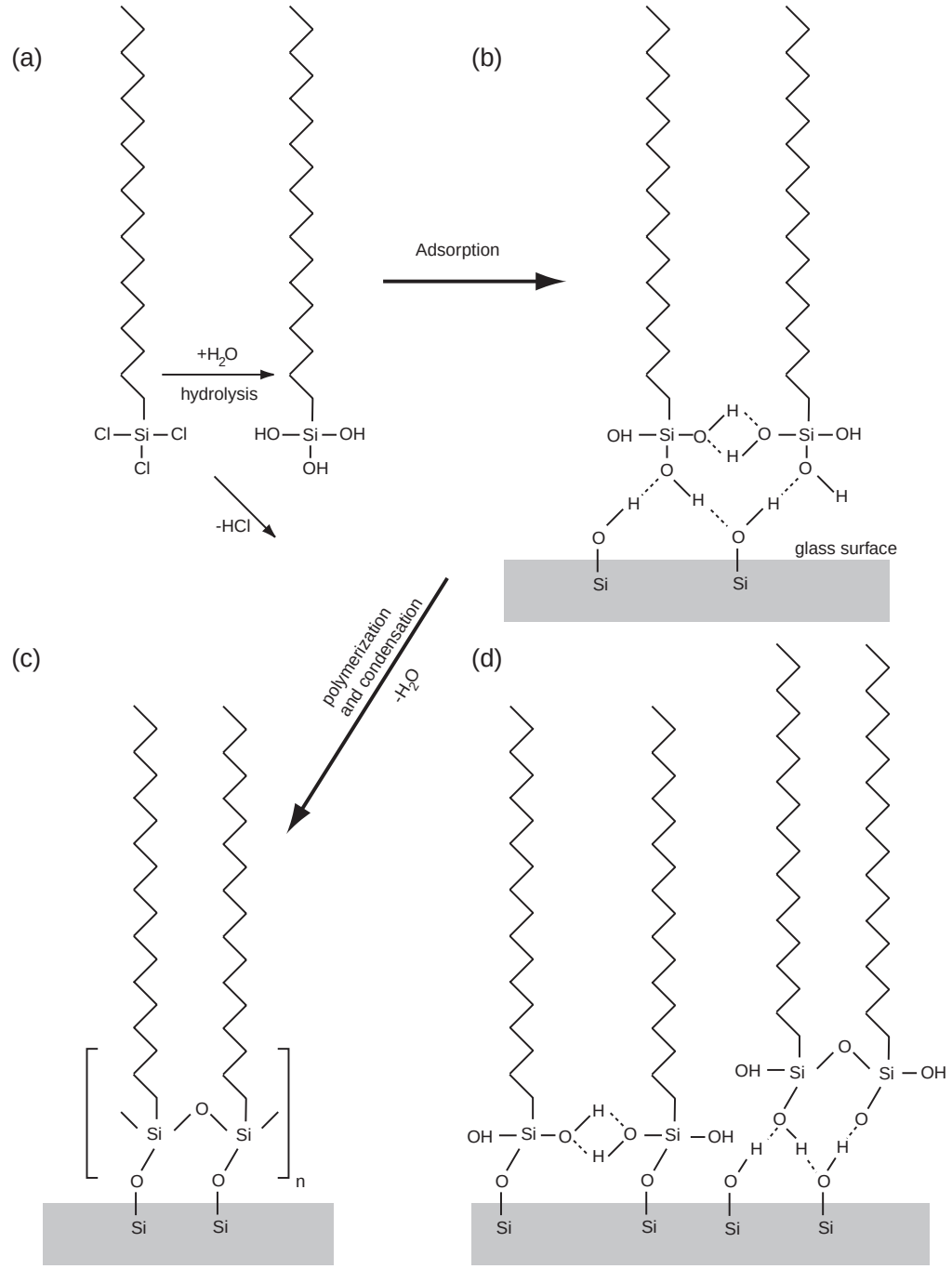

Figure 2.8: Chemisorption of *n*-Octadecyltrichlorosilane (OTS) on glass [63,64]. (a) hydrolysis occurs (with trace amounts of H_2O on glass surface), releasing HCl; (b) adsorption occurs by hydrogen-bonding between OH groups; (c) ideally, polymerization and condensation occurs, with H_2O given off; (d) in reality, some hydrogen-bonding probably still exists, either between OTS molecules, or between OTS and the surface. This figure is an adaptation from Sagiv [64].

step 1	Rinse the cell with hexanes.
step 2	Rinse a clean beaker with hexanes (3×), and then pour into the beaker enough hexanes to fill the cell.
step 3	Prepare coating solution by mixing a little OTS into the beaker full of hexanes. Typically a few drops of OTS mixed with hexanes is more than enough to coat a 1" spherical cell. Mix solution and pour into the cell.
step 4	Allow the solution to sit inside the cell for 5-10 minutes.
step 5	Pour out coating solution and rinse the cell 3× with hexanes.
step 6	Rinse the cell (3×) with chloroform.
step 7	Rinse the cell (3×) with ethanol.
step 8	Allow cell to sit out overnight (exposed to the atmosphere).

Table 2.7: Cell coating protocol.

by-product, but in reality the coating is probably a mixture of both covalent and hydrogen bonds [64].

The coating, if done properly, forms a hydrophobic surface which prevents or minimizes interaction with the glass surface itself. After the coating procedure described in Table 2.7, we test the coating by placing some distilled water into the cell; a good coating should not allow the water to wet the glass. On occasions where the coating is poor, we have been able to successfully apply more OTS coating without having to strip away the existing OTS. Re-cleaning the cell with the *piranha* solution does not remove the OTS coating, nor does baking the cell[26] up to temperatures of 400 ˚C [65]. Also, Sagiv as shown that with patches of OTS already bonded to the surface, it is possible for additional OTS to fill the gaps during a subsequent coating procedure [64, 66].

It is important to avoid coating areas that will be flamed sealed, since the reaction

[26]This is true only if no alkali metal is present in the cell. If Rb is also in the cell, the coating will be attacked by the Rb at temperatures exceeding $\sim$ 200 ˚C.

of OTS with hot glass is believed to result in depolarizing surfaces. If the coating has inadvertently found its way to such regions, it is possible to remove the coating with a strong basic solution such as concentrated sodium hydroxide (NaOH). Just as Rb will attack the coating at elevated temperatures, we have observed that NaOH can effectively remove OTS bonded to the surface. A cautionary note: NaOH will also etch the glass, and presumably increase the surface roughness. Hence, it is advisable to expose the glass surface to NaOH for as short a time as possible.

Cell filling procedure

Once a cell has been cleaned and coated, we attach a sealed Rb ampoule to it with a small piece of glass rod inside that acts as a plunger (to break the Rb glass seal later). The cell is then placed on a high vacuum pump station via an Ultra-torr connector[27]. The cell is evacuated by a turbomolecular vacuum pump[28] and baked out for 2 days at $\sim$ 150–200 $^{\circ}$C. At this point, the pump pressure is usually in the 10^{-8} Torr range, while an ion-gauge closer to the cell reads in the 10^{-6} Torr range.

Rb metal must be condensed in the cell under vacuum before gases are admitted. By shaking or rotating the cell quickly, we allow the glass plunger to break the small glass seal which protects the Rb stored in one end of the ampoule. Argon is usually sealed in with the Rb, and must be pumped away after the seal is broken (if needed, we melt the Rb with a cold flame[29] to allow the argon to escape out of the broken seal). The Rb is heated and then "chased" (or condensed) into the cell with a cold flame, until there are a few macroscopic Rb drops in the cell. We often wrap the coated portions of the cell in wet paper, and then cover it with aluminum foil to

[27]This connector allows glass to be mated to the otherwise metal station via a compressible rubber O-ring.

[28]Pump system PT 151, Leybold Vakuum GmbH, Cologne, Germany.

[29]For example, we used a methane-oxygen torch for our glasswork; with the oxygen turned off, the flame is "cold" and does not melt the glass.

protect it from unintentional heating. Finally, we usually seal the Rb ampoule/cell connection by heating and collapsing the glass;[30] as this occurs, we remove the Rb ampoule and dispose of it appropriately.

As mentioned earlier and shown in Fig. 2.7, there are two types of cells we commonly make: "valved" cells and "sealed" cells. Valved cells include a valve which allows one to repeatedly fill and empty the cell with gases; in contrast, a sealed (glass) cell is permanently sealed (with a torch) after being filled with gases. Practically speaking, valved cells are easier to calibrate and fill, but generally do not have the longevity of a sealed cell because of accumulated contamination of oxygen and water from repeated fillings with not-perfectly-clean gas, and because of human error (e.g., accidentally opening the valve). Again, the choice between using a valved or sealed cell depends on the experimental requirements.

The basic idea in filling a cell involves loading a pre-determined amount of gas into a "reservoir" volume on the pump station (we refer to it as the pump station *manifold*). During this step, the cell is isolated from the reservoir, usually by a valve either on the cell itself or on the pump station manifold. When the desired load pressure is reached, the valve is opened and the gas is allowed to fill the cell.

Xenon gas is particularly easy to work with because it has a melting temperature of ~ 161 K and a boiling temperature of ~ 166 K. Using liquid nitrogen, one can cool a sample cell to ~ 77 K, and thus easily condense xenon into the cell. Practically, this means that all the gas initially loaded into the reservoir volume (at pressure $P_{Xe\ load}$) will end up in the cell. If P_{Xe} is the pressure of xenon we desire in the cell at room temperature, then using the ideal gas law ($PV = NRT$) it is easy to show

[30] This is accomplished with a "hot" methane-oxygen flame, i.e., temperature in excess of 820 °C, which is the softening point for pyrex.

that

$$P_{Xe\ load} = P_{Xe}\left(\frac{V_{cell}}{V_{manifold}}\right), \tag{2.17}$$

where V_{cell} and $V_{manifold}$ are cell and manifold volumes as defined in Figures 2.9 and 2.10. Table 2.8 describes the manner in which we determine $\left(\frac{V_{cell}}{V_{manifold}}\right)$.

Step	Sealed cell	Valved cell
	pump station manifold and cell should be at vacuum.	
1	close the valve between the manifold and the cell, and fill only $V_{manifold}$ with an arbitrary amount of test gas (e.g., N_2). Record the pressure as $\mathbf{P_1}$.	close the cell valve and fill only $V_{manifold}$ with an arbitrary amount of test gas (e.g., N_2). Record the pressure as $\mathbf{P_1}$.
2	open the manifold valve to allow the test gas to expand into the cell (V_{cell}) and interstitial tubing (V_{tube}). Record the reduced pressure as $\mathbf{P_2}$.	open the cell valve to allow the test gas to expand into the cell (V_{cell}). Record the reduced pressure as $\mathbf{P_2}$.
3	now place the cell volume into a bath of liquid nitrogen, so that the cell volume V_{cell} is at 77K, while the remaining volumes ($V_{manifold} + V_{tube}$) are at room temperature (∼297K). Record the overall pressure as $\mathbf{P_4}$.	
$\frac{V_{cell}}{V_{manifold}}$	$\left[\frac{P_1}{P_2 P_4}\left(P_2 - P_4\right)\right]\left(\frac{1}{\alpha - 1}\right)$	$\left(\frac{P_1}{P_2} - 1\right)$

Table 2.8: Cell volume calibration protocol for sealed and valved cells. $\alpha = T_{room}/T_{liquid\ N_2}$. See fig. 2.9 and 2.10 for the volumes represented by V_{cell}, V_{tube}, and $V_{manifold}$.

Other gases, such as N_2, ^{3}He, ^{4}He, or O_2 (used for thermally polarized noble gas cells), are added afterwards assuming the sample cell is kept cold enough for the xenon to stay frozen. Care must be taken to account for residual vapor pressures of non-condensing gases which fill both the cell and the reservoir volume and to

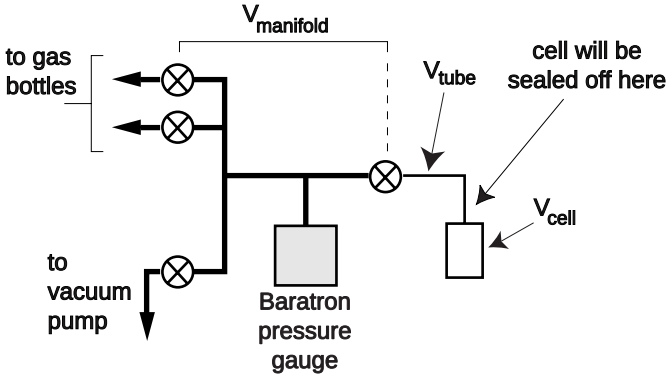

Figure 2.9: Schematic of *sealed* cell and pump station manifold with relevant volumes labeled.

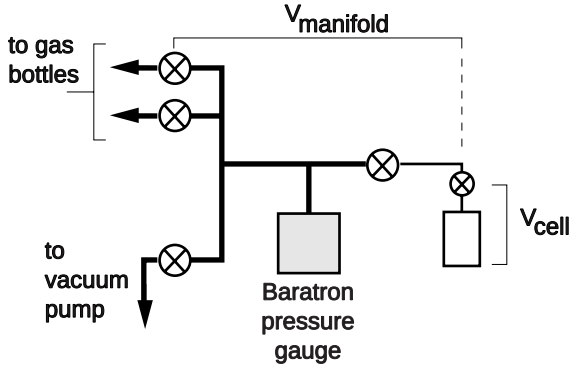

Figure 2.10: Schematic of a *valved* cell and pump station manifold with relevant volumes labeled.

allow sufficient time for full diffusive mixing of such gases. Obviously, once the cell is either sealed or valved off, gas left in the reservoir does not contribute to the amount found in the cell.

Once the desired quantities of gas have been loaded into the cell, the last step is to remove the cell from the pump station. For sealed cells, we need to flame seal the connecting tube, which is only possible if the pressure inside the tubing is below atmospheric (otherwise it will blow outward when the glass is heated to its melting temperature). If the pressure inside the cell at room temperature is > 1 bar, then the cell is cooled in LN_2 to condense gases such as xenon and lower the pressure of non-condensing gases by a factor of close to 4 (the ratio of room temperature to LN_2 temperature). Valved cells naturally do not require flame sealing, and can be removed easily once all the appropriate valves are closed.

Chapter 3

Basic NMR techniques as applied to laser-polarized noble gases

3.1 Preliminaries

As is well known, there is a close correspondence between the quantum mechanical magnetic moment expectation values ($\langle\mu_x\rangle$, $\langle\mu_y\rangle$ and $\langle\mu_z\rangle$) and the classical magnetization components (M_x, M_y, and M_z) for an ensemble of nuclear spin 1/2 atoms or molecules. For example, both theories show that the dynamics are governed by the Bloch equations (e.g., see ref. [67]):

$$\frac{dM_x}{dt} = \gamma(\mathbf{M}\times\mathbf{B})_x - \frac{M_x}{T_2} \tag{3.1}$$

$$\frac{dM_y}{dt} = \gamma(\mathbf{M}\times\mathbf{B})_y - \frac{M_y}{T_2} \tag{3.2}$$

$$\frac{dM_z}{dt} = \frac{M_0 - m_z}{T_1} + \gamma(\mathbf{M}\times\mathbf{B})_z \tag{3.3}$$

where we have chosen the quantization axis (i.e., main applied field B_0) to lie in the $\hat{z}$ direction; T_1 and T_2 denote the phenomenological longitudinal and transverse

relaxation times. Interestingly, equations (3.1-3.3) are also valid for time-dependent **B**. In particular, the application of an oscillating magnetic field B_1 (which we assume to be orthogonal to B_0) leads to population changes and coherences between different magnetic states of an atom (quantum mechanically speaking) and can be thought of as a precession of the magnetization vector (classically speaking).

For example, the transition probability $\mathcal{P}(t)$ between state populations is given by the familiar expression for Rabi oscillation [68]:

$$\mathcal{P}(t) = \frac{\omega_1^2}{\omega_1^2 + (\Delta\omega)^2} \sin^2 \left[\sqrt{\omega_1^2 + (\Delta\omega)^2} \frac{t}{2} \right]. \tag{3.4}$$

ω_1 is the Rabi frequency due to B_1 (i.e., $\omega_1 = \gamma B_1$) and $\Delta\omega$ is the difference between the oscillation frequency (ω) of B_1 and the Larmor frequency (ω_0) of the nuclear spin. When the oscillating field is on-resonance with the Larmor frequency (i.e., $\Delta\omega = 0$), $\mathcal{P}(t)$ varies from 0 to 1 with Rabi frequency ω_1. Classically this is equivalent to saying that on-resonance, the B_1 field appears stationary in the rotating frame of the atom and that the magnetization vector **M** simply precesses about this field at a rate determined by the strength of B_1. In "pulsed" NMR, such a B_1 would be applied for only a brief duration τ, and in effect "tips" **M** an angle θ away from the $\hat{z}$ direction, where θ is equal to $\gamma B_1 \tau$. Consequently, $M_z = |\mathbf{M}| \cos(\theta)$, while in the transverse plane there is a component $|\mathbf{M}| \sin(\theta)$.

It is this latter transverse component that gives rise to a detectable signal through Faraday induction in a nearby pickup coil; quantum mechanically speaking, the off-diagonal elements of the density matrix (i.e., the coherences) are detected. The oscillating signal, known as a "free induction decay" or FID, decays in time as the individual spins dephase from one another due to spin-spin coupling, local magnetic field inhomogeneities, and other possible environmental effects (e.g., applied

magnetic field gradients). *Inhomogeneous broadening* occurs when the decay is dominated by field inhomogeneities or other local environmental differences as seen by the atoms, and is commonly labeled with the time constant $T_2{}^*$. For transverse relaxation that occurs uniformly throughout the ensemble (*homogeneous broadening*), one typically refers to T_2. As we shall discuss next, it is possible with "spin echoes" to refocus $T_2{}^*$ dephasing; hence $T_2{}^* \leq T_2$.

Spin echoes were discovered in 1950 by Hahn [69] and are among the key building blocks of modern pulsed NMR[1]. Hahn found that applying a second RF pulse after the FID from an initial pulse had decayed away gave rise to yet another signal, the so-called "spin echo." A simple spin echo pulse sequence is shown in Fig. 3.1; a graphical explanation is given in Fig. 3.2. Spin echoes are important because they

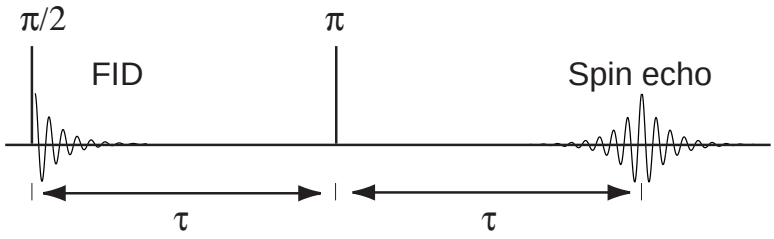

Figure 3.1: $\pi/2$ – π RF pulses result in a spin echo.

allow one to compensate for $T_2{}^*$ effects. Furthermore, one acquires a spin echo signal as the spins are refocussing, and then as they dephase once more. This is twice the amount of information obtained through a simple FID and by assigning $t = 0$ to be equal to the point of maximum detected signal (from either an FID or spin echo),

[1]It should be noted that modern NMR and MRI research is predominantly "pulsed," and employs an ever-growing variety of sophisticated "pulse sequences" that allow one to perform complex manipulations of the nuclear spins [i.e., the B_1 field is applied for a short period (with possible repetitions), and the transient magnetization dynamics are detected]. In contrast, early NMR experiments were performed in "continuous-wave" (CW) mode, (i.e., a steady-state B_1 field is applied and the magnetization is detected as the main magnetic field is swept through resonance). The availability of fast, affordable computers to perform fourier analysis and the development of novel techniques such as spin echoes [67, 69] were driving forces that led to this modern trend.

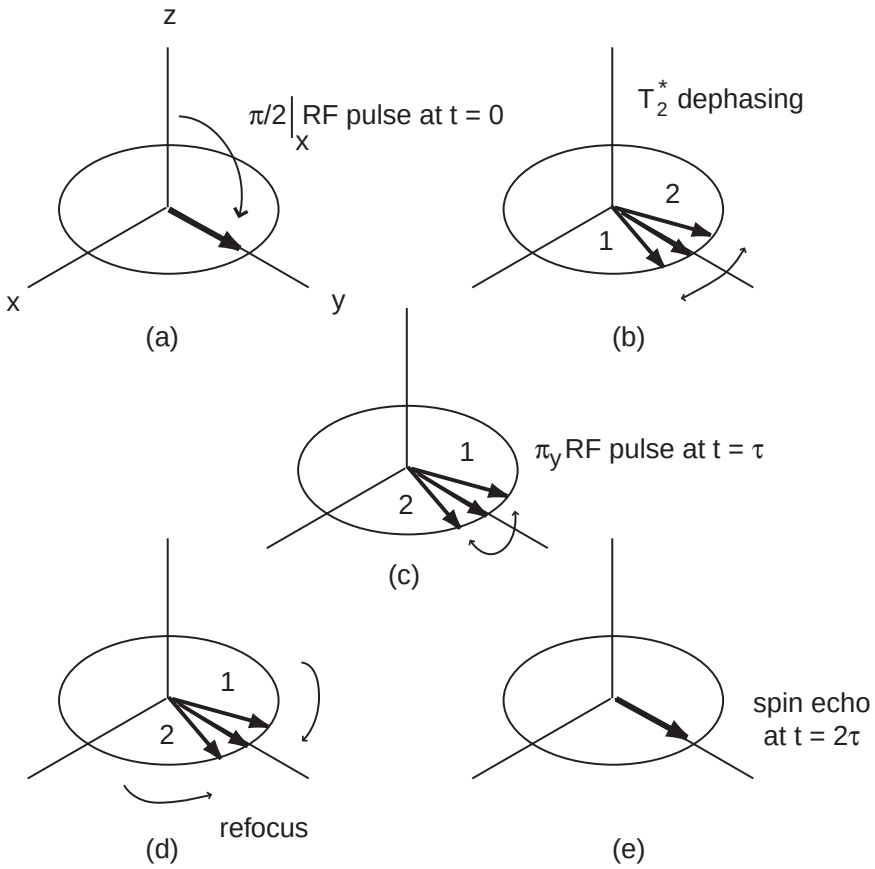

Figure 3.2: Graphical explanation of spin echoes [note: the rotating frame is assumed throughout]. (a) An initial $\pi/2$ RF pulse (aligned with the $\hat{x}$ axis in the rotating frame) places the magnetization $\mathbf{M}$ into the transverse xy plane aligned with the $\hat{y}$ axis. (b) Spins precess at different rates, resulting in a spread (dephasing) of the magnetization vector. For example, spin "2" precesses faster than the mean, while "1" is a bit slower. Consequently, "2" leads in phase while "1" lags behind. (c) A π RF pulse (aligned with the $\hat{y}$ axis in the rotating frame) reverses the relative phases of the spins; for example, spins "1" and "2" have had their relative positions reversed. (d) Nonetheless, spin "2" is still precessing faster than the mean, while "1" is still slower. Therefore, the phase difference between them decreases. (e) When their phase differences return to zero, all the magnetization is again aligned along $\hat{y}$, and a spin echo appears.

it is clear that spin echoes yield "negative time" data in addition to the "positive time" signal inherent to FIDs.

"Gradient echoes" are another means of obtaining both negative and positive time NMR signal. Rather than using a second (π) RF pulse to cause the spins to refocus, a gradient echo is created by first intentionally dephasing the spins with an applied magnetic field gradient ($G_1 > 0$) that dominates over any T_2^* effects, and then *reversing* the applied magnetic field gradient ($G_2 < 0$), resulting in an echo that is centered (in time) when $\int^{t_1} G_1 dt = \int^{t_2} |G_2| dt$. It is apparent that this method does not compensate for T_2^*; nonetheless, it is useful for some NMR applications. In particular, it is well suited for laser-polarized noble gas applications.

As we have discussed in the earlier chapters, laser-polarized noble gas possesses a large magnetization and is inherently out of thermal equilibrium. In addition, it typically exhibits long T_1 times in certain environments. These factors thus require modified NMR techniques for laser-polarized noble gas experiments. Frequently, low flip angles (i.e., $\theta \ll \pi/2$) are used with laser-polarized noble gas because of the high magnetization available; also, this conserves the long-lived magnetization for further experiments. However, spin echoes are usually inappropriate because they require using all the magnetization (not just a small portion of it); hence gradient echoes techniques are common in NMR sequences designed for laser-polarized noble gas. In cases where T_2^* is a limiting factor (e.g., in heterogeneous porous media), one must either consider using spin echoes in the sequence and modify the method of introducing polarized gas (e.g., via a continuous flow system, such as one we are currently developing), or operate at low magnetic fields where magnetic susceptibility mismatches (which often dominate T_2^*) are reduced, as demonstrated in Chapter 4.

3.2 Experimental considerations

Most laser-polarized noble gas NMR and MRI experiments (including some described in this dissertation) are performed with commercial instruments (e.g., at hospital radiology facilities). Since conventional NMR and MRI utilize nuclear spin magnetization arising from the Boltzmann distribution – which in turn is dependent on the applied magnetic field – the trend in magnet development is to push for greater magnetic fields[2]. For both safety and economic concerns, clinical magnets typically operate between 1.5 and 3 T; smaller horizontal bore animal research magnets commonly operate at 4.7 T; and narrow vertical bore high resolution spectroscopy magnets are available at fields in excess of 18 T. The key consideration for performing NMR and MRI experiments with laser-polarized noble gas at such facilities is that the gyromagnetic ratios of both ^{3}He and ^{129}Xe are significantly different from commonly detected NMR nuclei (c.f., Table 1.2)[3].

As a result, it is necessary to address the following questions:

(i) can the spectrometer/imager operate at the noble gas Larmor frequency?

(ii) is an RF coil of appropriate geometry available that can be tuned to the noble gas Larmor frequency?

If the spectrometer/imager does not accommodate Larmor frequencies other than those of standard nuclei (e.g., ^{1}H or ^{13}C), it will be necessary to install mixers and a supplemental frequency synthesizer to allow the spectrometer to work at these non-standard frequencies. Also, the software that controls the NMR experiment will need to be scrutinized to ensure that parameters are not determined with erroneous

[2]It is also possible to construct a modest NMR system that operates at much lower fields with non-superconducting magnets, and in later chapters we discuss our own such home-made low field system for use with laser-polarized noble gas.

[3]Actually, the gyromagnetic ratio of ^{129}Xe is similar to that of ^{13}C, the second most detected NMR nuclei in chemistry ($\gamma_{^{129}Xe}/\gamma_{^{13}C} = -1.1003$). However, MR-imagers are usually not equipped to detect ^{13}C.

assumptions about the Larmor frequency. Concerning RF excitation and detection coils, it is rare that existing coils for other nuclei can be tuned to a noble gas Larmor frequency. Consequently, a customized coil will either need to be ordered or built.

As a final practical matter, one should also investigate if it is possible to site an optical pumping apparatus in the fringe field of the magnet. As was discussed in section 2.3, laser-polarizing noble gas requires an orientation field coincident with the propagation vector of the polarizing light. At convenient distances ($\sim$ 1 m) from the magnet, it is frequently possible to find fields of several hundred gauss for this purpose. Of course, one must also ensure the associated equipment for the optical pumping is either located further away (in a lower magnetic field environment), or is capable of working at an elevated magnetic field. For example, the Opto Power lasers we use tended to fail quickly when sited in a field higher than 50 G. However, with a 5 meter fiber cable installed, they could be placed in a safer (lower) field and still illuminate an optical pumping cell placed at high field. If pumping in the fringe field is not possible, then constructing a polarizing field (e.g., with Helmholtz coils) for the optical pumping apparatus will be necessary.

3.3 Basic measurement techniques

We now describe a number of commonly used NMR pulse sequences that have been modified for use with laser-polarized noble gas experiments. In some cases the conventional technique is also described, but the interested reader is encouraged to peruse texts such as Abragam [70], Wehrli *et al.* [71], Callaghan [72], Slichter [67] and Ernst *et al.* [73] for more complete discussions of standard techniques.

3.3.1 Polarization, flip angles, and longitudinal relaxation

The amount of polarization in a sample of laser-polarized noble gas is usually determined by comparing its NMR signal to that of a thermally-polarized sample; the polarization of the latter is given by a Boltzmann distribution (i.e., directly proportional to the magnetic field strength and temperature at room temperatures) and can be calculated explicitly (see eq. 1.1). Of course, different factors such as sample volumes, dissimilar nuclear magnetic moments and natural abundances, number densities, and coil Qs (if using different nuclei for calibration) must be taken into account.

For example, consider a simple case where we obtain a laser-polarized noble gas NMR signal of strength S_{ng} after exciting some portion of the magnetization (i.e., applying an RF pulse, which rotates some of the longitudinal magnetization by an angle α into the transverse plane and through Faraday induction yields a detected signal S_{ng}). In order to determine the noble gas polarization P_{ng}, we compare S_{ng} to the signal S_t from a thermally polarized sample (e.g., water). In particular, the magnitude S of any NMR signal can be expressed as follows:

$$S = \mu P V \rho \eta \zeta \sin(\theta) \omega Q, \tag{3.5}$$

where μ is the nuclear magnetic moment, P is the polarization, ρ is the density of the nuclear species, η is the isotopic abundance, ζ is the filling factor, θ is the RF excitation "flip angle" (which determines how much the magnetization vector has been rotated into the transverse plane), and ω is the Larmor frequency. Assuming that the thermal signal is excited by a $\pi/2$ pulse (i.e., $\sin(\theta) = 1$ in eq. 3.5), we have

$$P_{ng} = \frac{S_{ng}}{S_t} \frac{1}{\sin(\alpha)} \left(\frac{\omega_t}{\omega_{ng}} \right)^2 \left[\frac{V_t \rho_t \eta_t Q_t}{V_{ng} \rho_{ng} \eta_{ng} Q_{ng}} \right] P_t. \tag{3.6}$$

P_t is the polarization expected for a (thermal) Boltmann distribution given the magnetic field strength and temperature; it also depends on the magnetic moment μ_t of the thermally polarized nuclei (c.f., eq. 1.1).

Of the variables in eq. 3.6, the flip angle α is not known *a priori*. In principle, α is given by $\gamma_{ng} B_1 \tau_{RF}$, where γ_{ng} is the gyromagnetic ratio (in radians $\mathrm{G}^{-1}\ \mathrm{s}^{-1}$) of the noble gas nuclei, B_1 is the strength (in G) of the RF field, and τ_{RF} is the duration of the pulse. Thus α can be varied by changing the pulse duration or magnitude of B_1 (by typically changing the RF power of the pulse). Experimentally, we can determine α by first using the simple pulse sequence shown in Fig. 3.3. It begins with an RF pulse (α), and the resulting FID is recorded. Before the next α pulse, a "crusher" gradient is pulsed to dephase any remaining transverse magnetization. This sequence is then repeated as often as desired (e.g., 8 or 16 times). The time between two consecutive RF pulses is parameterized by T_R. Each FID amplitude

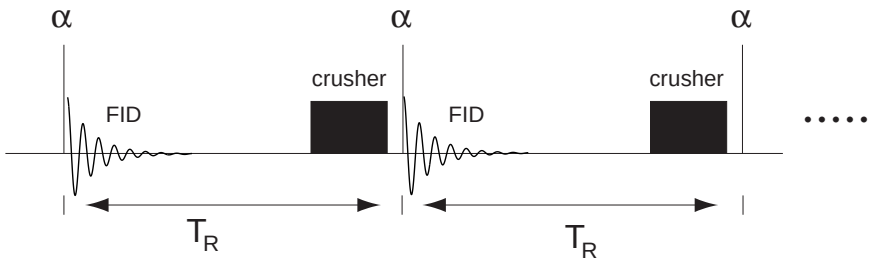

Figure 3.3: Simple pulse sequence for determining flip angle α and longitudinal relaxation time T_1.

is proportional to the transverse magnetization resulting from the RF excitation pulse; in other words, it is the projection of the magnetization vector $\mathbf{M}$ onto the transverse plane after the RF pulse has rotated it away from $\hat{z}$ by an angle α. In a sample without additional sources or sinks of magnetization, M_z diminishes over time due to two causes: longitudinal (T_1) relaxation and losses due to each RF pulse.

The sequence of FID amplitudes should therefore proceed as follows:

$$\begin{aligned} S_0 &\propto M_0 \sin(\alpha) \\ S_1 &\propto M_0 \cos(\alpha) \sin(\alpha) e^{-\frac{T_R}{T_1}} \\ S_2 &\propto M_0 \cos^2(\alpha) \sin(\alpha) e^{-\frac{2T_R}{T_1}} \\ &\vdots \\ S_n &\propto M_0 \cos^n(\alpha) \sin(\alpha) e^{-\frac{nT_R}{T_1}} \end{aligned} \tag{3.7}$$

Taking the natural logarithm of eq. 3.7, we have

$$\ln S_n \propto \ln \left[M_0 \sin(\alpha) \right] + n \left[\ln(\cos(\alpha)) - T_R/T_1 \right] \tag{3.8}$$

The first term of the right hand side is merely a constant, while the second term is linear in n. Therefore, we expect that $\ln S_n$ plotted against n should yield a straight line, with the slope (m) equal to $\ln(\cos(\alpha)) - T_R/T_1$. In order to measure α, we typically use a short T_R such that $T_R \ll T_1$; thus the term T_R/T_1 can be ignored and

$$\alpha \approx \cos^{-1}(e^m). \tag{3.9}$$

Knowing α, one can return to eq. 3.6 and determine the polarization of the noble gas. Also, it is possible to repeat this experiment with a longer T_R such that T_R/T_1 cannot be ignored, and since α has been determined, one can measure T_1 (i.e.,

$$T_1 = T_R / \left[\ln \cos(\alpha) - m' \right], \tag{3.10}$$

where m' is the slope of the linear fit to the long T_R data).

The method just outlined is applicable in situations where T_1 is very long (tens

of minutes to hours), such that T_R can be varied as required. For example, for our OTS-coated sealed glass phantoms filled with ^{129}Xe, N_2, and some Rb, we typically measured ^{129}Xe T_1's in excess of 2 hours at magnetic fields > 1 T. Figure 3.4 is an example of data taken with $T_R = 1$ s ($\ll T_1$); this allowed us to determine the flip angle $\alpha = 10.4°$ in this particular case. Using this value, we increased T_R to 120 s and assuming $\alpha = 10.4°$, we found that the ^{129}Xe $T_1 = 9293 \pm 39$ s (see Fig. 3.5).

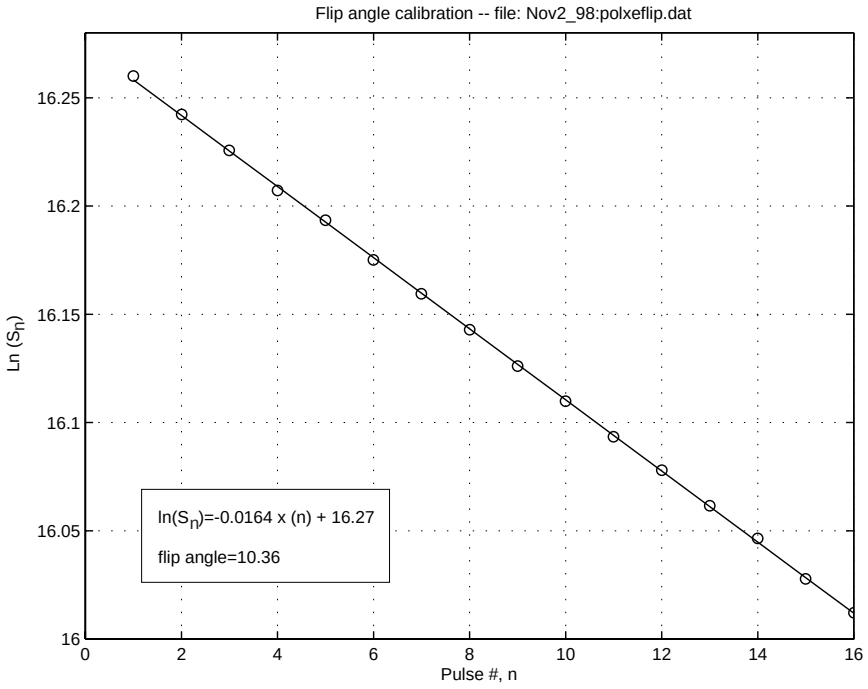

Figure 3.4: Flip angle calibration using a laser-polarized ^{129}Xe cell P-2 at 4.7 T. The natural logarithm of 16 FID amplitudes ($\ln(S_n)$) is plotted against the pulse number, n. $T_R = 1$ second. The line shown is a linear least-squares fit to the data, and has a slope of -0.0164. Since $T_R \ll T_1$, we find $\alpha = 10.4°$.

As we shall discuss in more detail in Chapter 6, typical ^{129}Xe T_1 times are much shorter at low magnetic fields ($\ll 1$ T), to the extent that choosing a $T_R \ll T_1$ may not be practical. Nonetheless, it is still possible to determine T_1 and α using the pulse sequence shown in Fig. 3.3. If we repeat this experiment k times with a series

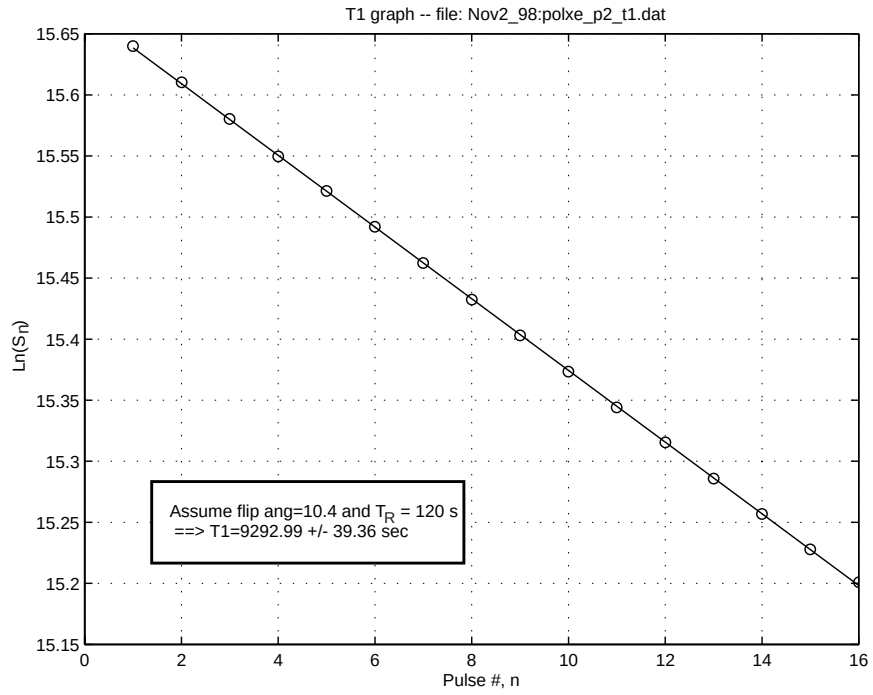

Figure 3.5: Laser-polarized ^{129}Xe T_1 measurement in cell P-2 at 4.7 T. The natural logarithm of 16 FID amplitudes ($\ln(S_n)$) is plotted against the pulse number, n. $T_R = 120$ seconds. The line shown is a linear least-squares fit to the data, and has a slope of -0.0049. Using $\alpha = 10.4°$ from the measurement shown in Fig. 3.4, we find that $T_1 = 9293 \pm 39$ s.

of different T_R values, we can fit different lines to each run such that

$$m_j = \ln(\cos(\alpha)) - \tau_j/T_1. \tag{3.11}$$

m_j is the linear coefficient of the least-squares fit for the experiment where $T_R = \tau_j$. It is clear that m_j is linear in τ_j, and a linear least-squares fit of m_j vs. τ_j will yield an intercept equal to $\ln(\cos(\alpha))$ and a slope equal to $-1/T_1$ (see Fig. 3.6). Note that no assumptions about the relation between the values of $\{\tau_j\}$ and T_1 are required[4].

[4]However, the accuracy of this method will improve if the τ_j are chosen over a wide range with respect to T_1

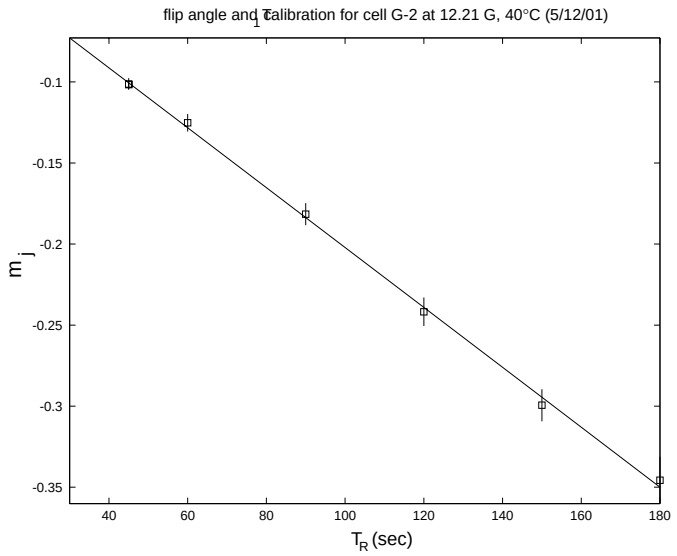

Figure 3.6: Laser-polarized ^{129}Xe flip angle and T_1 measurement at 12.21 G by varying T_R (cell G-2). 6 different T_R were used (i.e., $\tau_j = [45, 60, 90, 120, 150, 180]$ seconds). At this field strength, the ^{129}Xe Larmor frequency is 14.38 kHz. Note that each point represents the slope of a graph similar to those shown in Fig. 3.4 and 3.5. From this data, we conclude that the ^{129}Xe T_1=542±18 s and $\alpha = 11.0 \pm 1.2°$.

For comparison, calibrating the flip angle and measuring T_1 in a thermally polarized sample is quite different. Since thermally polarized nuclei such as ^{1}H in water have relatively fast (∼second) T_1's, one usually just employs $\pi/2$ pulses, which can be calibrated by adjusting the pulse power or duration until the FID signal is maximized. To measure T_1, a sample is then subject to the following pulse sequence:

$$\pi \xrightarrow{\tau_j} \pi/2 - (\text{acquire FID}) \xrightarrow{\sim 5T_1} \text{repeat}.$$

This is known as the "inversion recovery" sequence, and was first proposed by Vold *et al.* [74]. The delay τ_j between the π and $\pi/2$ pulses is varied from nearly zero to a few times T_1, and this sequence is repeated after the magnetization has returned to thermal equilibrium (e.g., $\sim 5 \times T_1$). The resulting series of FIDs, when phased

properly, follows the relationship

$$S_j \propto M_0[1 - 2\exp(-\tau_j/T_1)], \tag{3.12}$$

and it is straightforward to solve for T_1.

3.3.2 Diffusion measurements

Measuring the diffusion of gas in different environments is among the more interesting NMR applications for laser-polarized noble gas; in particular, the high polarization and fast diffusion create opportunities for studies of porous media [19] and the lungs [75].

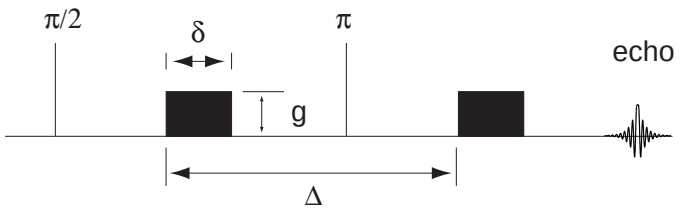

Figure 3.7: The PGSE sequence.

A standard pulse sequence used to measure diffusion is the "Pulsed Gradient Spin Echo" (PGSE) sequence, first introduced by Stejskal and Tanner in 1965 [76]; it is illustrated in Fig. 3.7. After the initial $\pi/2$ RF pulse, a magnetic field gradient pulse of strength g and duration δ "winds" a spatially varying phase onto the transverse magnetization $M_\perp$. In particular, the accumulated phase $\Delta\phi(u)$ along the gradient direction $\hat{u}$ is given by

$$\Delta\phi(u) = \left(\gamma \int_0^\delta g(t)dt\right) u \equiv ku, \tag{3.13}$$

where k is the wavenumber of the modulation or 'grating' of $M_\perp$ and u is the spatial variable. In the simple case of a square gradient pulse with amplitude g and duration δ (as shown in Fig. 3.7), $\Delta\phi(u) = \gamma g \delta u$, and hence $k = \gamma g \delta$.

The π RF pulse reverses the sense of all the phases by inverting one component of $M_\perp$; the subsequent gradient pulse of equal amplitude and duration as the first one then allows all the spins to refocus (i.e., $\Delta\phi(u) \to 0$). This generates a spin echo and is recorded. If the spins did not move at all during this sequence, one would expect perfect refocussing of the phase modulations, and the resulting spin echo would have an amplitude attenuated only by any spin decoherence (T_2) losses in the time between the initial RF excitation and the echo acquisition. However, diffusion causes random atomic and molecular motion and results in imperfect phase refocussing after the second gradient pulse. The diffusive attenuation is determined by g, δ, Δ – all of which are controlled by the NMR spectrometer – and of course the diffusion coefficient D. By varying one of the experimental parameters and repeating the experiment a number of times, it is possible to determine D.

For a more detailed explanation, consider the following: let $\psi(x,t)$ be a complex-valued function of position x and time t (i.e., the transverse magnetization $M_\perp$); assume $|\psi(x,t)| \leq 1$. Under 1D diffusion, ψ obeys Fick's Law:

$$\frac{\partial \psi(x,t)}{\partial t} = D \frac{\partial^2 \psi(x,t)}{\partial x^2}. \tag{3.14}$$

Now the initial part of the PGSE sequence is equivalent to creating an initial condition in $\psi(x,t)$ such that $\psi(x,t) = A(t)\exp(ikx)$, where $A(t)$ is a time-dependent amplitude, and $\exp(ikx)$ is a spatial phase modulation with wavenumber k. Solving

eq. 3.14 is straightforward using integration by parts, and the solution is simply

$$\psi(x,t) = \exp(-k^2 Dt)\exp(ikx). \tag{3.15}$$

For a given x, we could determine the diffusion coefficient D if we could measure $\psi(x,t)$ at different times with fixed k, or alternatively with fixed t and varying k.

However, in NMR the signal collected is integrated over the whole sample, and thus $\int \psi dx \to 0$ due to the $\exp(ikx)$ modulation. The π pulse and second gradient pulse of the PGSE sequence effectively remove the $\exp(ikx)$ dependence from $\psi(x,t)$, and thus the echo is proportional to $\exp(-k^2 D\Delta)$, where Δ is the diffusion time and k is determined by g and δ (see eq. 3.13).

In reality, the NMR experiment is only slightly more complicated to analyze, since one must also take into account diffusion that occurs during the finite time δ of each gradient pulse. Also, it is possible to generalize the experiment to account for bulk flow as well as diffusion; whereas the latter results in attenuation of the echo amplitude, the former causes a net phase shift of the echo. The resulting echo amplitude $\mathcal{E}$ is [72, 76, 77]:

$$\mathcal{E} = \exp\left[i\mathbf{k}\cdot\mathbf{v}\Delta - k^2 D\Delta'\right]. \tag{3.16}$$

with the following definitions:

$$\begin{aligned} \mathbf{v} &= \text{velocity vector of bulk flow} \\ \mathbf{k} &= \gamma\textstyle\int^{\delta}\mathbf{g}(t)dt \\ \Delta' &= \text{the ``reduced observation'' time [72]} \end{aligned}$$

Commonly, the gradients are rectangular or half-sinusoidal pulses (the latter reduce the eddy current distortions that arise from fast switching of large magnetic field

gradients), and explicitly give the following expressions for $|k|$ and Δ':

$$|k| = \begin{cases} [\gamma\delta g(2/\pi)] & \text{for sinusoidal gradient pulses} \\ [\gamma\delta g] & \text{for rectangular gradient pulses} \end{cases}$$

$$\Delta' = \begin{cases} (\Delta - \delta/4) & \text{for sinusoidal gradient pulses} \\ (\Delta - \delta/3) & \text{for rectangular gradient pulses} \end{cases}$$

It is common practice to record several echo amplitudes $\mathcal{E}$ while changing Δ or g. Thus, a plot of $\ln(\mathcal{E})$ versus Δ (or g^2) should yield a straight line whose slope is equal to the product of D and g^2 (or Δ).

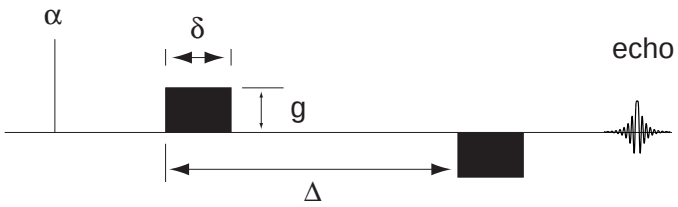

Figure 3.8: The PGE sequence.

For laser-polarized noble gas, one cannot use the PGSE sequence as shown in Fig. 3.7 because after a single run of the experiment, all the polarization would be depleted and additional laser-polarization of the noble gas would be required. Since the measurement requires multiple runs to acquire a series of varying echo amplitudes, we must instead consider a way to repeat the experiment using only a portion of the available polarization each time. The solution is to use a modified form of the PGSE sequence, known as the "Pulsed Gradient Echo" (PGE), which is shown in Fig. 3.8 [78].

Instead of placing all the magnetization into the transverse plane as the PGSE sequence does with its initial $\pi/2$ pulse, the PGE sequence uses only a fraction of its magnetization (i.e., $\mathbf{M}\sin(\alpha)$). The first gradient, as before, creates a spatially

varying phase in the magnetization, which then evolves over a time set by Δ. In place of a [π - (gradient pulse)] to refocus the spins, the PGE sequence simply uses an inverse gradient pulse to accomplish the same thing. However, one of the shortfalls of this method is that it is sensitive to T_2^* decoherence, as mentioned in section 3.1.

Furthermore, one must use an increasing flip angle α in order to begin each experiment with the same amount of transverse magnetization $M_\perp$. If we assume that the experiment is repeated quickly relative to T_1, then we can determine the sequence of α's needed by writing

$$\begin{aligned} M_\perp^{(0)} &= M_0 \sin(\alpha_0) \\ M_\perp^{(1)} &= M_0 \cos(\alpha_0) \sin(\alpha_1) \\ M_\perp^{(2)} &= M_0 \cos(\alpha_0) \cos(\alpha_1) \sin(\alpha_2) \\ &\vdots \\ M_\perp^{(n)} &= M_0 \left[\prod_{m=0}^{n-1} \cos(\alpha_m) \right] \sin(\alpha_n) \end{aligned} \tag{3.17}$$

Ideally, we want $M_\perp^{(n)}/M_\perp^{(n-1)} = 1$, which leads to the iterative relationship:

$$\tan(\alpha_{n-1}) = \sin(\alpha_n) \tag{3.18}$$

An example of data taken using the PGE sequence is shown in Fig. 3.9. The sample is laser-polarized ^{129}Xe in cell P-2 (OTS-coated sealed glass cell with 3 atm of 90% enriched ^{129}Xe, 0.13 atm N_2, and some Rb metal).

For completeness, I mention three other diffusion measurements which have been used in conjunction with laser-polarized gases. The first is known as "time-dependent" diffusion [19,78], and is useful for studying samples where the noble gas

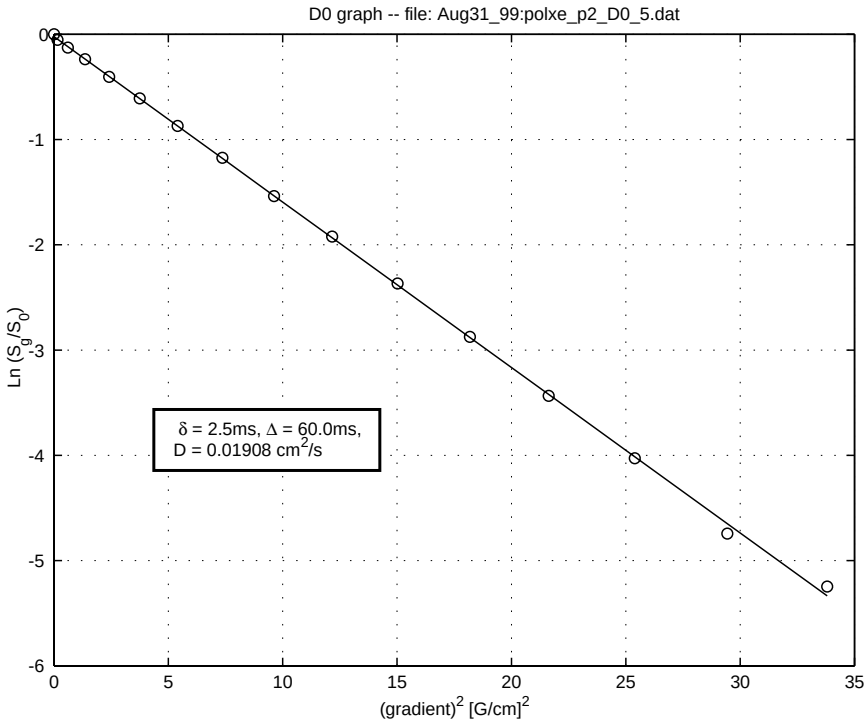

Figure 3.9: Example of laser-polarized ^{129}Xe diffusion data using the PGE sequence. To keep the transverse magnetization constant for each echo acquisition, a varying flip angle was used (i.e., $\alpha = [10, 10.16, 10.32, 10.49, 10.67, 10.86, 11.06, 11.27, 11.5, 11.74, 11.99, 12.26, 12.55, 12.87, 13.20, 13.57]$); $\delta = 2.5$ ms, $\Delta = 60$ ms. From this measurement, the diffusion coefficient $D_0 = 0.019$ cm^2/s, which is consistent with measurements made with PGSE NMR and other techniques.

fills some sort of pore space. The measurement is basically the same as PGSE or PGE, except that now both Δ and g will be varied; one then finds that the effective diffusion coefficient is not the same for all time scales. In particular, $D = D(t)$, where it is common practice in making such measurements to equate t and Δ. For small t (i.e., small Δ), we expect that $D(t)$ will be similar to the free gas diffusion coefficient D_0. However, for larger t, the size of the pore space begins to restrict the movement of the gas and is manifest in an apparently smaller diffusion coefficient. Specifically, $D(t)$ depends on the surface-to-volume ratio of the pore (S/V_p), until the diffusion length $\sqrt{D_0 t}$ begins to approach a fraction of the mean pore diame-

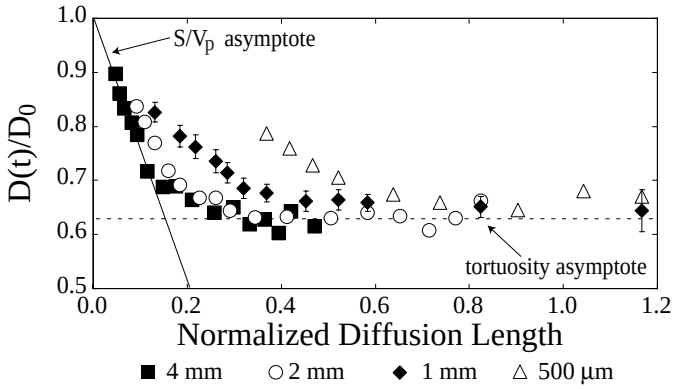

Figure 3.10: Time-dependent diffusion measurements for thermally polarized xenon gas in randomly packed spherical glass beads. Each sample contains beads of a uniform diameter b, as indicated in the legend. Data is shown as the time-dependent diffusion coefficient normalized to the free gas diffusion coefficient, $D(t)/D_0$, as a function of the free gas diffusion length in the time t normalized to the bead diameter, $\sqrt{D_0 t}/b$. Error bars are shown for the 1 mm beads and are similar for the other measurements. The calculated limits at short time (surface-area-to-volume ratio, S/V_p) and long time (tortuosity, α) are shown by the solid and dashed lines, respectively. For dense spherical bead packs, porosity $\phi = 0.39$, $1/\alpha \approx \sqrt{\phi} = 0.63$, and $S/V_p = 6(1-\phi)/(\phi b) = 9.38/b$. *Figure and caption taken from ref. [19].*

ter. At greater diffusion lengths (i.e., longer times), the $D(t)$ measurements reveal the *tortuosity* of the media, which is a characteristic of the interconnectivity of the pores. Figure 3.10 illustrates a series of such "restricted diffusion" measurements that were performed in samples of randomly packed glass beads.

A crude technique to measure diffusion in laser-polarized noble gas is simply a "hole-burning" or "bleaching" method [79–81], where by a small "slice" of the magnetization is depleted by a saturating RF pulse. This can be done by applying a narrow-frequency excitation (known as a "soft" pulse) onto the polarized gas while a linear magnetic field gradient is simultaneously applied. The width of the zero-magnetization slice is determined by the frequency-selectivity of the pulse and the strength of the magnetic field gradient applied. Once this slice of magnetization is depleted, one simply images the sample profile and watches as diffusion "fills" the

hole (imaging will be discussed in the next section). This technique has limited spatial and temporal resolution.

Finally, Peled and coworkers suggested a novel "single-shot" diffusion measurement (SSDM) [26]. Whereas a PGE sequence must be repeated multiple times with differing g values (assuming fixed Δ), the SSDM method creates an overlay of a discrete set of spatial phase modulations. Multiple echoes are subsequently acquired, with each containing amplitude information for all desired g values, which can then be used to determine D. A more thorough analysis of the sequence is facilitated by the "k-space" formalism, which we review in Chapter 5; in fact, the SSDM method is very similar to the "quasi-random encoding" sequence we used for the 1-D persistence measurement (also described in Chapter 5).

3.3.3 Imaging

A common theme in conventional pulse sequences (for thermally-polarized samples) is using $\pi/2$ and π pulses to maximize the available signal and create spin echoes. Since many experiments (such as imaging) rely on repeating the sequence with different parameters, one must simply use a delay equal to a few multiples of the T_1 between repetitions. This allows the system to return to thermal equilibrium and have sufficient magnetization to yield an NMR signal. With laser-polarized noble gas, however, using $\pi/2$ and π pulses are usually inappropriate as they deplete all of the available magnetization and thus cancels the possibility of further repetitions of the sequence[5]. Consequently, the laser-polarized noble gas sequences we have discussed use low flip angles and gradient echoes to circumvent this problem. As they do not require a wait of several T_1 before repeating the sequence, they can

[5]This limitation is of course lifted if a way is engineered to deliver "fresh" polarized gas to the experimental sample, either by discrete batches or by a continuously flowing system.

often run much faster than their conventional sequence counterparts.

The basic technique for imaging laser-polarized gas was developed several years ago, albeit for a different reason. The technique, known as Fast Low-Angle SHot (FLASH), was introduced in 1986 by Haase *et al.* [82] as a way to acquire NMR images faster without having to be limited by T_1. Fortunately, it is perfectly well-suited to laser-polarized noble gas imaging. In the remainder of this section we will review the basic imaging process and the FLASH sequence, with concluding remarks on variations that are particularly useful for laser-polarized nuclei.

Broadly speaking, imaging is the process of recording (on a photographic plate or binary data file) the spatial distribution of some quantity, such as light of a particular color. Specifically, in MRI it is the distribution and density of nuclear spins that are recorded, weighted by local environments and convolved with magnetic field homogeneity and RF coil geometry. Let $\rho(\mathbf{r})$ represent the distribution of nuclear spins, [^{1}H (e.g., in water) or a polarized noble gas (^{3}He, ^{129}Xe)]. The NMR signal $S(t)$ detected from this distribution is always integrated over the volume, i.e.,

$$S(t) = A \int \rho(\mathbf{r}) \exp(i\omega t) d\mathbf{V}. \tag{3.19}$$

Here, A is a constant proportional to the nuclear magnetic moment, coil Q, and Larmor frequency ω. Eq. 3.19 is very similar to the fourier transform of $\rho(\mathbf{r})$ – it only requires that the exponential argument have a linear dependence on position. This can be accomplished by applying linear magnetic field gradients after the initial excitation RF pulse, but before and/or during the signal acquisition. An applied gradient pulse before the signal is acquired would result in a position-dependent *phase*, while a gradient applied during the signal acquisition would cause a position-dependent *frequency*; the creation of such spatial dependence in the magnetization

is called "phase-encoding" and "frequency-encoding," respectively.

Consider two orthogonal linear field gradients $\partial B_z/\partial x$, and $\partial B_z/\partial y$, which we shall call G_{read} and G_{phase}[6]. The resultant NMR signal can be expressed as follows:

$$S(t_1, t_2) = A \int\int \rho(x, y) \exp\left\{ i \left[\omega t_1 + \gamma \left(\int^{t_1} G_{\text{read}} x dt \right) + \gamma \left(\int^{t_2} G_{\text{phase}} y dt \right) \right] \right\} dx dy. \tag{3.20}$$

Without loss of generality, we have assumed a "slice" of uniform thickness in the $\hat{z}$ direction, and are only concerned with acquiring an image in the xy plane. t_1 is actually the time variable while the signal is being acquired, while t_2 is the duration of the phase-encode gradient pulse applied prior to signal acquisition.

At this point the discussion is simplified if we explicitly change to the familiar spatial fourier conjugate variables k_x and k_y, such that $k_x = \gamma \left(\int^{t_1} G_{\text{read}} dt \right)$ and $k_y = \gamma \left(\int^{t_2} G_{\text{phase}} dt \right)$. Up to some constant factor, we can therefore rewrite eq. 3.20:

$$S(k_x, k_y) = A' \exp(i\omega t_1) \int\int \rho(x, y) \exp\left\{ i \left(k_x x + k_y y \right) \right\} dx dy. \tag{3.21}$$

The exponential $\exp(i\omega t_1)$ is just the carrier frequency, while the integral is the fourier transform of $\rho(x, y)$. Since k_x is a function of t_1 (the signal acquisition time variable), the NMR signal recorded represents a "line" of values $S(k_x, k_y)$ where k_y is held constant. To change k_y, we repeat the experiment with a different G_{phase}. This method is known as "spin warp imaging" and was introduced by Edelstein *et al.* in 1980 [83]; a simple depiction of how one traverses k-space to acquire $S(k_x, k_y)$ is shown in Fig. 3.11.

Now one question that naturally arises is how one may obtain data for negative values of k_x and k_y; in the latter case, it is a simple matter of reversing the polarity

[6]These are common NMR labels for the gradients. For example, G_{read} will be the frequency-encoding gradient, which is applied when the signal is *read* out.

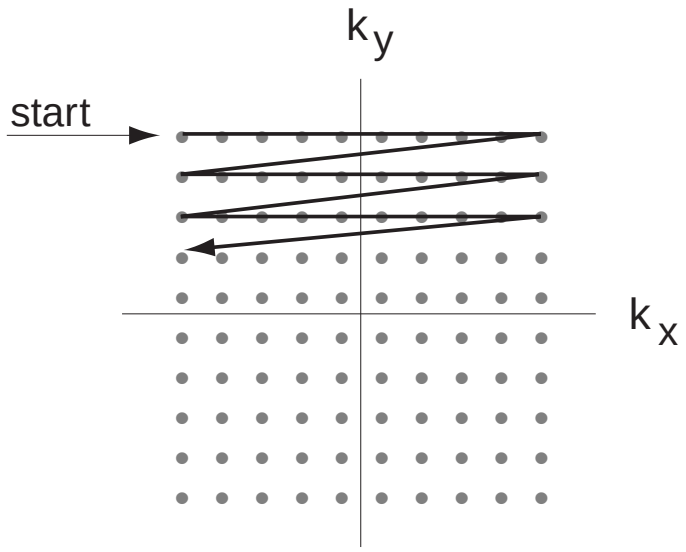

Figure 3.11: Spin warp imaging – the progression through k-space. Lines of k_x are acquired with each NMR signal, while moving to a different k_y line requires a repeat of the imaging experiment with a different G_{phase} magnitude.

of G_{phase}, whereas for k_x we must acquire an echo (which effectively yields both negative and positive time information if we define the echo maximum as $t = 0$). Typically, one uses a π pulse to induce a spin echo, but as we mentioned earlier, gradient echoes are better suited for laser-polarized noble gas.

Understanding the FLASH sequence (shown in Fig. 3.12) is straightforward. A low flip angle RF pulse α is used to excite some magnetization into the transverse plane; the G_{phase} pulse sets a particular k_y value, and then the G_{read} gradient is pulsed in a way to yield a frequency encoded gradient echo. Once an echo is acquired, the sequence is repeated with a new low flip angle RF pulse, a different G_{phase} (and hence a different k_y), and so on. An image is then formed by a simple 2-D fourier transform of all the acquired data.

For some samples, the T_1 of laser-polarized noble gas is very short, and this may be of concern if the time to acquire a set of image data is comparable to T_1. For

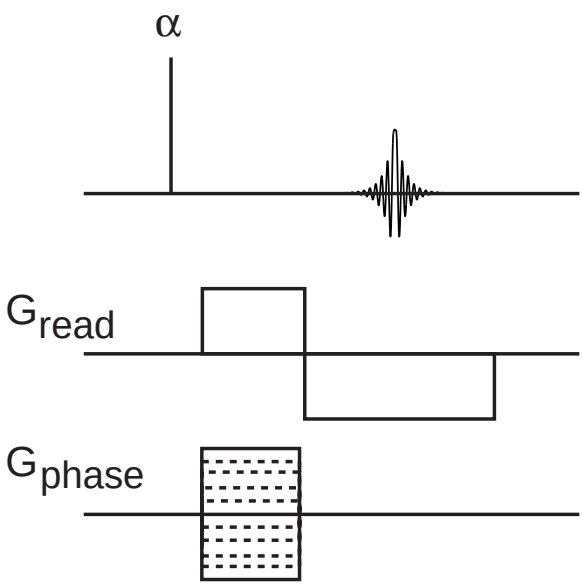

Figure 3.12: The FLASH imaging sequence.

example, our low field imaging FLASH sequence required $\sim$ 25 s to acquire all the data (due to our instrument hardware limitations), which is comparable to the $T_1 \sim$ 16–63 s we measured inside of excised rat lungs (as described in section 4.2). Under these circumstances, it is desirable to first acquire the lower spatial frequency data first, and if sufficient magnetization exists, to then continue with higher order data acquisition. In other words, rather than progress linearly from $-k_y^{max}$ to $+k_y^{max}$, it is preferable to start at $k_y = 0$ and then acquire data for increasing values of $|k_y|$. Figure 3.13 illustrates the meandering path through $k-$space implied by this algorithm (also known as concentric encoding [84]).

Another factor to consider when using the FLASH sequence is whether or not to use variable flip angles (see eq. 3.18). Each α pulse depletes the longitudinal magnetization by an amount $[1 - \cos(\alpha)]$. Consequently, each successive NMR signal arises from less and less transverse magnetization; using a variable flip angle would therefore normalize each NMR signal to the same initial transverse magnetization.

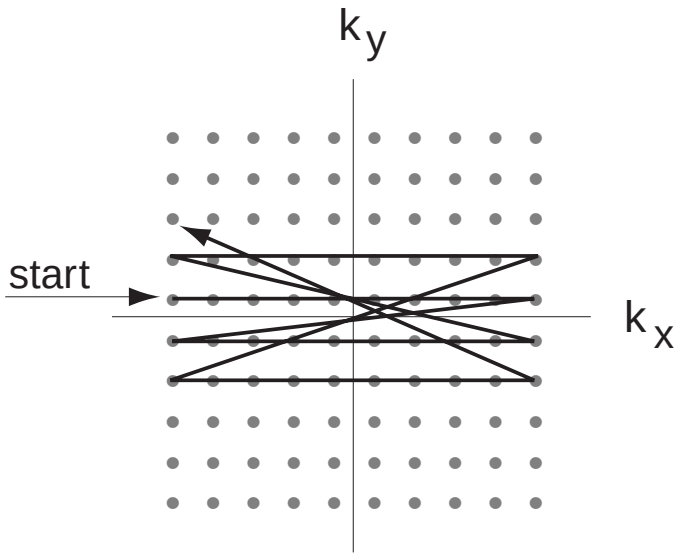

Figure 3.13: Concentric imaging – the progression through k-space. Lines of k_x are acquired with small $|k_y|$ *first*, with successively higher k_y acquired at later times.

However, if α is initially very small and only a small number of phase encodes will be acquired (e.g., $\alpha_0 < 9^\circ$ and k_y steps ≤ 32), there may be little noticeable improvement.

Finally, it should be noted that one can acquire 1-D images (also referred to as "profiles") by turning off G_{phase}. This is equivalent to obtaining only the $k_y = 0$ line of k-space, and represents the spatial distribution of spins along the G_{read} direction integrated over the other 2 orthogonal axes. The persistence measurement described in Chapter 5 relies on this manner of imaging.

Chapter 4

Low Field Imaging

This chapter consists of two papers describing our MRI experiments using laser-polarized noble gas at low magnetic fields. The first paper, entitled "Low-Field MRI of Laser Polarized Noble Gas", appeared in *Physical Review Letters,* **81**, pp. 3785–3788 (1998). It describes our first demonstrations of low field imaging and explores some of the inherent advantages, such as reduced magnetic susceptibility effects and greater RF transparency.

The second paper ("A System for Low Field Imaging of Laser-Polarized Noble Gas", *Journal of Magnetic Resonance*, **141**, pp. 217–227 (1999)) describes in more detail the experimental apparatus we built for performing low field imaging. It also presents new results (i.e., the first low field biological image) and demonstrates the effects of radiation damping on standard measurements such flip angle calibrations.

The work presented here is the result of a collaboration between the Harvard-Smithsonian Center for Astrophysics, the Massachusetts Institute of Technology, the University of New Hampshire, the Massachusetts General Hospital, and the Brigham and Women's Hospital.

4.1 Low-Field MRI of Laser Polarized Noble Gas

C. H. Tseng, G. P. Wong, V. R. Pomeroy, R. W. Mair, D. P. Hinton, D. Hoffmann, R. E. Stoner, F. W. Hersman, D. G. Cory, and R. L. Walsworth

Physical Review Letters *vol.* ***81****, pp. 3785–3788 (1998).*

This article has been reformatted to conform to Harvard dissertation guidelines and is reprinted with permission.

NMR images of laser polarized ^{3}He gas were obtained at 21 G using a simple, homebuilt instrument. At such low fields magnetic resonance imaging (MRI) of thermally polarized samples (e.g., water) is not practical. Low-field noble gas MRI has novel scientific, engineering, and medical applications. Examples include portable systems for diagnosis of lung disease, as well as imaging of voids in porous media and within metallic systems.

In this paper we demonstrate a powerful diagnostic technique: NMR imaging at low magnetic fields using laser polarized noble gas. Conventional magnetic resonance imaging (MRI) employs large magnetic fields ($\sim$1 T) to induce an observable thermal Boltzmann polarization in the nuclear spins of liquids such as water. MRI is a minimally invasive imaging technique with enormous impact in the biomedical and physical sciences. Examples include diagnostic clinical medicine [85], biological research, such as mapping of brain function [86], materials science (e.g., imaging the flow of shaken granular media [87]), and soft condensed matter physics, such as imaging the coarsening of foams [88]. Nevertheless, the large magnetic fields of conventional MRI require cumbersome and expensive equipment, and limit the technique's scientific and practical applications [89].

As demonstrated in this paper, the greatly increased nuclear spin polarization of the noble gases ^{3}He and ^{129}Xe, provided by optical pumping techniques ("laser polarization") [90], enables efficient gas-phase MRI at low magnetic fields ($\sim$ 10 G) using a simple, small, and inexpensive device. With this demonstration, the door

is opened to a wide variety of new MRI applications. Examples in the biomedical field include portable systems for diagnostic lung imaging in humans [18, 91–96], and low-cost tabletop MRI instruments for research in animals. Furthermore, a low-field noble gas MRI system would be compatible with operation in restricted environments, such as on board a space station, and may permit lung imaging of patients with artificial transplants such as pacemakers [97].

In the physical sciences, low-field noble gas MRI will be effective in imaging voids in two classes of materials that are problematic for high-field MRI: (i) heterogeneous systems, such as porous and granular media, which distort high-field images because of large, solid-gas magnetic susceptibility gradients; and (ii) electrical conductors, which prevent high-field MRI by Faraday (i.e., rf) shielding. Also, low-field NMR measurements of the restricted diffusion of noble gas imbibed in porous media (e.g., reservoir rock) may provide an effective and practical diagnostic of fluid permeability in such media.

At low magnetic fields and near room temperature, the thermally polarized nuclear magnetization of systems such as ^{1}H in water is extremely weak (spin polarizations $\sim 10^{-8}$), requiring extensive signal averaging in order to obtain a resolvable NMR signal, and making imaging impractical with conventional methods [72,89,98]. With laser polarization, however, angular momentum is transferred from photons to nuclei, and a large nonequilibrium nuclear spin polarization ($> 10\%$) can be created in the spin-1/2 noble gases, ^{3}He and ^{129}Xe, independent of the applied magnetic field [90]. Laser polarized noble gas can be stored in specially prepared containers for several hours before the spin polarization decays back to thermal equilibrium. In "real world" samples such as biological tissue, air, and porous sandstone, the ^{3}He and ^{129}Xe spin polarization lifetime (T_1) is typically $\sim$10 s, still quite long for many purposes. Laser polarization greatly enhances the NMR detection sensitivity of the

noble gases [99], enabling diverse applications such as gas-phase imaging at high magnetic fields (e.g., of the lung) [18, 91–96], dissolved-state biomedical investigations [20, 100–103], chemical physics and materials science studies [17, 24, 104, 105], precision frequency measurements [14, 15, 106], and, as reported in this paper, practical MRI at low magnetic fields [107].

As a demonstration of low-field noble gas MRI, we imaged glass and plastic cells ("phantoms") containing laser polarized ^{3}He gas and thermally polarized water, at both high (4.7 T) and low (21 G) magnetic fields. Laser polarization of ^{3}He was accomplished with a standard spin-exchange optical pumping technique that employs Rb vapor as an intermediary to transfer angular momentum from laser photons to ^{3}He nuclear spins [90]. The ^{3}He glass cells were held in a static magnetic field of $\sim$100 G, heated to $\sim$170 °C in a hot air oven, and illuminated by 15 W of 795 nm light ($\sim$3 nm FWHM) from a fiber-coupled laser diode array (Optopower, Inc.). After about 3 hours of laser polarization, the ^{3}He phantoms were cooled to room temperature, walked over to the MRI instrument (without a holding magnetic field), and then placed in an appropriately tuned rf coil at the center of the low- or high-field MRI magnet. All ^{3}He phantoms contained 2.7 atm of ^{3}He, 100 torr of nitrogen, and a small amount of Rb metal, and were imaged with a ^{3}He spin polarization of $\sim$10%.

MRI at 4.7 T was performed using a commercial GE Omega/CSI spectrometer/imager operating at 152 MHz for ^{3}He and 200 MHz for ^{1}H, while imaging at 21 G was performed with an inexpensive, homebuilt spectrometer/imager operating at 67 kHz for ^{3}He and 88 kHz for ^{1}H, and employing a simple, wire-wound solenoid electromagnet (see Fig. 4.1). (A detailed description of our low-field MRI system will be provided in a future paper. The solenoid design is described in [108].) All images were obtained without signal averaging using standard MRI techniques. For

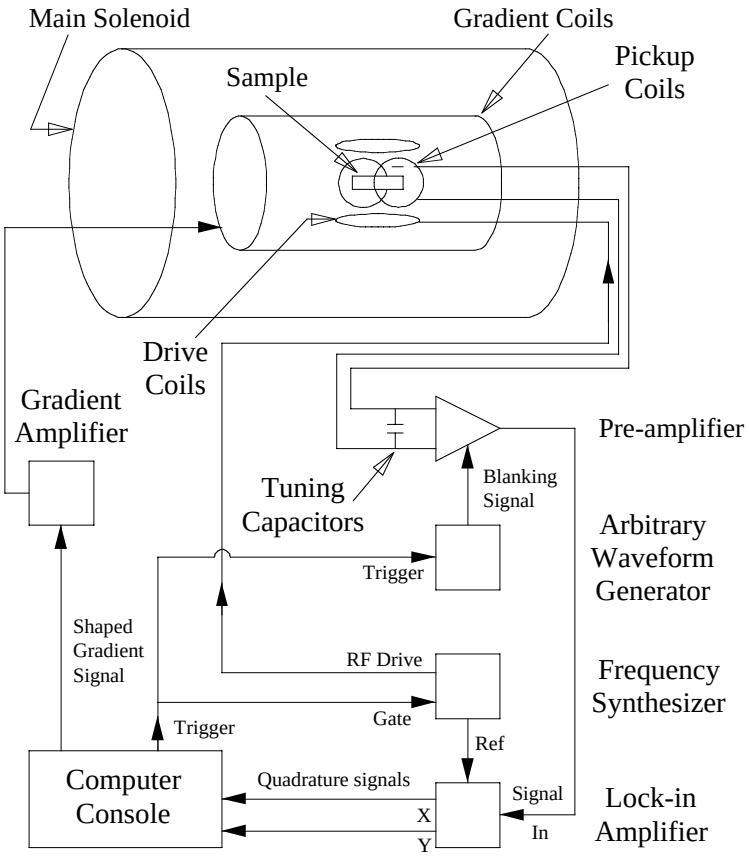

Figure 4.1: Schematic of the homebuilt low-field MRI system. The main magnetic field (B_z) of $\sim$20 G is created by an unshielded, copper wire solenoid. Gradient coils provide controllable, linear variations of B_z along the x, y, and z directions, which are necessary for imaging. Around the sample, coils tuned to the spins' Larmor frequency provide NMR excitation ("drive") and detect the resultant NMR signal ("pickup"). A frequency synthesizer operating close to the spins' Larmor frequency is gated by a millisecond TTL trigger to provide rf drive pulses. The pickup signal goes from a preamplifier - which is blanked during the drive pulse to avoid saturation - to a lock-in amplifier for phase-sensitive detection. A computer controls the magnetic field gradients and rf drive pulses, and performs data digitization and storage.

example, a spin echo pulse sequence was used for ^{1}H imaging of water phantoms at 4.7 T, and a low-flip-angle gradient echo technique (known as FLASH) was used for imaging the laser polarized ^{3}He gas phantoms [72]. (Low-flip-angle techniques are widely used for MRI of laser polarized noble gas because of the finite and difficult-to-replenish sample magnetization [18, 91–96].) The low-field imaging employed magnetic field gradients up to 0.2 G/cm, chosen to keep field variations across the sample small relative to the main field of ∼20 G, and hence to validate the secular approximation used to generate undistorted images from MRI data [109, 110].

As shown in Fig. 4.2, low-field ^{3}He images have comparable spatial resolution to high-field images of water and ^{3}He. Not surprisingly, low-field water images could not be obtained due to the very small ^{1}H spin polarization at 21 G. Our prototype low-field MRI system provides ^{3}He images with a good, two-dimensional resolution of ∼1 mm^2 for a data acquisition time of 10 s and a sample or slice thickness of ∼1 cm. For example, the H-shaped ^{3}He image shown in Fig. 4.2d has a two dimensional resolution of 0.6 × 1.5 mm and a sample thickness of 21 mm. In contrast, using naive scaling laws, approximately *two months* of signal averaging would be needed to make an ^{1}H water image of comparable resolution at 21 G using our low-field MRI system.

We found that the signal-to-noise ratio of low-field, laser polarized noble gas MRI was sufficient that the limit to imaging resolution was set by gas diffusion [72]. Diffusion coefficients for gases are ∼10^4 times larger than for liquids [111]. Therefore, significant gas atom displacement can occur during the application of the small imaging gradients that are appropriate for low-field MRI, limiting the image resolution [109, 110]. For example, with a gradient echo imaging method, an imaging gradient of ∼0.1 G/cm sets a diffusion-limited imaging resolution of ∼1 mm for free ^{3}He gas at standard temperature and pressure (STP) [72]. Note that this

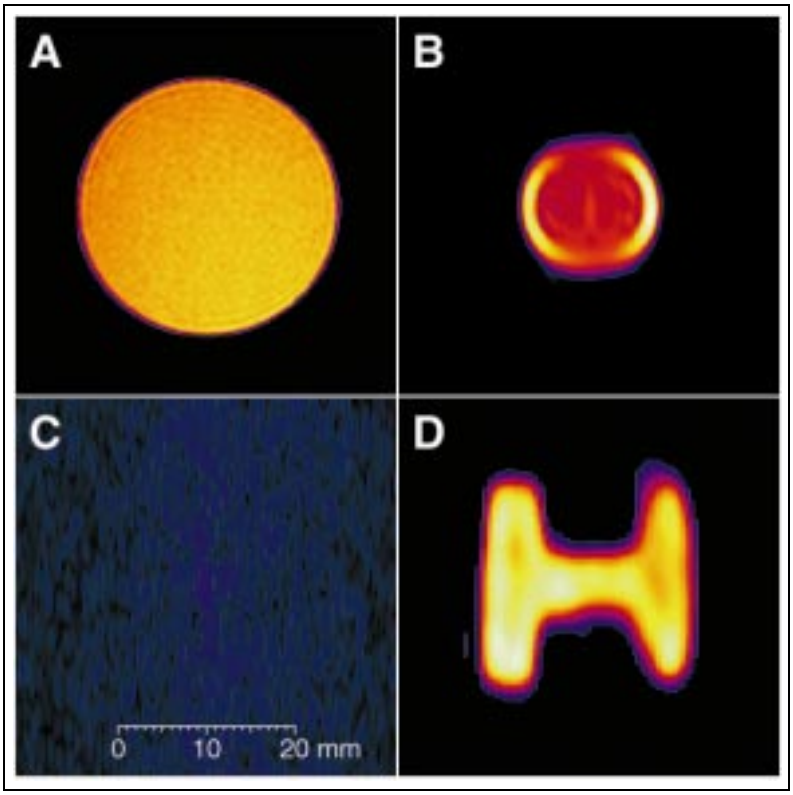

Figure 4.2: Comparison of NMR images taken at 4.7 T and 21 G. Images at 4.7 T were obtained using a GE Omega/CSI spectrometer/imager: (a) Water inside a cylindrical Plexiglas cell; and (b) laser polarized ^{3}He gas inside a cylindrical glass cell (the increased signal intensity near the edges is due to restricted gas diffusion near the cell walls, i.e., edge enhancement [107]). Comparison images at 21 G were obtained using the homebuilt spectrometer/imager (see schematic in Fig. 4.1). (c) No image of water inside a cylindrical glass cell because of the very low ^{1}H spin polarization, but (d) a clear image of laser polarized ^{3}He gas inside a handblown, roughly H-shaped glass cell. All four images are to the same scale, as given in (b). The width and height of the gas space within the glass H cell are each 22 mm, and the thickness is 21 mm. The 21 G images were acquired in $\sim$10 s using standard gradient echo imaging sequences.

imaging resolution can be improved by reducing the effective noble gas diffusion coefficient: e.g., in restricted environments (the lung, granular media, etc.), or in the presence of a buffer gas with a large scattering cross section.

An endemic problem in high-field MRI is spatial variations in magnetic susceptibility, for example, at the solid-gas or liquid-gas interfaces in granular media, foams, or the lung. Such susceptibility variations create local magnetic field gradients that induce both spatially homogeneous and inhomogeneous NMR line broadening at high magnetic fields: the homogeneous broadening reduces imaging resolution while the inhomogeneous broadening causes image distortion. Operating at low magnetic field greatly reduces these effects because the magnitude of susceptibility-induced local field gradients is proportional to the applied field. For example, we measured the NMR linewidth of laser polarized ^{3}He gas imbibed into rat lungs to be less than 3 Hz at 21 G, whereas recent measurements at high magnetic fields found much broader NMR linewidths ($\sim$100 Hz for ^{3}He gas imbibed into guinea pig lungs at 2 T and human lungs at 1.5 T [112, 113]). The nonlinear nature of susceptibility-induced distortion is evident in the high-field water images shown in Figs. 4.3a and 4.3b, while the reduced susceptibility distortion of low-field noble gas MRI is clearly demonstrated in Figs. 4.3c and 4.3d. Similar susceptibility-induced problems also limit NMR diffusion measurements at high magnetic fields, where background gradients in heterogeneous samples can make experiments difficult or impossible [77]. Again, such problems should be greatly ameliorated with low-field noble gas operation, providing a practical technique for measuring fluid permeability in porous media.

Low-field noble gas MRI can also examine voids inside electrically conducting materials. At the lower NMR frequencies enabled by low-field operation, RF electromagnetic fields can penetrate much deeper into conducting materials. Figure 4.4

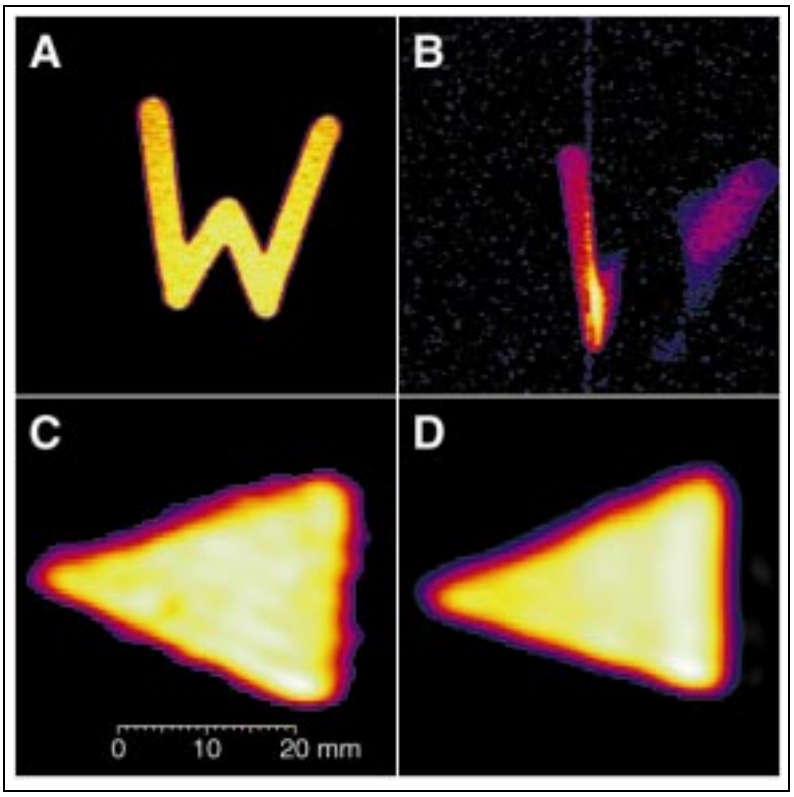

Figure 4.3: Reduced magnetic susceptibility distortion at low magnetic fields. At 4.7 T, an NMR image of a water sample in a machined, W-shaped Plexiglas cell is (a) undistorted when no high magnetic susceptibility materials are nearby, but is (b) severely distorted by susceptibility-induced magnetic field gradients when placed next to four sealed tubes of paramagnetic materials (gadolinium chloride, nickel chloride, magnesium chloride, and gadopentetate dimeglumine). However, at 21 G an NMR image of laser polarized ^{3}He gas in a handblown, roughly triangular glass cell is undistorted both (c) without nearby paramagnetic materials and (d) when placed next to the same four tubes of paramagnetic materials that distorted the high-field water image in (b). The gas space within the triangular cell has a base length of 23.5 mm, equal side lengths of 34 mm, and a thickness of 23 mm.

demonstrates the ability of low-field noble gas MRI to image gas spaces within conductively shielded objects. This new technique may be useful in studies of fissures or cavities inside metals, for example, in aerospace components, or in measuring wall thinning of pipes in steam generation plants and elsewhere. Together, the efficacy of low-field noble gas MRI for both paramagnetic and metallic materials should allow imaging of interstitial spaces in a wide variety of granular media, and thus provide a powerful probe of three dimensional granular structure, dynamics, and relative grain-gas flow.

In summary, low-field noble gas MRI is a powerful diagnostic technique with novel applications in physical and biomedical science. We developed a simple low-field apparatus that provides laser polarized ^{3}He gas images at 21 G in a few seconds, with a two dimensional spatial resolution of $\sim$1 mm^2 for a sample or slice thickness of $\sim$1 cm, comparable to the resolution at high magnetic fields provided by commercial MRI instruments.

We gratefully acknowledge J. Moore for preparation of excised rat lungs. This work was supported by NSF Grant No. BES-9612237, NASA Grants No. NAGW-5025 and No. NAG5-4920, the Whitaker Foundation, and the Smithsonian Institution.

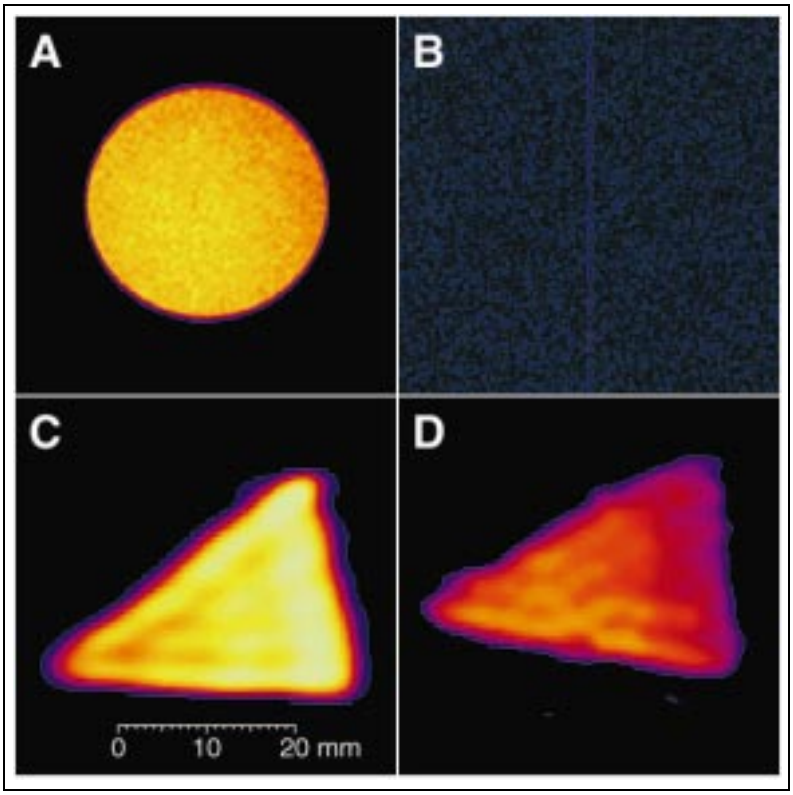

Figure 4.4: Imaging of voids within a conductor. Samples of water and laser polarized ^{3}He gas were encased in identical rf shields made of 25 mm thick brass. The rf shield reduced the water NMR signal by 3 orders of magnitude at 4.7 T, but reduced the ^{3}He signal minimally at 21 G. This modest low-field signal reduction is consistent with reduced Faraday (i.e., rf) shielding of the NMR excitation pulses and signals at low magnetic fields. NMR imaging was performed at 4.7 T of (a) a cylindrical water sample, and (b) the same sample encased in the brass shield, illustrating the impracticality of imaging spaces within an electrical conductor at high magnetic fields. Comparison images were obtained successfully at 21 G of (c) laser polarized ^{3}He gas in a handblown, roughly triangular glass cell (the same cell as in Fig. 4.3), and (d) the triangular cell encased in the brass shield, demonstrating the utility of low-field noble gas MRI for imaging voids within conductively shielded objects.

4.2 A System for Low Field Imaging of Laser-Polarized Noble Gas

G. P. Wong, C. H. Tseng, V. R. Pomeroy, R. W. Mair, D. P. Hinton, D. Hoffmann, R. E. Stoner, F. W. Hersman, D. G. Cory, and R. L. Walsworth

Journal of Magnetic Resonance, *vol.* ***141****, pp. 217-227 (1999).*

This article has been reformatted to conform to Harvard dissertation guidelines and is reprinted with permission.

We describe a device for performing MRI with laser-polarized noble gas at low magnetic fields (<50 G). The system is robust, portable, inexpensive, and provides gas-phase imaging resolution comparable to that of high field clinical instruments. At 20.6 G, we have imaged laser-polarized ^{3}He (Larmor frequency of 67 kHz) in both sealed glass cells and excised rat lungs, using ∼0.1 G/cm gradients to achieve ∼1 mm^2 resolution. In addition, we measured ^{3}He $T_2{}^*$ times greater than 100 ms in excised rat lungs, which is roughly 20 times longer than typical values observed at high (∼2 T) fields. We include a discussion of the practical considerations for working at low magnetic fields and conclude with evidence of radiation damping in this system.

Key Words: laser-polarized noble gas; low magnetic field; magnetic resonance imaging; lung imaging; radiation damping.

4.2.1 Introduction

Recently, laser-polarized (LP) spin-1/2 noble gases (^{3}He and ^{129}Xe) have been the focus of intense interest in the magnetic resonance community. Starting with LP ^{129}Xe gas imaging of excised mouse lungs in 1994 by Albert *et al.* [18], there have been numerous advances made with LP ^{129}Xe and ^{3}He imaging. Notable examples include live animal and human lung imaging [114], as well as imaging and time-dependent diffusion studies of materials [78, 104]. The interest in LP noble gases arises from the large nuclear spin polarization (>10%) provided by laser-polarization techniques [10,115]. Whereas the spin polarization of conventional, thermally polar-

ized systems is a linear function of the applied magnetic field, the spin polarization of LP noble gas is determined by factors that are not dependent on the applied magnetic field, such as laser power and gas mixtures. Consequently, it is possible to perform sensitive NMR and MRI on LP noble gases at substantially lower field strengths. For example, Darrasse *et al.* recently demonstrated LP ^{3}He human lung imaging at 1000 G (0.1 T) [116], while Saam and coworkers obtained one dimensional profiles of cells filled with LP ^{3}He at 31 G [117]. In addition, using superconducting quantum interference devices (SQUIDs), Augustine *et al.* imaged LP ^{3}He gas and ^{129}Xe solid at liquid helium temperature (4 K) and 5.4 G [118].

There are important advantages to low field MRI of LP noble gas because certain fundamental imaging constraints are diminished. In particular, distortions and line broadening that result from large background gradients produced by magnetic susceptibility differences in heterogeneous samples are greatly reduced. Also, low Larmor frequencies ($\sim$kHz) correspond to greater electromagnetic field skin depths. Consequently, RF pulses can penetrate thin metallic shielding and thus allow gas-phase imaging inside conductors. In addition, a low field system is simple, inexpensive, portable, and easy to maintain. Magnetic field requirements are easily met with a low-power, wire-wound solenoid capable of producing absolute field homogeneity comparable to, if not better than, typical high field clinical magnets. Also, the small external field and low (kHz) RF frequencies do not necessitate site restrictions, such as large shielded rooms, thus permitting operation in restricted environments (e.g., a space station) and with subjects and systems incompatible with high magnetic fields or high RF frequencies (e.g., patients with sensitive implants or experimental apparatus with integrated electronics).

Recently, we demonstrated fast, single-scan 2D imaging at 20.6 G of LP ^{3}He in sealed glass phantoms (for an example, see Fig.4.5) [119]. In this report, we describe

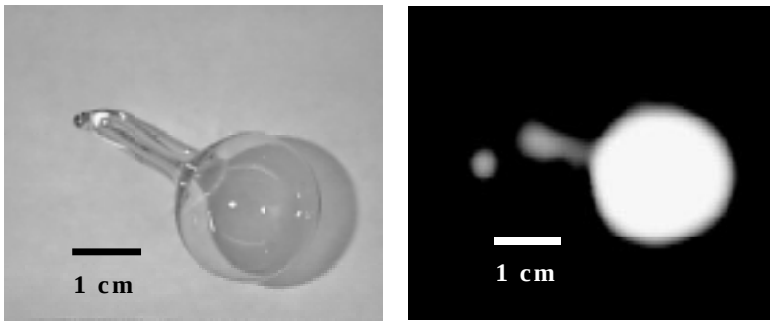

(a) (b)

Figure 4.5: Example ^{3}He test phantom and low field image. (a) Photograph of a sealed glass cell filled (at STP) with 2.7 atm ^{3}He, 100 Torr N_2, and Rb metal. Prior to filling, the cell was baked at high temperature under vacuum for 6 days; (b) Laser-polarized ^{3}He MRI of the test phantom at 20.6 G using a gradient echo FLASH sequence. Note that the small volume pull-off stem of the cell is visible to the left; the protrusion to the lower left of the pull-off is the zero-frequency artifact, and the discrepancy in the stem length is due to image foreshortening.

the low field imaging system used in those experiments, present recent experimental results (e.g., low field MRI of LP ^{3}He imbibed in excised rat lungs), and discuss advantages and practical considerations of imaging at low fields. We also present measurements of radiation damping in LP ^{3}He at low field and conclude with a discussion of this effect on our experiments.

4.2.2 System Overview

The Magnet

We built a wire-wound solenoid using a design by Hanson and Pipkin [108]. It is capable of producing a magnetic field of up to 100 G without significant resistive heating and consists of four layers of 19-gauge copper wire wrapped around a 114-cm long, 30-cm o.d. aluminum cylinder. Two HP6200B DC power supplies provide the current required to power the magnet – typically, 0.4 amps to each of the four

winding layers to establish an applied field of ∼20 G.

As Hanson and Pipkin showed, the magnetic field homogeneity in the central region of a solenoid can be characterized by the field along the axis (taken as the z direction) and its derivatives. This axial field $B_z(z,\, r = 0)$ is primarily determined by the solenoid dimensions, and given the solenoid radius a and the angle θ (which is defined by the symmetry axis and the line joining the solenoid center to the radius at the bore end), can be written as

$$B_z = \frac{4\pi NI}{10}\cos(\theta)\left[1 - \frac{3}{2}\sin^4(\theta)\left(\frac{z}{a}\right)^2 - \frac{5}{8}\sin^6(\theta)(7\cos^2(\theta) - 3)\left(\frac{z}{a}\right)^4 - \cdots\right]. \tag{4.1}$$

Here, I is the applied current and N is the number of turns per unit length. We also included second- and fourth-order correction coils wound on the outside of the main solenoid. The angle θ_2, defined by the dimensions of the second-order correction coil in analogy with θ is chosen so that the fourth-order term in Eq. 4.1 equals zero (i.e., $7\cos^2(\theta_2) - 3 = 0$). The fourth-order correction coil is a split solenoid and may be analyzed as two different solenoids with opposing currents and characteristic angles θ_4' and θ_4. The angles are chosen so that the second-order term in Eq. 4.1 goes to zero (i.e., $\cos(\theta_4')\sin^4(\theta_4') - \cos(\theta_4)\sin^4(\theta_4) = 0$). For convenience, we follow Hanson and Pipkins example and choose $\theta_4' = \theta_2$.

A simple coil loop of n turns with applied current I is used to shim the linear component of $B_z(z,\, 0)$; its field is described by

$$B_z^{(1)}(z, 0) = \frac{2\pi nI}{10}\frac{\sin^3(\theta)}{a}\left[1 + 3\cos(\theta)\sin(\theta)\left(\frac{z}{a}\right) + \frac{3}{2}\sin^2(\theta)(5\cos^2(\theta) - 1)\left(\frac{z}{a}\right)^2 + \cdots\right]. \tag{4.2}$$

This linear correction coil is offset so that the second order term of $B_z^{(1)}$ is zero at the center of the main solenoid (i.e., $5\cos^2(\theta_1) - 1 = 0$, where θ_1 is defined by the

position of the linear coil).

The magnet's field homogeneity was determined by measuring free induction decays (FIDs) of LP ^{3}He sealed in a spherical 8.5 cc test cell placed at the solenoid's center. At main fields of ∼20 G, typical linewidths of 2-3 Hz were observed, with even narrower linewidths (<1 Hz) under ideal conditions. Such ^{3}He linewidths were suitable for the imaging experiments performed; higher homogeneity would require magnetic shielding from the background field of ∼1 G and shim coils to compensate for radial gradients of B_z (the existing coils correct for axial gradients only).

Figure 4.6 shows an example of the measured temporal stability of the field during the first 12 h after the magnet was turned on. There is an initial large drift in the field (∼0.1%) as the DC current supplies and detection electronics warm up. After about an hour, the field equilibrates, providing short-term stability (on minute time scales) of a few parts in 10^5; with imaging times less than 30 s, this stability is sufficient. Straightforward modifications such as shielding, active feed-back control of the solenoid current, and temperature control of the magnet would increase both the magnetic field stability and homogeneity.

Electronics

The RF source is an unamplified Wavetek DDS function generator Model 29. This device provides a frequency reference for a lockin amplifier (Stanford Research Systems, Inc., Model SR830), while its main output is gated by a TTL pulse (whose duration sets the RF pulse width) and drives a set of Helmholtz coils surrounding the sample. A pair of orthogonally mounted pickup coils around the sample sense the NMR signal, which is amplified and filtered by a low noise preamplifier (Stanford Research Systems, Inc., Model SR560). After this stage, the lock-in amplifier further amplifies and filters the NMR signal components near the reference frequency. The

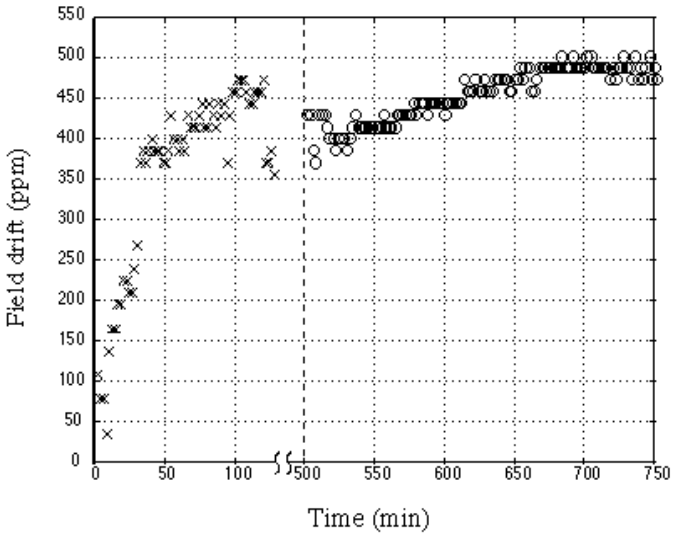

Figure 4.6: Typical temporal stability of solenoid's magnetic field (∼20 G) without stabilization. Two data sets are shown. The first (×) is taken just after turning on the magnet; the large initial drift is due to system warm up. The second data set (∘) is taken much later, after the current supplies and electronics have stabilized.

two drive coils surrounding the sample each consist of six turns of no. 25 HAPT wire wound around a square 7 cm per side. The drive coil pair are separated by 8.5 cm and tuned with external capacitors to the spin Larmor frequency (e.g., 67 kHz for ^{3}He at 20.6 G). The Q of this drive coil configuration is ∼10. The pickup coils are mounted orthogonal to the drive coils, and are wired to allow differential signal amplification that rejects common-mode noise (see Fig. 4.7a). Each pickup coil consists of ∼200 turns of no. 32 HAPT wire on a round nylon form 7.5 cm in diameter. The coils are spaced 4.5 cm apart and are tuned to the spin Larmor frequency by external capacitors; the measured Q is approximately 60. The sample holder is a 2.5 × 3.2 × 9 cm long trough nestled between the drive and pickup coils. The whole assembly (coils + sample holder) is rigidly mounted together with one of the drive coils on a hinged lid to allow access into the sample holder. This is shown in

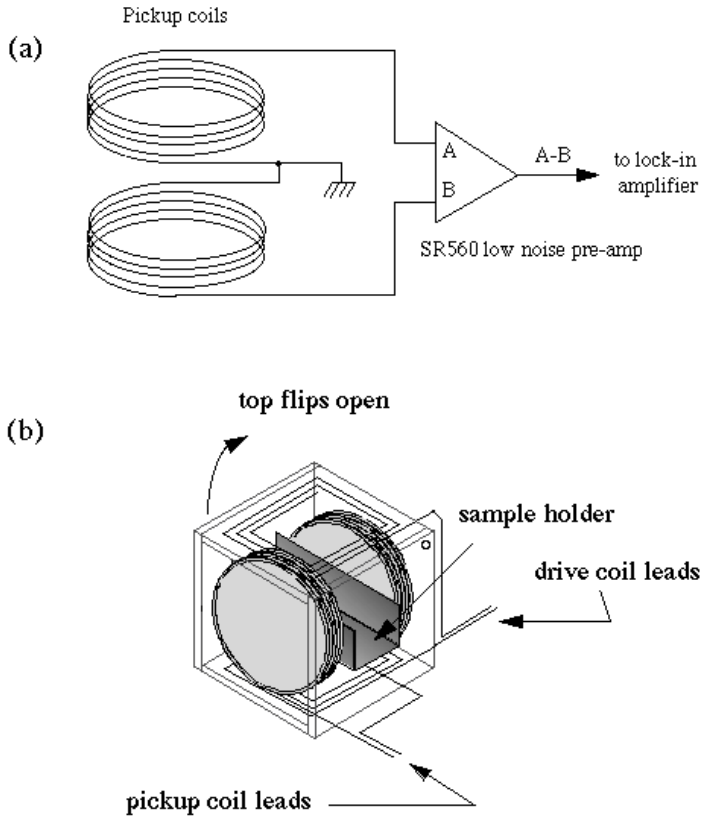

Figure 4.7: (a) Configuration used to reject common-mode noise in the pickup coils. (b) Sample holder with orthogonal RF drive (square) and pickup (round) coils. The coil geometry was inspired by our earlier maser and adiabatic fast passage (AFP) LP noble gas experiments (Ref. [14]).

Fig. 4.7b.

Imaging gradients are produced by a homemade set of unshielded Golay coils (for dB_z/dx and dB_z/dy, i.e., G_x and G_y) and a pair of anti-Helmholtz coils (for dB_z/dz, i.e., G_z) wound on a 14-cm diameter G-10 cylinder, following the description found in Callaghan [72]. With our present amplifiers, the anti-Helmholtz coils (also known as a Maxwell pair) provide a maximum gradient of 380 mG/cm, while the Golay coils produce up to 630 mG/cm. Typically, we used these gradients up to 50% of their full strength for durations of 10 ms. The gradients, as well as the RF trigger pulses,

are controlled by a commercial Bruker AMX console. Detected NMR signals are routed directly from the lock-in amplifier outputs into the console's digitizer (thus bypassing the console's normal high frequency receivers and mixers). Figure 4.8 shows a schematic of the system. One could easily replace the AMX console with a desktop computer equipped with a Digital-Analog Acquisition (DAQ) board. The DAQ board should have at least two analog outputs for gradient control, a TTL output to trigger and set the duration of the RF pulse, and a sufficiently fast digitizer ($\sim$50 kHz).

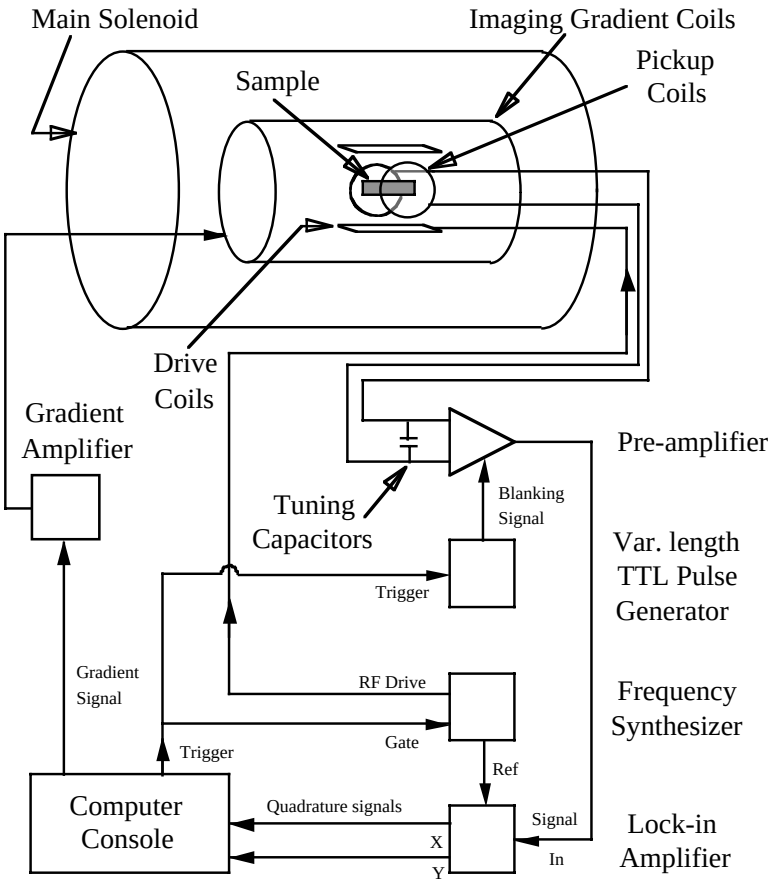

Figure 4.8: Schematic of low-field MRI system. A variable length TTL signal blanks the preamplifier slightly longer than the RF pulse to avoid amplifying any coil ring-down.

4.2.3 Method

A cell containing a mixture of 3 atm of ^{3}He, ∼100 Torr nitrogen and Rb metal was placed in a blown-air oven and heated to 180 ℃. Optical pumping of the Rb vapor by circularly polarized light from a 15 Watt fiber-coupled laser diode array (Opto Power Corporation, model OPCA-015-FCPS) polarized the ^{3}He via spin-exchange to approximately 10% after 3-4 h (in our small 8.5 cc sealed test cells). For the lung imaging experiments, a valved 65 cc cell was used; after laser-polarization, measured shots of 3 to 5 cc's of ^{3}He gas were forced into the excised rat lungs for imaging. Excised tissue was obtained from 300-400 g male Sprague–Dawley rats. Both the left and multiple right lobes of the lungs, along with several cm of trachea, were removed postmortem. A 25 gauge butterfly tube (with needle removed) was placed into the trachea and secured with silk suture. Forty-eight inches of high pressure plastic tubing extended down the bore of the low field magnet to connect the lung tissue to a syringe that was filled with LP ^{3}He gas directly from the valved glass polarization cell. Excised lungs were used in the imaging experiments within 3 h of harvest. All animal procedures were approved by the Massachusetts General Hospital Subcommittee on Research Animal Care.

4.2.4 Results

Pulse flip angles and T_1 of the LP gas were measured by recording the FIDs following each of a series of low flip angle (α) pulses. Given a time T_R between each pulse, the jth FID signal amplitude S_j can be expressed as

$$S_j = S_0(\cos\alpha)^{j-1}\exp\left[-(j-1)\times T_R/T_1\right]. \tag{4.3}$$

Figure 4.9 shows typical FID and flip angle calibration data taken at 20.6 G for LP ^{3}He sealed in a glass cell. Each point of the flip angle calibration data represents the logarithm of the integrated real part of each successive FIDs fourier transform (which is proportional to $\log[S_j]$); plotting $\log[S_j]$ versus j should be linear with a slope equal to $[\ln(\cos\alpha) - T_R/T_1]$. With $T_R \ll T_1$, one can determine the flip angle α; consequently, once α is known, repeating the experiment with a long T_R allows one to measure T_1.

To demonstrate the efficacy of low field imaging with laser-polarized noble gases for samples of biological interest, we imaged excised rat lungs filled with LP ^{3}He (Fig. 4.10) using a FLASH imaging sequence: 128 concentric phase encodes steps; 12° flip angle; gradient strength and duration was ∼0.1 G/cm, 10 ms; total imaging time was ∼25 s. No slice selection was used, and the two-dimensional resolution was ∼1 mm^2. In different experimental runs we measured ^{3}He relaxation times T_1 from 16 to 63 s (Fig. 4.11), which is within the range of values reported at high field due to remnant paramagnetic oxygen in the lung gas space [93]. We also measured the low-field ^{3}He $T_2{}^*$ in excised rat lungs to be greater than 100 ms, which is significantly longer than the approximately 5 ms $T_2{}^*$ observed for LP ^{3}He in guinea pig and human lungs at 2 and 1.5 T, respectively [114, 120]. This longer ^{3}He $T_2{}^*$ is a result of the reduced effect of magnetic susceptibility heterogeneity at low magnetic fields, and is one of the advantages of low-field imaging. In addition, there was a consistent trend of increasing $T_2{}^*$ with subsequent low angle RF pulses (corresponding to decreasing longitudinal LP ^{3}He magnetization), which prompted us to investigate radiation damping in this system. A brief discussion of these measurements is given later in this paper.

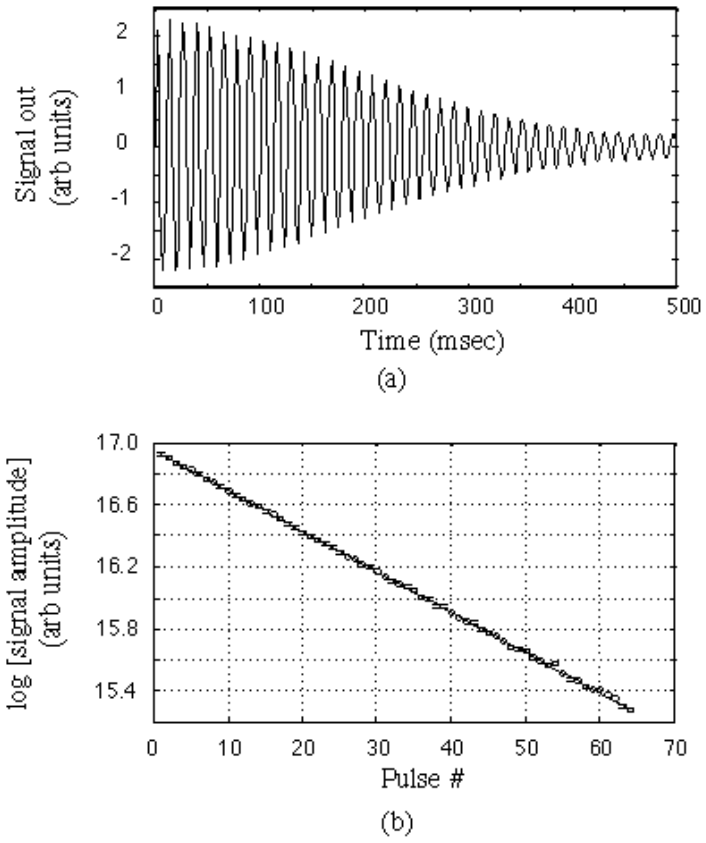

Figure 4.9: (a) Typical free-induction decay (FID) observed for LP ^{3}He at 20.6 G and (b) flip angle calibration data obtained using a series of low flip angle pulses on a LP ^{3}He sealed glass phantom; the line shown is a fit to the data. RF pulse width was 2 ms, and the frequency synthesizer was set to output 2.0 Vpp at 67.0 kHz. For each FID acquired for (b) (of which (a) was the first), the linewidth was $\sim$2 Hz with initial SNR $\sim$1700. Acquisition of 64 FIDs took $\sim$84 s, which was much less than the T_1($\sim$100 h) of the cell. Fitting the data to the log of Eq. 4.3 indicated a flip angle α of 13.0° for this RF pulse.

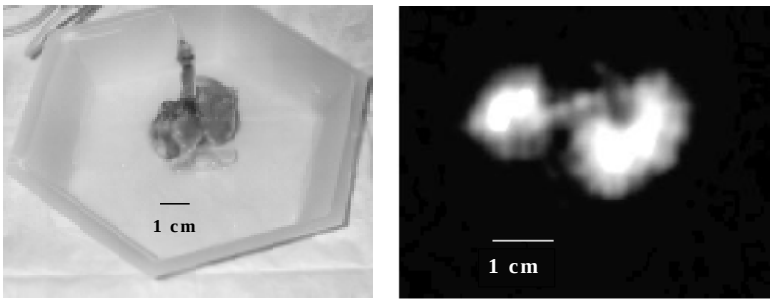

(a) (b)

Figure 4.10: Low field LP ^{3}He images of excised rat lungs. Excised rat lungs (a) were filled with LP ^{3}He gas and (b) imaged at 20.6 G.

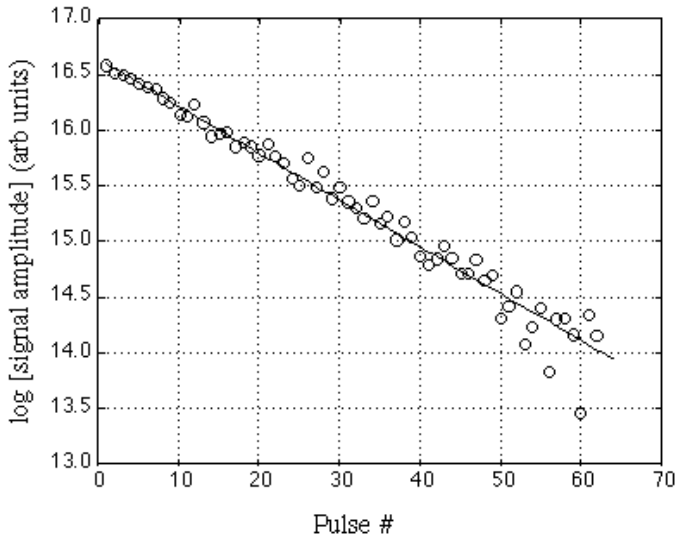

Figure 4.11: Example T_1 data for LP ^{3}He inside excised rat lungs at 20.6 G. With the calibrated flip angle of 9.5° and T_R of 540 ms, the data shows a T_1 of 19 s for LP ^{3}He inside the lungs.

4.2.5 Discussion

(i) Dependence of Signal-to-Noise-Ratio on Magnetic Field Strength

In conventional NMR and MRI, nuclear spin polarization P is determined by the temperature T and magnetic field strength B according to the Boltzmann (thermal) distribution,

$$P = \frac{1 - \exp(-\mu B/kT)}{1 + \exp(-\mu B/kT)} \sim \mu B/2kT \tag{4.4}$$

where k is the Boltzmann constant, and μ is the nuclear magnetic moment. For example, assuming T at room temperature ($\sim$296 K) and a field strength of 1.5 T, the proton spin polarization is $\approx 0.0005\%$. This value can be improved by increasing the magnetic field or lowering the temperature. However, given the large quantity of available protons found in most samples of biological interest (usually in the form of H_2O), NMR signal intensity is usually adequate at magnetic fields of $\sim$1 T despite the low polarization. This is in contrast to the laser-polarization of noble gases (i.e., ^{129}Xe and ^{3}He), where polarizations of order $\sim$1-50% can be achieved independent of magnetic field strength. This factor of 10^4 to 10^5 increase in polarization is balanced by the 1/3000 ratio of gas to liquid density [at standard temperature and pressure (STP)] and the lower gyromagnetic ratio of the spin-$\frac{1}{2}$ noble gases compared to that of ^{1}H [$\gamma(^3He) : \gamma(^1H) = 0.76; \gamma(^{129}Xe) : \gamma(^1H) = 0.28$]. Thus in high magnetic fields, one can expect comparable magnetization density, and hence NMR signals per unit volume, from protons (in liquid) and LP noble gases. At low fields (e.g., 20.6 G) LP noble gas imaging is still feasible, whereas proton imaging is impractical unless a large "prepolarizing" field is used to enhance the extremely low proton spin polarization (see Table 4.1).

A more quantitative discussion should begin with signal-to-noise considerations. By approximating the ensemble of polarized nuclear spins as a driven solenoid cou-

	^{1}H (water)	^{3}He	^{129}Xe
Spin densities at STP (assuming pure samples)	6.7×10^{22} (^{1}H nuclei/cc)	2.7×10^{19} (^{3}He nuclei/cc)	2.7×10^{19} (^{129}Xe nuclei/cc)
Gyromagnetic ratio γ (10^8 rad/s/T)	2.67	2.04	0.74
High Field ($B_0 = 1.5$ T)			
Larmor frequency	63.8 MHz	48.6 MHz	17.6 MHz
polarization	5.1×10^{-6}	$(1-5) \times 10^{-1}$	$(1-10) \times 10^{-2}$
magnetization density ($10^{18}\mu_N$/cc)	**0.96**	**5.7–29**	**0.2–2.1**
Low Field ($B_0 = 0.002$ T)			
frequency	87.9 kHz	67.0 kHz	24.5 kHz
polarization	7×10^{-9}	$(1-5) \times 10^{-1}$	$(1-10) \times 10^{-2}$
magnetization density ($10^{18}\mu_N$/cc)	**0.0013**	**5.7–29**	**0.2–2.1**

Table 4.1: Comparison of thermally polarized water and laser-polarized ^{3}He and ^{129}Xe magnetizations at high and low fields.

pled to the pickup (or receiver) coils, Hoult and Richards deduce an expression for the detected NMR signal ξ_S [121]:

$$\xi_S = (B_r/i_r)V_S\omega_0 M_0. \tag{4.5}$$

Here, (B_r/i_r) is the magnetic field strength per unit current that the pickup coil can produce, V_S is the sample volume, ω_0 is the Larmor frequency, and M_0 is the sample magnetization given by the product of the polarization P, density of spins N_S, and the magnetic moment $\mu/2$:

$$M_0 = PN_S\mu/2. \tag{4.6}$$

Combining Eqs. [4.5] and [4.6], and noting that $\omega_0 = \gamma B$, one finds

$$\xi_S = (B_r/i_r)V_S\gamma BPN_S\mu/2. \tag{4.7}$$

The dominant noise source for sufficiently small samples at high field, and practically

any sample at low field, is Johnson noise from the pickup coils at temperature T

$$\xi_N = (4kTR\Delta f)^{1/2}, \tag{4.8}$$

where R is the coil resistance and Δf is the noise bandwidth of the system. Inductively coupled noise from samples with weak electrical conductivity (e.g., biological tissue) scales linearly with the NMR frequency: $\xi_N \sim \omega \sim B$. This latter "tissue noise" dominates over coil Johnson noise only in large biological samples at high fields. [Note: due to the RF skin depth of the coil, there is also a weak dependence on NMR frequency, and hence magnetic field: $\xi_N \sim \omega^{1/4} \sim B^{1/4}$. For simplicity of discussion, we will ignore this weak effect here.]

Dividing Eq. [4.7] by Eq. [4.8], one obtains the familiar expression for the NMR signal-to-noise-ratio (SNR):

$$\text{SNR} = \frac{(B_r/i_r)V_S\gamma BPN_S\mu/2}{\sqrt{4kTR\Delta f}}. \tag{4.9}$$

Note that P in the equations above is linearly dependent on the applied magnetic field for thermally polarized samples: i.e., SNR $\sim B^2$. As mentioned earlier, a prepolarizing field B_P is sometimes applied that is purposefully stronger than the magnetic field B in which the nuclei precess [122, 123]; in such cases, SNR is proportional to $B_P \times B$. In contrast, P is field independent for laser-polarized noble gases and hence SNR depends only linearly on B.

Assuming similar coil characteristics for detecting both thermally and laser-polarized samples, the ratio of SNRs scale as

$$\text{SNR}(LP)/\text{SNR}(\textit{thermal}) \propto 1/B_P. \tag{4.10}$$

Equation [4.10] gives the expected SNR from laser-polarized noble gases when compared with a thermally polarized sample at *the same field*. Furthermore, this equation can be directly applied at varying field strengths, which is not necessarily true of a comparison of SNR at high and low fields for LP or thermally polarized samples alone. In this latter case, establishing a clear field dependence is complicated by the fact that coil characteristics (i.e., B_r/i_r in Eq. [4.9]) can be quite varied in design and behavior over large frequency ranges. For instance, at low frequencies (kHz) one can utilize multiple turn coils to enhance signal detection, a technique not easily parameterized by the main applied field.

As an example, we compare $1/B_P$ at 1.5 T (a typical clinical imager field strength) and 20 G. If we assume SNR($LP\ gas$) $\sim 10 \times$ SNR($water$) at high field, then at the lower field we expect SNR($LP\ gas$) $\sim 750 \times 10 \times$ SNR($water$). Thus the low field SNR of a LP noble gas sample exceeds the low field SNR of a thermally polarized water sample by nearly four orders of magnitude.

(ii) Reduced Effect of Magnetic Susceptibility Gradients at Low Fields

As noted above, one of the advantages of low field imaging is to reduce both imaging distortions and line broadening due to heterogeneous magnetic susceptibilities. Assuming that a given susceptibility χ is linear, we have the simple expression for the resultant magnetic field B'

$$B' = B_0(1 + \chi), \tag{4.11}$$

where B_0 is the main applied field. When χ is nonuniform in a sample ($B' = B'(r)$), spins will precess at a frequency $\gamma(B'(\mathbf{r}) = \mathbf{G} \cdot \mathbf{r})$ in the presence of an imaging gradient $\mathbf{G}$. Thus the usual mapping of spin frequencies (with gradients on) to real

space is no longer an accurate representation of the spatial distribution of spins, and will result in imaging distortions. Two possibilities to reduce or eliminate such artifacts is to either increase the imaging gradient strengths to a degree which makes the susceptibility-induced frequency shifts much smaller than the imaging gradient (i.e., $\mathbf{G} \cdot \mathbf{r} \gg$ variations in $B'(\mathbf{r})$), or to produce the same effect by decreasing the main field B_0. In our low field setup we use gradients 1/10 the strength of high field (clinical) imaging gradients, but the drop of nearly three orders of magnitude in the main field B_0 implies a hundred-fold improvement in reducing artifacts arising from susceptibility heterogeneity. In addition to distortions, variations in χ lead to spectral line broadening. For example, let χ be characterized by a Gaussian spatial distribution with mean χ_0 and standard deviation $\Delta\chi$. The susceptibility deviation $\Delta\chi$ causes decoherence for *stationary* nuclei precessing in the resultant varying fields. This decoherence is characterized as a contribution to ${T_2}^*$ of the form

$$1/T_2^* = 1/T_2 + \gamma \Delta\chi B_0/2. \tag{4.12}$$

For diffusing nuclei (with diffusion coefficient D), one must consider a random walk of the ensemble's phase, providing an additional contribution to T_2^*

$$1/T_{2diff}^* = \left[\gamma(\Delta\chi/l)B_0\right]^2 D\tau^2/3, \tag{4.13}$$

where l is a characteristic length over which χ varies by $\Delta\chi$, and τ is related to the echo time used in the imaging sequence. Strictly speaking, this expression is relevant for diffusion through a steady gradient field. In practice, susceptibility-induced gradients can fluctuate, with an upper bound on phase shifts they induce. The result is a "restricted random walk" that can only be described by Eq. [4.13] in

a "slow diffusion" regime where the characteristic diffusion time is large compared to the frequency shifts due to susceptibility heterogeneity, i.e., $(\gamma\Delta\chi B_0)(l^2/D) \gg 1$. In a "fast diffusion" regime, $(\gamma\Delta\chi B_0)(l^2/D) \ll 1$ and Eq. [4.13] is no longer valid; instead, the correct expression is of the form

$$1/T^*_{2diff} = (\gamma\Delta\chi B_0)^2(l^2/D). \tag{4.14}$$

Both Eqs. [4.13] and [4.14] depend on the main field B_0 squared, unlike Eq. [4.12] which is linear in B_0.

Clearly, at low fields there will be significantly less decoherence due to magnetic susceptibility gradients than at high fields, in addition to the reduction in imaging distortions. This has been demonstrated experimentally in a previous report [119] and will be particularly effective for low field noble gas NMR in heterogeneous samples such as the lung or reservoir rocks [124].

(iii) Imaging Resolution Considerations

An immediate benefit of the reduced magnetic susceptibility at low fields is the long T_2^* for heterogeneous samples. As mentioned earlier, T_2^* was measured to be greater than 100 ms for LP ^{3}He at STP when infused into a sample of excised rat lungs at 20.6 G; however, this value does not fully demonstrate the aforementioned B_0^2 improvement over high field because of both B_0 inhomogeneity and uncertainties due to the influence of radiation damping (discussed below). Thus one can expect even longer LP ^{3}He T_2^* at low fields with better magnetic field shimming and reduced radiation damping. The positive effect of a longer T_2^* on imaging resolution (Δx)

can be seen in the expression from Callaghan [72]

$$\begin{aligned} \Delta x(T_2^* - \textit{limited}) &= [(\gamma G/(2\pi)) \times \pi T_2^*]^{-1} \\ &= 2/(\gamma G T_2^*), \end{aligned} \tag{4.15}$$

where γ is the gyromagnetic ratio in angular units and G is the applied gradient strength. Weak gradients are used at low fields to keep field variations across the sample small relative to the main magnetic field, and hence to validate the secular approximation used to generate undistorted images from MRI data [109,110]. Typically, 0.1 G/cm gradients were used in our low field setup. At high fields, gradients for human subjects are limited to $\sim$1 G/cm by safety considerations. Assuming T_2^* is 100 and 5 ms at low and high fields, respectively, one obtains a corresponding $\Delta x(T_2^* - \textit{limited}) = 0.1$ and 0.2 mm for LP ^{3}He. It is important to note that the high and low field T_2^* values used in this estimate were measured in "bulk" LP ^{3}He imbibed in the lungs; locally, T_2^* may differ in a given voxel. Nonetheless, assuming that these times are reasonable for an average voxel, the calculated values serve as a basis of comparison for low and high field noble gas MRI, and will be referred to as Δx_{opt}.

Next, consider the image resolution set by finite data acquisition time. At low fields we typically acquire NMR imaging data for 128 ms, corresponding to a frequency resolution of 1/(128 ms) = 7.8 Hz. For comparison, assume that we use the same acquisition time at high field and employ the same imaging gradient values as above (respectively). This frequency resolution then translates to an image resolution of 0.2 mm at low field, and 0.02 mm at high field. Clearly, given the quoted values for T_2^*, one could use a longer acquisition time at low fields, while a shorter acquisition time at high field would not degrade resolution.

The effect of diffusion for gases is quite significant. At STP, ^{3}He has a diffusion coefficient $D = 1.8 \times 10^{-4}$ m^2/s. A simple calculation gives the one-dimensional distance an ^{3}He atom will diffuse in a data acquisition time t_{aq} of 128 ms

$$\Delta x_{diff} = (2Dt_{aq})^{1/2} = 6.8 \text{ mm}. \tag{4.16}$$

As Callaghan notes [72], one should not consider Δx_{diff} as a strict limit on resolution; rather, it results in spectral broadening that, in the presence of imaging gradients, will degrade resolution in a manner weighted toward the T_2^*-limited value. Therefore, ignoring the small effects of a finite data acquisition time, we find the effective image resolution of LP ^{3}He gas in the lung at STP to be

$$\begin{aligned} \Delta x &= 1.34[\Delta x_{diff} \Delta x_{opt}^2]^{1/3} \\ &= 0.6 \text{ mm for low fields} \\ &= 0.9 \text{ mm for high fields} \end{aligned} \tag{4.17}$$

$$\tag{4.18}$$

This analysis shows that low and high field MRI of laser-polarized gas offer comparable resolution for human lung imaging (of course, sufficient NMR SNR is required to realize such resolution – see discussion above). The relatively weak gradients used at low fields are compensated by the intrinsically longer T_2^*. However, because of the high degree of diffusion, gas phase imaging at both high and low fields only allows for resolution just under 1 mm. For nonliving subjects, this resolution can be improved in principal by increasing the gas pressure; and, at high fields, by increasing the strength of the imaging gradients.

(iv) Reduced RF Shielding at Low Frequencies

Another advantage for low field imaging is that oscillating electromagnetic fields can penetrate much deeper into conducting materials at the low Larmor frequencies resulting from the reduction in field strength. The "skin depth" δ that characterizes the distance RF can propagate inside a conductor before it is attenuated by 63% $(1/e)$ is given by [125]

$$\delta = \frac{1}{\sqrt{\pi f \sigma \mu}}, \tag{4.19}$$

where f is the Larmor frequency, σ is the conductivity of the conductor, and μ is the magnetic susceptibility of the conductor. For example, at 100 kHz, δ is 400 μm for brass and 200 μm for copper. On the other hand, δ is 13 μm and 7 μm for brass and copper, respectively, at 100 MHz. Thus the imaging of spaces surrounded by conductive materials, which is not feasible with high field NMR, may be achieved with low field MRI of LP noble gas. This capability has also been demonstrated in the previous report [119].

(v) Radiation Damping

Radiation damping in NMR is well known [70,126] and is generally observed at high fields where liquid-phase magnetization due to thermal polarization is large, T_2^* is long, and pickup coil Q is very high. Briefly stated, radiation damping describes the effect of the "back reaction" field of the pickup coil on the sample magnetization. The precessing spins cause a current to flow in the pickup coil, which in turn produces a field that acts on the sample magnetization and brings it back into the longitudinal direction in the lower energy configuration (i.e., aligned with the main magnetic

field). The characteristic time for this process is τ_{rd}

$$\tau_{rd} = (2\pi\eta\gamma Q|\mathbf{M}|)^{-1} \tag{4.20}$$

where η is the filling factor, and $\mathbf{M}$ is the magnetization vector. For LP gases, radiation damping is in stark contrast to T_1 and T_2^* processes, which act to reduce the magnitude of $\mathbf{M}$ (recall that T_1 relaxation restores the magnetization to thermal equilibrium, which is much smaller than the magnetization achieved with laser-polarization). In comparison, radiation damping does not affect the magnitude of $\mathbf{M}$, but its direction. Because radiation damping is observed for large magnetizations, it is not surprising that we observed this effect at low fields in our LP ^{3}He samples. In fact, optically pumped ^{3}He Zeeman masers rely on radiation damping to sustain an active oscillation, as was first demonstrated at 32 G [127]. A related device we have developed is a cohabitating, two-species ^{3}He/^{129}Xe Zeeman maser operating at fields $\sim$1–3 G [14].

Due to long T_1 and nonrenewable polarization of the LP noble gases, one generally utilizes small flip angles to acquire NMR imaging data. If the flip angle α is held constant, the longitudinal LP noble gas magnetization $\mathbf{M}$ is depleted each pulse by a factor of $(1 - \cos\alpha)$ and by T_1 relaxation between pulses. Radiation damping acts to restore $\mathbf{M}$ back along the $\mathbf{B_z}$ axis, resulting in an effectively smaller flip angle α in the case where the interpulse spacing T_R is much less than T_1 and the noble gas is laser-polarized in the lower energy state. This radiation damping effect is clearly seen in Fig. 4.12, which shows flip angle calibration data taken with the pickup coils tuned both on and off resonance with the ^{3}He Larmor frequency (i.e., with a high and low pickup coil Q, respectively). Recall that our drive coils are independent from and orthogonal to our pickup coils; thus we can be confident that

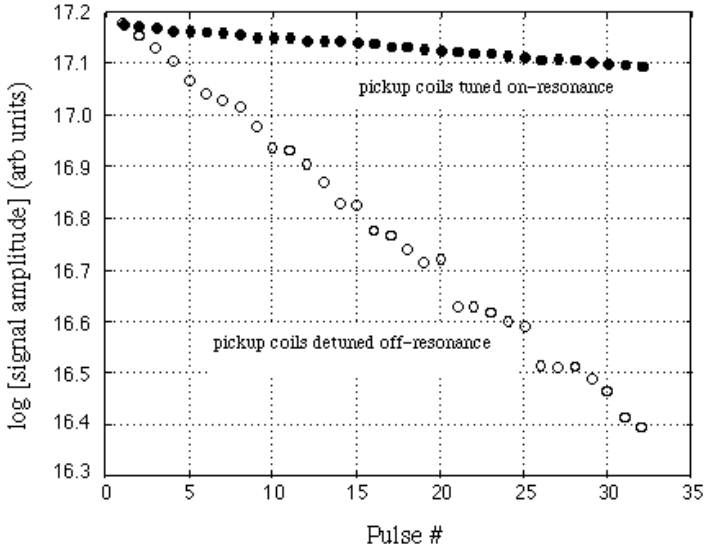

Figure 4.12: The effect of coil tuning on LP ^{3}He flip angle measurements at 20.6 G in a sealed glass cell, demonstrating radiation damping in our low-field system. The (•) data were taken with pickup coils tuned on resonance with the ^{3}He Larmor frequency (67 kHz). With exactly the same RF pulse power and duration, a dramatically increased flip angle (◦) was observed when the pickup coils are detuned far off-resonance (i.e., with a greatly reduced pickup coil Q). Fits to the (•) and (◦) data yield apparent flip angles of 4.2° and 12.8°, respectively.

the same RF power over the same duration is delivered to the sample regardless of the pickup coil tuning. However, by changing the pickup coil tuning, the "back reaction" field generated while $\mathbf{M}$ has a transverse component precessing around $\mathbf{B_z}$ is also changed. As expected, the detuned case minimizes the effect of radiation damping, and the effective flip angle is greater.

Another way to examine the situation is to vary the acquisition time between LP ^{3}He flip angle calibration data. The flip angle calibration sequence employs "crusher" gradients directly after each acquisition period to effectively remove any residual transverse magnetization. Consequently, one expects to see a larger effective flip angle when shorter acquisition times are chosen, because the crushers dephase

any residual transverse magnetization that radiation damping could have restored to the longitudinal direction. Figure 4.13 shows three data sets supporting this expectation, with acquisition times of 1024, 256, and 64 ms. There is a clear trend of larger effective flip angles for shorter acquisition times. Finally, Fig. 4.14 shows τ_{rd} measurements made from 64 successive FIDs from LP ^{3}He in excised rat lungs at 20.6 G. It is well known that FIDs follow a decay of the form $\mathrm{sech}(t/\tau_{rd})$ when radiation damping dominates over the usual T_2^* exponential decay (i.e., $\tau_{rd} \ll T_2^*$). From Eq. [4.20], τ_{rd} depends on $|\mathbf{M}|$, which is decreasing after each FID acquisition due to magnetization dephased by the subsequent crusher gradients. Since τ_{rd} is inversely proportional to $|\mathbf{M}|$, one expects τ_{rd} to increase with each successive FID, which is observed in the data. (Note: based on Fig. 4.14, which shows τ_{rd} increasing from 50 to 120 ms, one can assume that $T_2^* > 100$ ms for ^{3}He imbibed into excised rat lungs at 20.6 G, as we stated earlier. Values of T_2^* greater than 100 ms have also been measured with the coils detuned off resonance.)

While these results are unsurprising, they do raise the question of how to quantify parameters of interest for low field noble gas NMR. For example, T_1 data shown in Fig. 4.11 for a sample rat lung was taken with the pickup coils tuned on resonance. If the coils were tuned off resonance, both a larger apparent flip angle would have resulted, as well as a shorter apparent T_1. As for imaging, the previous discussion on resolution leads one to expect better resolution with decreasing magnetization (i.e., less radiation damping), since dephasing times will increase as $\mathbf{M}$ decreases. This is counterbalanced by the loss of SNR as $\mathbf{M}$ decreases, and the fact that radiation damping plays less of a role when imaging gradients are applied (this last effect enabled better than 1 mm^2 resolution in our low field LP ^{3}He imaging, despite large $\mathbf{M}$).

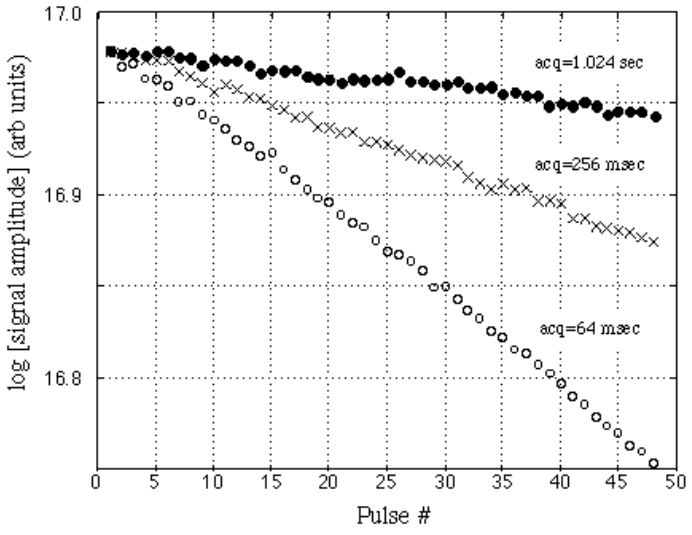

Figure 4.13: The effect of data acquisition time on LP ^{3}He flip angle measurements in a sealed glass cell, demonstrating the effect of radiation damping in our low-field system. All data were taken at 20.6 G with the pickup coils tuned on-resonance with the ^{3}He Larmor frequency (67 kHz), and with exactly the same power and duration RF pulse. The upper data (•) had an FID acquisition time (acq) of 1.024 s; the middle data (×) had acq = 256 ms; and the lower data (∘) had acq = 64 ms. Apparent flip angles are 2.4°, 3.9°, and 5.6°, respectively.

4.2.6 Conclusion

Low field imaging of laser-polarized noble gas offers many advantages while retaining the resolution one expects from a high field system. Setting up a low field apparatus is straight-forward and inexpensive, utilizing easy-to-manufacture equipment and off-the-shelf electronic components of modest cost. Furthermore, a low field MRI system is robust and portable and does not require specialized accommodations (e.g., a shielded room or cryogenic cooling for the magnet). Operating at low fields (<100 G) results in low Larmor frequencies (kHz), which reduces both RF power requirements and simplifies the electronics required. Also, these low frequen-

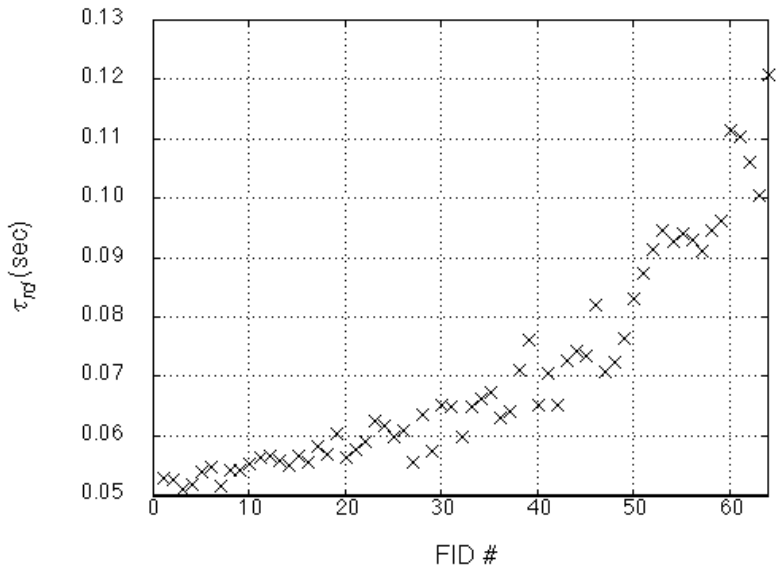

Figure 4.14: Measurements of radiation damping time (τ_{rd}) for LP ^{3}He inside excised rat lungs at 20.6 G are shown for each of the FIDs acquired from sequential low flip angle pulses. With each successive FID, the ^{3}He magnetization is reduced, hence radiation damping is lessened (i.e., τ_{rd} increased).

cies have longer RF skin depths, thus allowing gas-space imaging inside conductive materials. At low magnetic fields there is a reduced effect of magnetic susceptibility heterogeneity, resulting in longer T_2^* and improved noble gas image resolution and distortion reduction. This reduced susceptibility effect is also relevant to restricted gas diffusion experiments conducted in porous media, where sample heterogeneity limits the technique's effectiveness at high fields [78]. Finally, the long T_2^* at low fields and the high spin polarization in LP ^{3}He make radiation damping effects observable (e.g., during low flip angle calibrations), which must be taken into account when interpreting LP noble gas NMR data.

4.2.7 Acknowledgments

We gratefully acknowledge J. Moore for preparation of excised rat lungs. This work was supported by NSF Grant BES-9612237, NASA Grants NAGW-5025 and NAG5-4920, the Whitaker Foundation, and the Smithsonian Institution. G.P.W. gratefully acknowledges support from an NSF Graduate Research Fellowship.

Chapter 5

Persistence in 1-D diffusion

Nothing in the world can take the place of persistence.
Talent will not; nothing is more common than unsuccessful men with talent.
Genius will not; unrewarded it's almost a proverb.
Education will not; the world is filled with educated derelicts.

Persistence and determination alone are omnipotent.

- Calvin Coolidge

5.1 Introduction to Chapter 5

Recently, we used a novel NMR scheme to observe "persistence" in one dimensional (1-D) gas diffusion [128]. In this context, persistence is defined as the probability $p(t)$ that for an initially random distribution of spin magnetization, a given region will *not* change sign after some amount of time t. Calculations have shown that $p(t) \sim t^{-\theta}$, where the persistence exponent θ is dependent on both the dynamics and dimensionality of the system under study. For 1-D diffusion, we measured $\theta \sim 0.118 \pm 0.008$, in agreement with theoretical and numerical calculations that found $\theta \sim 0.12$ [129–131]. Persistence is an interesting phenomena in the general

class of first passage events in non-equilibrium dynamics, and has been the focus of statistical physicists in recent years [132–138]. Notably, our report [128] joins a small pool of experimental results [139–141], in contrast to the relatively larger body of analytical and numerical progress in persistence research. In particular, our persistence measurement is the first performed in a diffusing system and the first to examine a one-dimensional configuration.

In this chapter, we begin by presenting a reprint of our paper, *Measurement of persistence in 1-D diffusion* [128], which concisely describes both our experiment and results. In later sections, we discuss in more detail *(i)* the NMR sequence used to create the required initial conditions; *(ii)* the numerical simulations used to check both the experiment and analysis method; and *(iii)* additional details that we had to take into account (i.e., signal-to-noise).

5.2 Measurement of persistence in 1-D diffusion

Glenn P. Wong, Ross W. Mair, Ronald L. Walsworth, and David G. Cory
Physical Review Letters *vol.* ***86****, pp. 4156–4159 (2001).*
This article has been reformatted to conform to Harvard dissertation guidelines.

Using a novel NMR scheme we observed persistence in 1-D gas diffusion. Analytical approximations and numerical simulations have indicated that for an initially random array of spins undergoing diffusion, the probability $p(t)$ that the average spin magnetization in a given region has not changed sign (i.e., "persists") up to time t follows a power law $t^{-\theta}$, where θ depends on the dimensionality of the system. Using laser-polarized ^{129}Xe gas, we prepared an initial "quasirandom" 1D array of spin magnetization and then monitored the ensemble's evolution due to diffusion using real-time NMR imaging. Our measurements are consistent with analytical and numerical predictions of $\theta \approx 0.12$.

The dynamics of non-equilibrium systems is a field of great current interest,

including such topics as phase ordering in binary alloys, uniaxial ferromagnets, and nematic liquid crystals, as well as coarsening of soap froth and diffusion of inhomogeneous fluids (*e.g.* [142]). The evolving spatio-temporal structures in these non-equilibrium systems depend crucially on the history of the system's evolution and are not completely characterized by simple measures such as two-time correlation functions. Therefore, an important problem in the study of non-equilibrium dynamics is the development of simple and easily measurable quantities that give nontrivial information about the history of the system's evolution. The recently identified phenomenon of "persistence" may be such a quantity: it characterizes the statistics of first passage events in spatially extended non-equilibrium systems [129–141,143–149]. Persistence is being actively studied in statistical physics; e.g., in the search for universal behavior in non-equilibrium critical dynamics [135,146,149]. Practically, persistence may be important in determining what fraction of a system has reached a threshold condition as a function of time; e.g., in certain chemical reactions or disinfectant procedures.

Consider a non-equilibrium scalar field $\phi(\mathbf{x}, t)$ fluctuating in space and time according to some dynamics (e.g., a random array of interdiffusing spins). Persistence is the probability $p(t)$ that at a fixed point in space the quantity $[\phi(\mathbf{x}, t) - \langle\phi(\mathbf{x}, t)\rangle]$ has not changed sign up to time t. It has been found that this probability decays as a power law $p(t) \sim t^{-\theta}$, where the persistence exponent θ is generally nontrivial and has been suggested as a new universal dynamic critical exponent [135, 146]. This exponent depends both on the system dimensionality and the prevalent dynamics [129, 130], and is difficult to determine analytically due to the non-Markovian nature of the phenomena. Although θ has been calculated – largely using numerical techniques – for such systems as simple diffusion [129–131], the Ising model [133, 134, 148], and the more generalized q-state Potts model [132, 133, 144], few

Dim.	**Diffusion**	**Ising**	**q-Potts**
1	0.12, **0.118**‡	3/8*, 0.35	$-\frac{1}{8}+\frac{2}{\pi^2}\left[\cos^{-1}\left(\frac{(2-q)}{\sqrt{2}q}\right)\right]^2{}^{*}$
2	0.19	0.22, 0.19†	0.86, 0.88† (large q)
3	0.24	0.26	
refs	*[129–131]*	*[133, 134] [140]*†	*[132, 133, 144] [141]*†

Table 5.1: A sample of reported persistence exponents. All values except those indicated are derived from numerical simulations; (*) denotes exact analytical results, (†) experimental measurements, and (‡) the result reported here.

measurements of persistence have been performed (see Table 5.1). In particular, "breath figures" [139], 2-D soap froth [141], and twisted nematic liquid crystals [140] are the only systems for which experimental results have been reported. Further experimental investigation is needed to probe the utility of persistence in studies of fundamental and applied non-equilibrium dynamics.

In this paper we present the first measurement of persistence in a system undergoing diffusion (i.e., dynamics governed by Fick's Law $\dot{\phi} = D\phi''$). Our experiment is also the first to observe persistence in one dimension (1-D). We employed a novel NMR technique to create an initial "quasi-random" spatial variation in the nuclear spin magnetization of a sample of laser-polarized ^{129}Xe gas. Subsequent 1-D NMR imaging allowed us to monitor the temporal evolution of the ensemble. We observed persistence by noting mean magnetization sign changes at fixed locations of constant size (i.e., imaging pixels) as a function of time. Using a simple theory (the "independent interval approximation") and numerical simulations, both Derrida *et al.* [130] and Majumdar *et al.* [129] independently found that $\theta \approx 0.121$ for 1-D diffusion. Newman and Toroczkai [131] found $\theta \approx 0.125$ in 1-D using an analytic expression for the diffusion persistence exponent. Our measurements are consistent with these calculations.

Recently, laser-polarized noble gas NMR has found wide application in both

the physical and biomedical sciences. Examples include fundamental symmetry tests [16], probing the structure of porous media [19], and imaging of the lung gas space [18]. These varied investigations, as well as the experiment reported here, exploit special features of laser-polarized noble gas: the large nuclear spin polarization ($\sim 10\%$) that can be achieved with optical pumping techniques; the long-lived nuclear spin polarization of the spin-1/2 noble gases ^{129}Xe and ^{3}He; and rapid gas-phase diffusion.

We performed laser-polarization of xenon gas using spin-exchange optical pumping [10]. We filled a coated cylindrical glass cell [150] ($\sim$ 9 cm long, 2 cm I.D.) with approximately 3 bar of xenon gas isotopically enriched to 90% ^{129}Xe, 0.5 bar of N_2 gas, and a small amount of Rb metal. We heated the sealed cell to $\sim 100^{\circ}$C to create a significant Rb vapor. Optical pumping on the Rb D1 line was achieved with 15 W of circularly-polarized 795 nm light (FWHM $\sim$ 3 nm) from a fiber-coupled laser diode array. After 20 minutes the ^{129}Xe gas was routinely nuclear spin-polarized to 1% by spin-exchange collisions with the Rb vapor. We next cooled the cell to room temperature in a water bath and placed the cell inside a home-made RF solenoid coil (2.5 cm diameter, 15 cm long, $Q \sim 900$) centered in a 4.7 T horizontal bore magnet (GE Omega/CSI spectrometer/imager) with ^{129}Xe Larmor frequency = 55.345 MHz. To allow the gas temperature to reach equilibrium, we left the cell in place for 20 minutes before starting the persistence measurements. At equilibrium under these conditions, the ^{129}Xe polarization decay time constant (T_1) was in excess of 3 hours, with a ^{129}Xe diffusion coefficient of 0.0198 cm^2/s [78]. (Note that changes in the sample gas pressure, and hence the diffusion coefficient, simply cause a rescaling of the time variable and do not affect the persistence power law $p(t) \sim t^{-\theta}$ [129].)

The NMR pulse sequence we used to observe persistence in laser-polarized ^{129}Xe

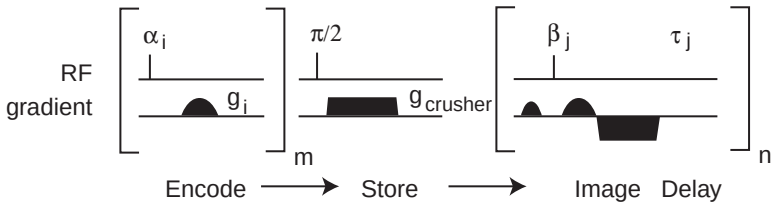

Figure 5.1: NMR pulse sequence used to encode a 1-D "quasi-random" pattern on the average magnetization of laser-polarized ^{129}Xe gas. Temporal evolution of the magnetization pattern is monitored with n repetitions of a 1-D FLASH imaging routine [82]. For example, with $m = 8$ encoding RF pulse/gradient pairs, the encoding pulse angles $\alpha_i = [30°, 35°, 37°, 41°, 45°, 50°, 63.5°,$ and $90°]$ while the encoding gradient amplitudes g_i were chosen randomly. The imaging pulse angle β_j was fixed at 8° and the diffusion times τ_j were varied from 2.4 ms up to ~ 2 s. The encoding gradients and the transverse magnetization dephasing "crusher" gradient were pulsed for 1 and 20 ms, respectively. Imaging gradients were applied for a total of 7.56 ms. The maximum gradient available was 6.7 G/cm.

gas diffusion is shown schematically in Fig. 5.1. The first portion of the pulse sequence encodes a 1-D "quasi-random" pattern on the transverse magnetization of the laser-polarized ^{129}Xe gas sample by using m pairs of variable-strength RF and magnetic-field-gradient pulses, repeated in rapid succession (see Fig. 5.1). Each pair of RF and gradient pulses adds different spatial Fourier components to the 1-D transverse magnetization pattern, with wavenumbers given by the gradient pulse area and Fourier component amplitudes set by the RF pulse area. Next, a $\pi/2$ RF pulse "stores" this quasi-random 1-D magnetization distribution along the longitudinal (z) direction while a subsequent strong (crusher) gradient pulse dephases any remaining transverse magnetization. The quasi-random longitudinal magnetization distribution then evolves with time due to diffusion and is monitored by a series of 1-D FLASH (Fast Low Angle SHot) NMR images [82, 151] (see Fig. 5.1).

The initial pattern of longitudinal ^{129}Xe magnetization is quasi-random in that there must be a minimum length scale to the induced variations in the ^{129}Xe mag-

netization, i.e., a maximum wavenumber in the pattern, for there to be sufficient NMR signal for useful imaging. (This minimum length scale was ≈ 0.6 mm in our experiment.) Nevertheless, at longer length scales the induced pattern must be random enough that persistence behavior can be expected. Ideally, $\langle \phi(x,0)\phi(x',0) \rangle = \delta(x-x')$; however, calculations indicate that it is sufficient for the initial condition correlator to decrease faster than $|x-x'|^{-1}$ for 1-D persistence [129]. We found that six to eight RF/gradient pulse pairs ($m = 6$–8) were optimal for the desired quasi-random 1-D patterning of the ^{129}Xe magnetization. $m < 6$ resulted in a pattern that was not sufficiently random, while $m > 8$ significantly reduced the signal-to-noise ratio (SNR) of the NMR images. The requirement of $m \geq 6$ is supported by numerical calculations in which we modeled the NMR encoding sequence and simulated the subsequent gas diffusion using a finite difference first-order forward Euler scheme [130, 152]: we found persistence behavior (i.e., $p(t) \sim t^{-\theta}$) only when $m \geq 6$. The requirement of $m \leq 8$ was set by the available NMR signal (i.e., the finite ^{129}Xe magnetization), the necessity of rapid data acquisition to avoid excessive diffusion during the imaging sequence itself, the limitation of approximately $2\pi \times (0.6 \text{ mm})^{-1}$ for the maximum wavenumber, and the maximum imaging gradient strength available.

For NMR imaging, we used a field of view (FOV) of 31.5 cm with 0.6 mm resolution, which thus divided the 9 cm cell into about 150 imaging pixels, each corresponding to a discernible spatial region of fixed size and location. We typically employed 8° excitation RF pulse angles and acquired 32 1-D images spaced logarithmically in time from ~ 3 ms to 5 s for a single experimental run. Longitudinal magnetization depletion due to imaging was highly uniform across the sample and did not affect the persistence measurement, since the relative magnetization amplitudes in neighboring imaging pixels was unchanged. An example of the images

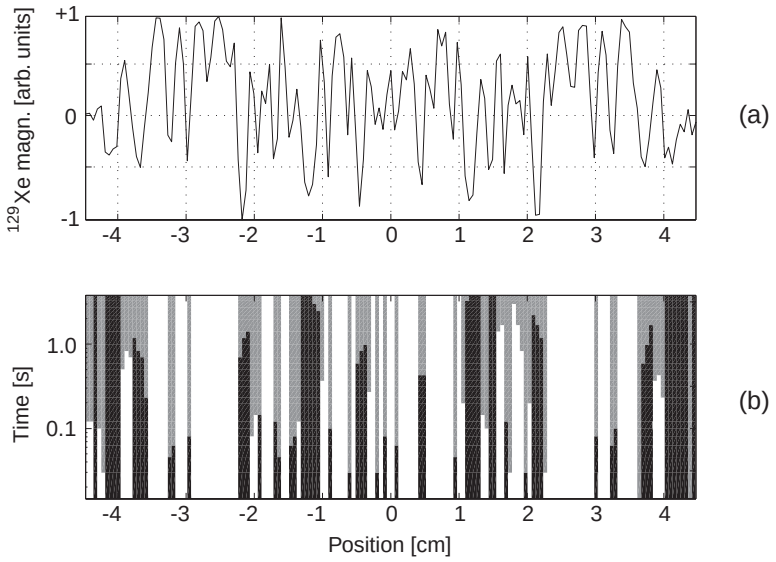

Figure 5.2: (a) Typical quasi-random initial pattern of ^{129}Xe magnetization resulting from 8 encoding RF pulse/gradient pairs. (b) 32 images of the evolving magnetization pattern were acquired at logarithmically increasing times. White (black) indicates average positive (negative) magnetizations for each of the 150 fixed-location imaging pixels of width ≈ 0.6 mm. Gray indicates pixels whose magnetization has changed sign at least once. The persistence exponent is determined from the growing fraction of gray pixels as a function of time.

acquired in a typical run are shown in Fig. 5.2. For each pixel, we derived average magnetizations (aligned or anti-aligned to the main magnetic field) from the phase information contained in the time-domain NMR image data, and spatial positions from the frequency information [153]. An experimental run thus provided a record of the ^{129}Xe gas magnetization in each pixel as a function of time proceeding from the initial quasi-random pattern to the equilibrium condition of homogeneous (near-zero) polarization.

To measure persistence, we noted the sign of the ^{129}Xe magnetization in each fixed spatial region (i.e., in each 1-D image pixel) and counted how many remained unchanged as a function of time. We equated the probability $p(t)$ with the fraction of pixels that had not changed sign up to time t. We chose $t = 0$ to coincide with

the first image and assigned the time index for each image to be the start time of the imaging RF pulse. Images with SNR < 40 were excluded from the data to minimize uncertainty in pixel sign changes. We conducted about 30 experiments with image SNR > 40, each with a unique set of randomly chosen encoding magnetic field gradients $\{g_i\}$. We observed that pixel sign changes occurred smoothly, so it was unlikely we missed sign changes with an error of more than one step in the imaging sequence. We employed two averaging schemes to combine the results from different experimental runs. In the first method, we used a linear least-squares fit of $\log[p(t)]$ vs. $\log[t]$ for each run, resulting in a distribution of power law exponents with a weighted mean $\theta = 0.119 \pm 0.048$. With our numerical simulations of quasi-random initial conditions, we found that this averaging scheme results in a gaussian distribution of exponents with a mean value $\theta \approx 0.12$ in agreement with previous calculations for 1-D diffusion [129–131] and our experimental results. In the second averaging scheme, we combined the data from all experimental runs; hence $p(t)$ represented the fraction of total pixels from all experiments that had not changed sign up to time t. We found $p(t) \sim t^{-\theta}$ with $\theta = 0.118 \pm 0.008$ for 0.1 s $\leq t \leq$ 1 s. Figure 5.3 shows a log-log plot of $p(t)$ vs. t when the data is averaged using this method.

The observed deviations from power law behavior for $t \lesssim 0.1$ s and $t \gtrsim 1$ s are explained by image resolution and finite size effects, respectively. At short times persistence is not observed because ^{129}Xe atoms have not yet diffused on average across a single 1-D image pixel (≈ 0.6 mm). The relevant diffusion time is $(0.6 \text{ mm})^2/(2D_{Xe}) \approx 0.1$ s for our typical experimental conditions. At long times, the coarsening of the ^{129}Xe magnetization pattern by diffusion results in large "domains" of adjacent pixels with the same sign of the magnetization. Our simulations indicate that persistence is not observed when there are few domains in the finite

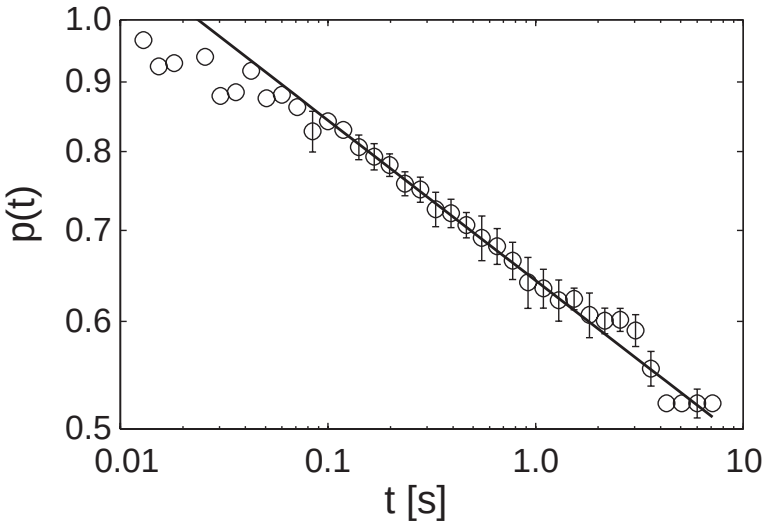

Figure 5.3: A log-log plot of $p(t)$, the fraction of regions (pixels) with ^{129}Xe spin magnetization that had not changed sign up to a time t, representing the sum of $\sim$ 30 different experimental runs. The solid line is a weighted linear least-squares fit to the data for 0.1 s $\leq t \leq$ 1 s, and yields $\theta = 0.118 \pm 0.008$. Error bars are derived from the number of pixels with amplitudes close to the image noise level and are shown when they exceed the plot symbol diameter.

size sample because the number of magnetization boundaries is greatly reduced; hence the rate of pixel sign-changing (i.e., the growth of the gray area in Fig. 5.2) is curtailed. Both the short and long-time deviations are seen in Fig. 5.4, where the average length L of like-signed magnetization domains from all experimental runs is plotted against time. For 0.1 s $\lesssim t \lesssim$ 1 s, our data are in reasonable agreement with the expected power law $L \sim t^{1/2}$ for diffusion [142]. For $t \gtrsim 1$ s, we find $L \gtrsim 1$ cm, implying there are typically less than 10 magnetization boundaries in the 9 cm long sample cell.

In conclusion, we experimentally measured a persistence exponent $\theta \approx 0.12$ for 1-D diffusion, consistent with analytical and numerical studies. We performed the measurement using a novel NMR scheme with laser-polarized ^{129}Xe gas which allowed us to both encode a spatially "quasi-random" magnetization pattern and

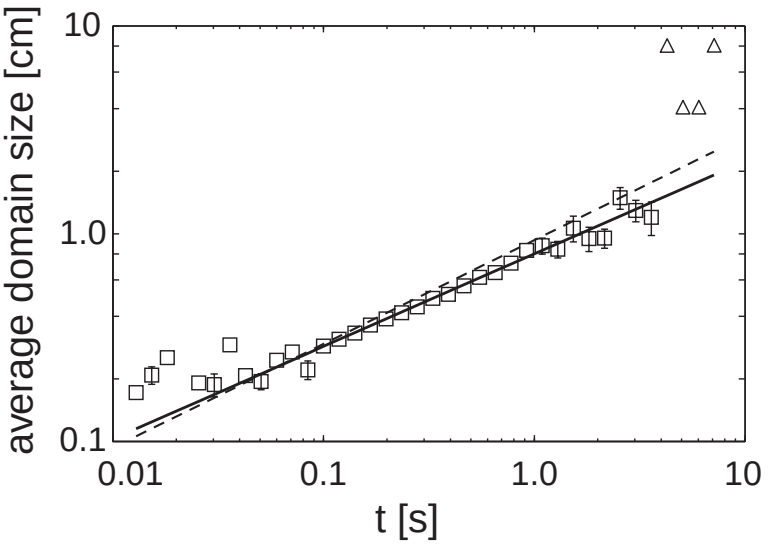

Figure 5.4: The average size L of domains of adjacent pixels with uniform magnetization orientation, as a function of time t, derived from all experimental runs. For $0.1\text{ s} \leq t \leq 1\text{ s}$, $L \sim t^{\alpha}$ where $\alpha = 0.45 \pm 0.02$ (solid line). The dotted line shows the expected $L \sim t^{1/2}$ behavior for an infinite system. The error in L is shown where it exceeds the plot symbol size. The finite size limit on L is evident in the four late-time points ($\triangle$), which were taken from the only two runs with sufficient SNR at long times.

monitor its evolution over several seconds. We also observed the effect of finite sample size for long-time diffusion. In future work the experimental technique employed in this study may allow measurements of persistence in 2 and 3-D diffusion, in heterogeneous systems (e.g., porous media) infused with noble gas, and in 'patterns' [154].

The authors thank Satya Majumdar, Michael Crescimanno, and Lukasz Zielinski for useful discussions. This work was supported by NSF Grant No. CTS-9980194, NASA Grant No. NAG9-1166, and the Smithsonian Institution Scholarly Studies Program.

5.3 Quasi-random spatial encoding

5.3.1 Introduction

Persistence is observed when the initial magnetization configuration is random; however, such a situation is incompatible with NMR signal detection. We address this issue by creating a "quasi-random" distribution of magnetization; in other words, a distribution of magnetization that is random at long length scales, but is sufficiently non-random at short length scales (i.e., on the order of an imaging pixel) to allow sufficient ensemble magnetization for NMR detection. The purpose of this section is to describe in greater detail the NMR pulse sequence we employed to achieve this. Furthermore, we shall use the k-space formalism introduced by Hennig [155] and developed by Sodickson and Cory [156] to facilitate the understanding of the sequence and resulting magnetization distribution.

In addition, we shall briefly present experimental 1-D images of the quasi-random spatial magnetization in a sample of laser-polarized ^{129}Xe. While in principle this experiment could be performed in a thermally-polarized sample, the laser-polarized noble gas offered distinct advantages for the purposes of this experiment, including high polarization ($\sim 1\%$), fast diffusion (~ 0.02 cm^2/s at 3 atm.), and long T_1 at 4.7 T (≈ 3 hours in an OTS-coated glass cell [150]).

5.3.2 Theory

Figure 5.1 shows the pulse sequence we used for our persistence measurement. It consists of the following three parts: first, m repetitions of variable-strength RF/gradient pulse pairs encodes the quasi-random *transverse* spin magnetization; next, a $\pi/2$ pulse followed by a strong dephasing (crusher) gradient pulse effectively

stores the quasi-random pattern in the *longitudinal* spin magnetization and dephases any residual transverse magnetization; finally, a series of n 1-D FLASH (Fast Low Angle SHot) images acquired at varying times monitor the temporal evolution of the magnetization pattern.

Review of the k-space formalism

As mentioned earlier, the reciprocal or k-space formalism provides a clear and convenient framework for understanding how the encoding portion of the sequence results in a "quasi-random" spatial magnetization distribution. We present here a brief review of the relevant concepts of the formalism as described by Sodickson and Cory [156].

In the presence of a magnetic field gradient $G_u = \partial B_z/\partial u$, transverse magnetization accumulates varying amounts of phase along the $\hat{u}$ direction in the laboratory frame. Assuming G_u is constant, the phase varies linearly and can be described by a spatial wavenumber (or frequency) k, which changes as follows:

$$\Delta k_u^{trans} = \gamma \int G_u dt. \tag{5.1}$$

where $k = 2\pi/\lambda$, λ being the wavelength of the modulation. Note that the magnetic field gradients do not affect longitudinal magnetization.

For convenience, it is useful to map the transverse magnetization M_{trans} to the complex plane, with the convention that (in the rotating frame) M_x is real and M_y is imaginary. Phase modulations due to a gradient pulse result in a spatial "helix" of magnetization described by $e^{i(k_u u+\theta)}$, where θ is a global phase offset. Note that by simply inverting one component of the transverse magnetization (e.g., with a $\pi|_x$ RF pulse) or applying a magnetic field gradient of opposite sign instead, it is possible

to reverse the sense of the helix. Consequently, phase modulations of the transverse magnetization can be described by either right or left-handed helices $e^{i(\pm k_u u+\theta)}$. It is common to refer to them as "magnetization gratings" with wavenumbers $\pm k_u$.

In contrast to gradient pulses, which only affect the transverse magnetization phase gratings, RF pulses mix the longitudinal and transverse magnetization gratings and affect their relative amplitudes. On-resonant RF pulses have a fixed phase in the transverse (complex) plane, and cause the orthogonal components of magnetization to precess. For example, a $\pi/2|_x$ pulse will cause a $\pi/2$ rotation in M_z and M_y, but not M_x. RF pulses (of angle α) thus mix transverse gratings (i.e., $A_1 e^{\pm i(k_u u+\theta)} \xrightarrow{\alpha} A_1' e^{\pm i(k_u u+\theta)} + A_2' e^{\mp i(k_u u+\theta')}$) while also creating (from a portion of the transverse magnetization) a longitudinal magnetization grating of *amplitude* modulation given by $A'' \sin(\pm k_u u + \theta'')\hat{z}$. Similarly, preexisting longitudinal gratings of wavenumber k_u' and phase θ''' are rotated into the transverse plane, resulting in linear combinations of the transverse gratings $e^{\pm i k_u' u+\theta'''}$. The strength of the RF pulse (i.e., the flip angle α) determines the amount of mixing between longitudinal and transverse magnetizations.

It is possible to express any spatial magnetization modulation by using the three basis functions $\mathbf{m}_+(k_u,\theta) = e^{i(+k_u u+\theta)}, \mathbf{m}_-(k_u,\theta) = e^{i(-k_u u+\theta)}$, and $\mathbf{m}_z(k_u,\theta) = \sin(k_u u+\theta)\hat{z}$. With these basis functions, the transformations due to an RF pulse α_ϕ can be written as follows:

$$\begin{bmatrix} \mathbf{m}_+(k_u,\theta) \\ \mathbf{m}_-(k_u,\theta) \\ \mathbf{m}_z(k_u,\theta) \end{bmatrix} \overset{\alpha_\phi}{\Rightarrow} \begin{bmatrix} \cos^2(\frac{\alpha}{2})\mathbf{m}_+(k_u,\theta) & \sin^2(\frac{\alpha}{2})\mathbf{m}_-(k_u,-\theta+2\phi) & \sin(\alpha)\mathbf{m}_z(k_u,\theta-\phi) \\ \sin^2(\frac{\alpha}{2})\mathbf{m}_+(k_u,-\theta+2\phi) & \cos^2(\frac{\alpha}{2})\mathbf{m}_-(k_u,\theta) & \sin(\alpha)\mathbf{m}_z(k_u,-\theta+\phi+\pi) \\ \frac{1}{2}\sin(\alpha)\mathbf{m}_+(k_u,\theta+\pi+\phi) & \frac{1}{2}\sin(\alpha)\mathbf{m}_-(k_u,-\theta+\phi) & \cos(\alpha)\mathbf{m}_z(k_u,\theta) \end{bmatrix} \tag{5.2}$$

where ϕ is the phase of the RF pulse ($\phi = 0$ is equivalent to having an RF pulse along the $\hat{x}$ axis in the rotating frame, i.e., α_x).

When using a homogeneous RF coil for detection in a homogeneous spin-density sample, only the k=0 grating of M_{trans} yields an observable NMR signal; non-zero k gratings result in spatially phase-modulated RF signals that destructively interfere when integrated over the volume of the coil. In order to detect the non-zero k gratings, one must apply a gradient to "unwind" the phase until k=0.

A useful tool for visualizing the k-space formalism is to graph k-components as a function of time. As an example, Fig. 5.5 illustrates the simple case of a two-pulse spin echo sequence in the presence of a constant field gradient[1]. The first $\pi/2|_y$ pulse[2] places all the magnetization into the transverse plane. In the presence of the gradient G_u, the magnetization "winds" up with increasing k; in particular, $\partial k/\partial t = \gamma G_u$, and when $t = \tau$, one has $k = k_1 \equiv \gamma G_u \tau$. Assuming a global phase factor of zero, the second $\pi/2|_y$ pulse then transforms $\mathbf{m}_+(k_1, 0)$ into a mixture that includes $\mathbf{m}_+(k_1, 0)$, $\mathbf{m}_-(k_1, 2\phi)$, and the longitudinal grating $\mathbf{m_z}(k_1, -\phi)$. The relative amplitudes of each grating can be computed using eq. 5.2: for the gratings $\mathbf{m}_+$ and $\mathbf{m}_-$ we have $\cos^2(\pi/4)$, $\sin^2(\pi/4)$, respectively, while the longitudinal grating $\mathbf{m_z}$ has an amplitude of $\sin(\pi/2)$. These values are found in Fig. 5.5 on the appropriate pathways.

Note that a spin echo is detected at $t = 2\tau$ when the negative k grating passes through zero. Furthermore, the diagram shows that the longitudinal grating $\mathbf{m}_z(k_1, \theta)$ (dashed line) does not evolve in the presence of the gradient. Similarly the transverse k-values remain fixed once the gradient is turned off.

[1] This example represents the famous Hahn spin echo experiment [69].
[2] recall, $\phi = \pi/2$ for a $\alpha|_y$ pulse.

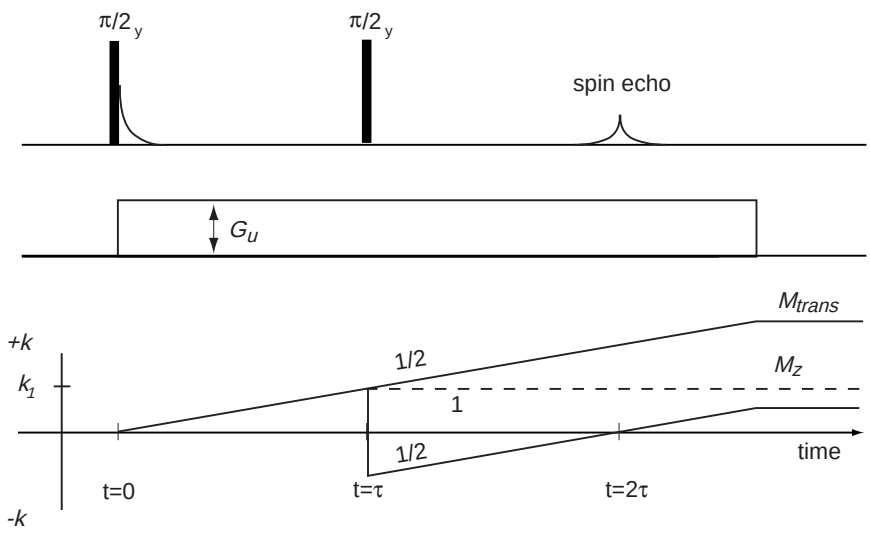

Figure 5.5: Two-pulse spin echo pulse sequence in the presence of a constant field gradient G_u. On the k-space diagram, the solid lines represent the wavenumbers of transverse magnetization gratings; the dashed line is the wavenumber of the longitudinal amplitude grating. The numbers represent the relative amplitude of the different gratings following the second $\pi/2$ pulse.

Quasi-random encoding

We are now prepared to discuss the details of the quasi-random encoding sequence. As shown in Fig. 5.1, there are m iterations of a variable strength RF pulse α_i, followed by a gradient pulse of random magnitude g_i. The random magnitude gradient pulse creates and changes the wavenumbers of transverse magnetization gratings, while the RF pulses continually mix between longitudinal and transverse magnetizations. Consequently, the entire ensemble is transformed into gratings with different k-values at a geometric rate, resulting in a quasi-random spatial magnetization that is predominantly in the transverse plane (i.e., in M_{trans}). The storage $\pi/2$ pulse and subsequent crusher pulse places the pattern in M_z and dephases any remaining transverse magnetization. The resulting quasi-random pattern in M_z is then free to evolve by diffusion. Using fast, low flip-angle imaging along the $\hat{u}$ direction in the

laboratory frame (i.e., FLASH imaging [82]; see also sec. 3.3.3), we could monitor the evolution of the pattern as a function of time. As a final note, it should be clear that the "quasi-randomness" of the pattern depends on m (the number of encoding RF pulse/gradient pairs) and the different choices for α_i and g_i.

The sequence is fairly straightforward to understand in the trivial case where $m = 1$. After some initial RF pulse α_1 (we will assume for simplicity and without loss of generality that all RF phases are aligned with $\hat{x}$ [i.e., $\phi = 0$] and the initial phase factor $\theta = \pi/2$), eq. 5.2 can be used to show that $M_z = M_0 \cos(\alpha_1)$ while the transverse magnetization $M_{trans} = M_0(\sin(\alpha_1)/2)\left[\mathbf{m}_+(0, \pi/2 + \pi) + \mathbf{m}_-(0, -\pi/2)\right]$ $= M_0 \sin(\alpha_1)\mathbf{m}_+(0, -\pi/2)$, as expected (recall, imaginary values are aligned along $\hat{y}$). After the gradient pulse of strength g_1, the transverse magnetization has been "wound up" to a k-value given by $k_1 = \gamma g_i \int f(t)dt$, where $f(t)$ is the shape of the gradient pulse (to avoid eddy currents resulting from fast gradient switching, it was more convenient to use half-sine shaped pulses rather than rectangular pulses). As mentioned above, M_{trans} is stored in M_z after encoding via a $\pi/2$ RF pulse, so with $m = 1$, we are left with a single sinusoidal modulation in M_z with wavenumber k_1 and amplitude $M_0 \sin(\alpha_1)$.

For $m > 1$, the situation becomes more complicated, but is straightforward to analyze with the above formalism. As before, the first α_1 RF pulse and g_1 gradient pulse leave a k=0 magnetization grating in M_z and a k=$+k_1$ grating in M_{trans}. The next RF pulse (α_2) transforms the $+k_1$ grating into a linear combination of $\pm k_1$ transverse gratings and a $+k_1$ longitudinal grating, while a new transverse grating with k=0 emerges from M_z. After the second (g_2) gradient pulse (which adds k_2 to preexisting transverse wavenumbers), M_{trans} becomes a combination of k_1+k_2, $-k_1+k_2$, and k_2 transverse gratings. On the other hand, M_z is now comprised of gratings with wavenumbers k_1 and k=0. Additional RF and gradient pulses create

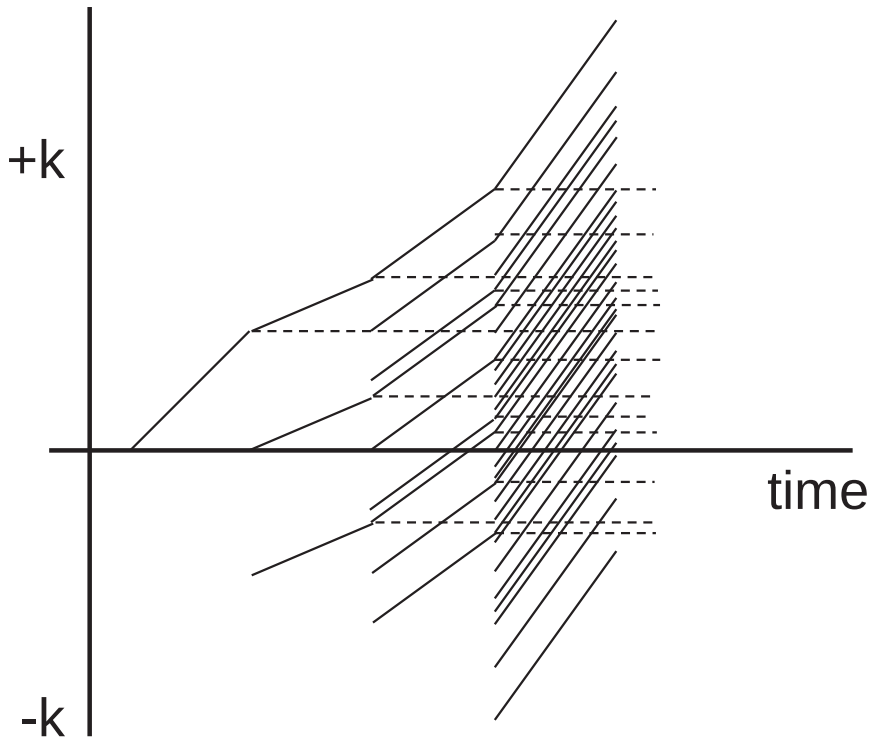

Figure 5.6: A k-space diagram for the encoding sequence when $m = 4$. Solid lines represent the wavenumbers of transverse gratings; dashed lines are k-values for longitudinal amplitude gratings. The different slopes reflect the randomly chosen g_i gradient strengths. RF pulses were applied at each point in time where new grating wavenumbers appear.

yet more gratings, with wavenumbers that are linear combinations of the different $[k_i]$.

Figure 5.6 shows an example of how quickly different magnetization gratings appear during the encoding sequence. To maximize the number of gratings for a given m, two conditions are necessary:

(i) the different gradient strengths g_i should not be multiples or linear combinations of one another, otherwise a "new" grating may overlap with a previous one;

(ii) the RF pulse angles α_i should not be multiples of $\pi/2$. If they are, some of the mixing amplitudes from eq. 5.2 would equal zero, thus reducing the

number of gratings created.

We can analytically determine the maximum number of gratings present in the ensemble after m repetitions of the encoding sequence. Let l_m and t_m represent the number of longitudinal and transverse gratings present after m RF and gradient pulse pairs, assuming the above conditions are satisfied. For $m = 1$, $l_1 = 1$ and $t_1 = 1$, corresponding to a longitudinal grating with k=0 and a transverse grating with k=k_1. For $m = 2$, the longitudinal grating creates a new transverse grating (k_2), while the transverse grating is the source for 2 new transverse gratings ($k_1 + k_2, -k_1 + k_2$) and a new longitudinal grating (k_1). Generalizing for all $m > 1$, we obtain the following difference equations:

$$\begin{aligned} t_m &= 2t_{m-1} + 2\left(l_{m-1} - 1\right) + 1 \\ l_m &= t_{m-1} + l_{m-1}. \end{aligned} \tag{5.3}$$

These equations can be solved to yield the following:

$$\begin{aligned} t_m &= 3^{m-1} \\ l_m &= \frac{1}{2}\left(3^{m-1} + 1\right) \end{aligned} \tag{5.4}$$

The relative strength of each transverse and longitudinal grating is dependent on the RF pulses $[\alpha_i]$ in a nontrivial way. However, it is possible to calculate each amplitude using eq. 5.2 in an iterative fashion. For example, the transverse grating with the largest k-value (i.e., $k_{max} = \sum_1^m k_i$) after $m > 1$ iterations of the encoding sequence will have an amplitude:

$$A^m_{max\ k} = \sin(\alpha_1) \prod_{i=2}^{m} \left[\cos^2\left(\alpha_i/2\right)\right]. \tag{5.5}$$

Similar expressions can be derived for any of $(t_m + l_m)$ transverse and longitudinal gratings.

As mentioned earlier, our definition of "quasi-randomness" is a pattern uncorrelated at long length scales, but sufficiently non-random at a length scale comparable to an imaging pixel so that NMR imaging is possible. Translating that into the present formalism, we want a pattern with as many (transverse) gratings as possible, each with a different k-value, subject to the condition that $k_{max} \lesssim 2\pi/(dx)$, where dx is the imaging pixel size. Furthermore, the mean difference between "adjacent" k-values must not exceed a minimum value that is determined by the acquisition parameters. In other words, one cannot set m arbitrarily high and use vanishingly small values for g_i such that $\left(\gamma \sum_{i=1}^{m} g_i \int f(t)dt\right) \lesssim 2\pi/(dx)$, since this would result in indiscernibly different k-values. Experimentally, this means that the number of points acquired to form an image sets a limit on the number of discernible gratings, while the strength of the imaging gradient determines the imaging pixel size, and hence k_{max}. Of course, an overriding consideration is the amount of magnetization available and the level of signal-to-noise (SNR) which is acceptable to form an image. It should be noted that our discussion of k_{max} should not be taken as a hard upper limit on k. In fact, because of the high spin polarization of the laser polarized noble gas, we could afford to exceed k_{max} (which results in less overall signal) to ensure a more random initial configuration. Further details will be discussed in the following section.

5.3.3 Experiment

Experiments were as described in section 5.2 [128]. In particular, we used a 4.7 T horizontal bore magnet (GE Omega/CSI spectrometer/imager), where the ^{129}Xe

Imaging parameters	value	
flip angle	8°	
points acquired	512	
sweep width	200000	Hz
gradient pulse duration	2	ms
refocus (acquisition) time	2.56	ms
field of view (FOV)	310	mm
max. gradient avail.	6.7	G/cm

Table 5.2: Parameters used for 1-D FLASH imaging of the longitudinal magnetization following the quasi-random spatial encoding sequence. Key priorities in imaging include resolution and rapidity, with constraints given by maximum available gradient strength and the maximum digitizer rate.

Larmor frequency is 55.345 MHz. The sample was a sealed cylindrical glass cell ($\sim$ 9 cm long, 2 cm i.d.) filled with 3 bar of enriched (90%) ^{129}Xe, 0.5 bar N_2, and a macroscopic amount of Rb (the ^{129}Xe diffusion coefficient $D_{Xe} = 0.0198$ cm^2/s). Laser polarization was accomplished in the fringe field of the magnet as described in sec. 2.3.

We used a transverse solenoid, optimized for high homogeneity over the length of the sample cell, as the RF excitation and NMR signal detection coil[3]. The axis of the coil was coincident with the G_x gradient (i.e., $\partial B_z/\partial x$), which we used for both quasi-random encoding and 1-D FLASH imaging. Therefore, $\hat{u} = \hat{x}$ in the above formalism. The maximum field gradient possible from the available hardware was 6.7 G/cm. Typical imaging parameters are listed in Table 5.2.

The earlier discussion on the quasi-random encoding sequence assumed no diffusion or T_2 decoherence; in reality, these are important factors and to minimize their impact on the sequence, we made the encoding sequence as short as possible. The encoding gradient was pulsed for 1 ms in a half-sine waveform (to minimize eddy currents), and we found that setting $m = 6 - 8$ resulted in a sufficiently "random"

[3]A detailed discussion of the solenoid design is found in Appendix A.

magnetization pattern. We support this claim in a number of ways:

(i) given the imaging parameters listed in table 5.2, the imaging resolution is 0.06 cm, which sets both the minimum length scale for signal detection and the maximum detectable k-grating, i.e., $k_{max}^{resolution} = 2\pi/(2 \times 0.06 \text{ cm}) = 52 \text{ cm}^{-1}$. Assuming $\langle g_i \rangle = 3.3$ G/cm, the maximum k-value after $m = 6$ iterations of the encoding sequence yields $k_{max}^{m} = \gamma(6 \times 3.3 \text{ G/cm})(0.001 \text{ s}/\pi) \int_0^\pi \sin(x)dx = 95 \text{ cm}^{-1}$. Similarly, for m=7 and 8, $k_{max}^{m} = 110$ and 126 cm^{-1}, respectively. Thus, the encoding sequence with $m = 6 - 8$ has the potential to create gratings that exceed the detection resolution. Ideally, the largest k-values generated match $k_{max}^{resolution}$, since any k-values above the resolution limit are undetectable and only degrade the SNR by using up valuable polarization.

(ii) the time domain signal acquired during the imaging sequence is essentially a map of the spatial fourier (k) space; thus, by acquiring 512 points, we can discern at most 512 different k-valued gratings (half of which have $k < 0$ and the other half have $k > 0$). By choosing $m = 6, 7, 8$, we can generate up to 243, 729, and 2187 gratings with the encoding sequence (see eq. 5.4)[4].

We therefore create close to the maximum number of modulation components we can detect with $m = 6$, and in the case of $m = 7$ or 8 we potentially exceed the limit by a fair amount. Having too many magnetization gratings in the sample is not a problem so long as the overall SNR is acceptable (in the

[4]Actually, the imaging sequence transforms a portion of the stored longitudinal gratings into transverse gratings that may be detected as they pass through k=0; in particular, eq. 5.2 shows that a longitudinal k-grating goes to both $\mathbf{m}_-$ and $\mathbf{m}_+$ in equal proportions. Hence the detected number of *unique* gratings is halved. In our case, because we acquire 512 (time) data points, we can discern $512/2 = 256$ different longitudinal gratings, even though the signal is comprised of up to 512 *transverse* gratings.

extreme case of infinite gratings, the sample would be fully randomized but have an SNR = 0).

5.3.4 Results

Figure 5.7 shows an example 1-D NMR image of an initial magnetization configuration generated using the quasi-random encoding sequence with $m = 7$. To illustrate clearly the randomness of such a configuration, we analyzed the autocorrelation of several independent initial configurations that were appended to each other. In other words, we artificially created a much larger sample by pasting together the results from numerous experiments such as that shown in Fig. 5.7. Figure 5.8 presents the autocorrelation of an array consisting of 7 separate initial configurations (4 of them were created with $m = 7$; the other 3 had $m = 8$).

Figures 5.7 and 5.8 illustrate an important point we have yet to address. In particular, the quasi-random encoding scheme creates a magnetization configuration that is symmetric about the center of the magnetic field gradient (in our experiments, this coincides with the geometric center of the cell). This occurs because of the odd symmetry of the magnetic field gradient (i.e., $G_x x = -G_x(-x)$), and results in a configuration that is effectively only half as random as originally desired. Of course, one way to create a fully quasi-randomized configuration would be to simply place one end of the cell near the magnetic field gradient center. However, as the cell is placed off center in such a fashion, the homogeneity of the main magnetic field may not be very good or the linearity of the magnetic field gradient may deteriorate, thus causing other problems with the configuration and later image analysis. We believe that in our experiments, the symmetry in each initial configuration was actually beneficial, as it served as a way for us to run the experiment twice – simultaneously

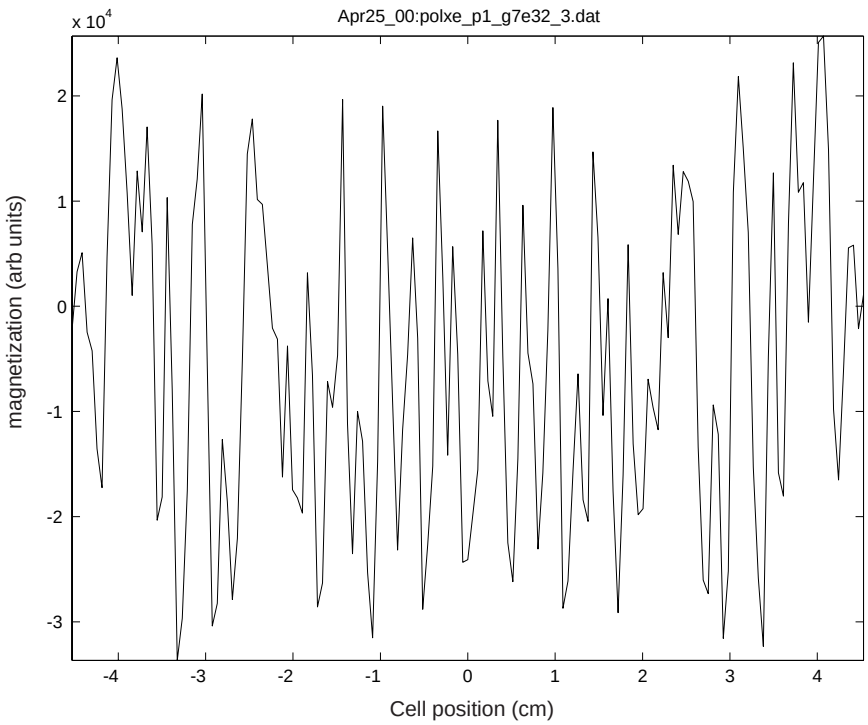

Figure 5.7: Example of a quasi-random initial condition created in laser-polarized ^{129}Xe, cell P-1. 7 encoding gradient pulses were used, with $g_i = (6.7\ \mathrm{G/cm}\times)[0.335\ .13\ .121\ .327\ .362\ .456\ .219]$; each pulse was a shaped half-sinusoid lasting 1 ms.

– with the same initial conditions. In this way small random fluctuations across the cell are averaged out, but we have yet to confirm this hypothesis; future studies will address this issue.

As a final comment, we note that the quasi-random encoding sequence (Fig. 5.1) is very similar to the single-shot diffusion measurement (SSDM) sequence described by Peled *et al.* [26] (see Fig. 5.9). In fact, SSDM can be considered a special case of the quasi-random encoding sequence with the following two constraints: first, all the RF pulses (α_i) must be small, and second, the encoding gradient is constant in magnitude and continuously on; this is equivalent to setting all the quasi-random encoding gradients (g_i) to the same value.

The first constraint is meant to limit the mixing of k-gratings; the SSDM mea-

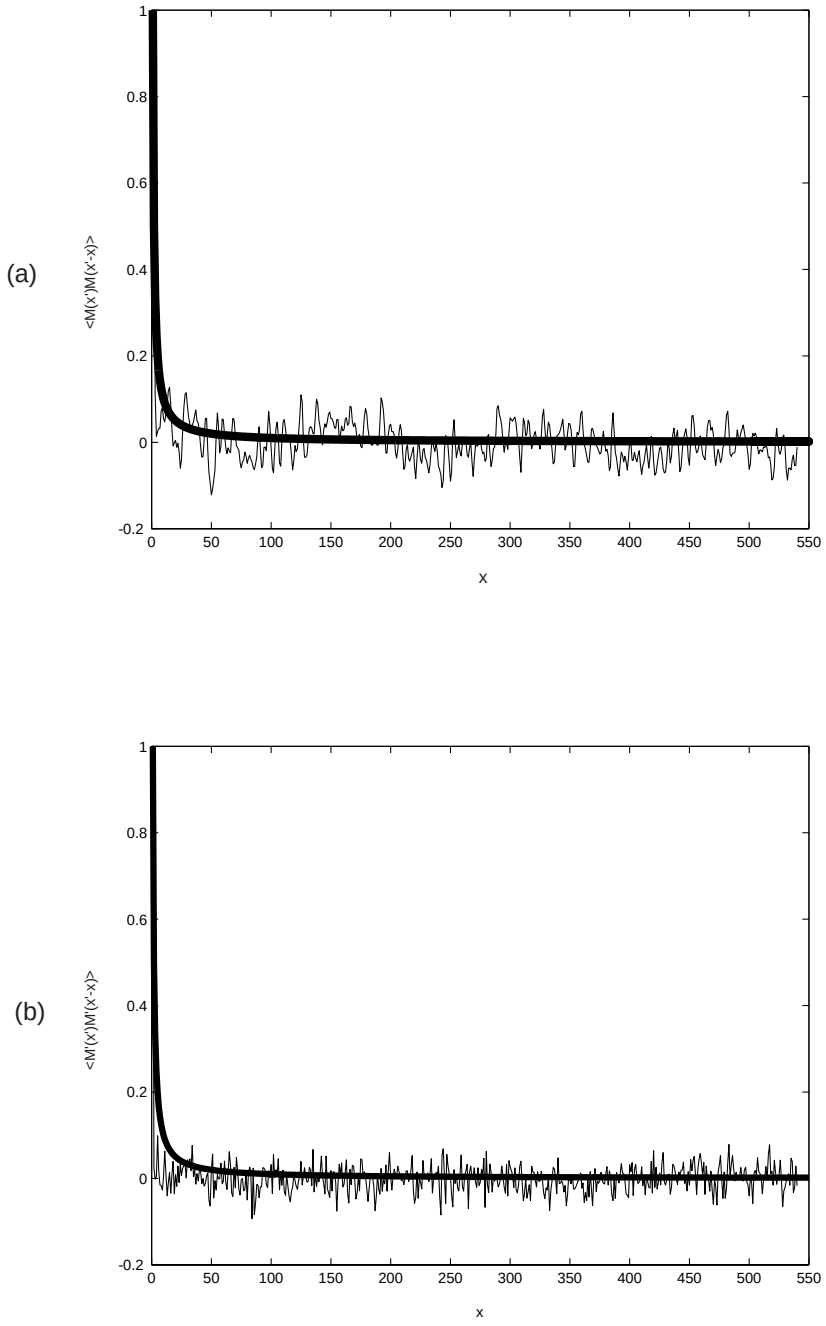

Figure 5.8: Comparison autocorrelations of the initial conditions. (a) The autocorrelation $\langle M(x')M(x'-x)\rangle$ of 7 independent (normalized) experimental initial configurations linked together to form a "macro" configuration array $M(x')$. The apparent undulations have a period equal to the length of the sample cell, and result from the symmetrized nature of the magnetization configuration about the cell center. (b) The autocorrelation $\langle M'(x')M'(x'-x)\rangle$ of a computer-generated random array $M'(x')$ of length equal to the "macro" array $M(x')$. The heavy line in both plots is the function $1/x$, which is the ideal autocorrelation function of the initial configuration [129].

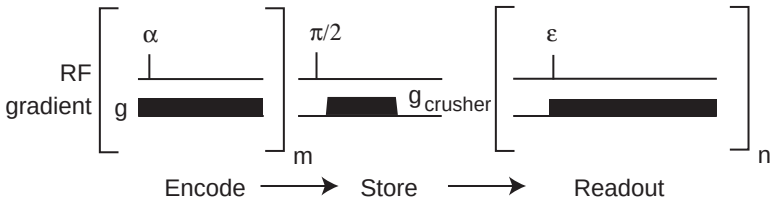

Figure 5.9: Pulse sequence for the single-shot diffusion measurement (SSDM) [26]. Similar to the quasi-random encoding sequence, SSDM "winds" a number of transverse magnetization gratings and then "stores" them in the longitudinal magnetization. The different longitudinal k-gratings decay at different rates as dictated by diffusion (i.e., $\exp(-k^2Dt)$), which are simultaneously detected during the readout portion of the sequence. See ref. [26] for more details.

surement only examines the $+k$–components of the transverse magnetization originally created from the k=0 longitudinal magnetization, and minimizes/ignores -k–components or any $+k$ transverse magnetization resulting from $k \neq 0$ longitudinal magnetization. The second constraint means that the k-gratings created by the SSDM are multiples of one another and thus simplify the determination of the diffusion coefficient.

5.4 Numerical simulations

This section describes the numerical simulations we used to investigate the feasibility of our persistence experiment and to validate the analysis schemes we used. We begin by describing the simple difference algorithm for modeling the diffusion equation; by using this algorithm, we are able to reproduce the published results for persistence in a diffusive system. Next, we model the quasi-random encoding scheme and simulate its effectiveness for producing persistence behavior. Finally, we present the results from simulated NMR experiments and describe the analysis schemes we used to derive a persistence exponent. Because we did not have unlimited access to an NMR facility, these numerical simulations expanded our ability to conduct "experiments" off-line, and for example, enabled us to ascertain the extent to which the data block size would play a role in determining the experimental resolution.

5.4.1 Numerical simulation of the diffusion equation

To simulate the 1D diffusion equation $\frac{\partial u}{\partial t} = D\frac{\partial^2 u}{\partial x^2}$, we used the "Forward Time Centered Space" (FTCS) algorithm[5] as described in *Numerical Recipes* [152]:

$$\frac{u_j^{n+1} - u_j^n}{\Delta t} = D\left[\frac{u_{j+1}^n - 2u_j^n + u_{j-1}^n}{(\Delta x)^2}\right] \tag{5.6}$$

where n denotes the time step index and j is the spatial coordinate index. We can easily solve for u_j^{n+1}:

$$u_j^{n+1} = u_j^n\left[1 - 2\frac{D\Delta t}{(\Delta x)^2}\right] + \frac{D\Delta t}{(\Delta x)^2}\left[u_{j+1}^n + u_{j-1}^n\right] \tag{5.7}$$

[5]This is also known as the finite difference first-order forward Euler scheme [130].

Note that this is a generalized version of the expression used by Majumdar *et al.* [129] and Derrida *et al.* [130] in their back-to-back papers presenting the first calculations of persistence in diffusion. The only difference is that the expressions cited in their papers make the assumption that $\frac{D}{(\Delta x)^2} = 1$. von Neumann stability analysis [152] requires that

$$\frac{2D\Delta t}{(\Delta x)^2} \leq 1. \tag{5.8}$$

this requirement simply means that the difference equation is only valid for simulating the diffusion equation if the timestep used is smaller than 1/2 the time needed to diffuse across a cell of width Δx.

The diffusion simulation algorithm was coded into MATLAB[6] running on an Apple Macintosh[7] computer. Random initial spin configurations were created from a random gaussian distribution of zero mean and unit standard deviation[8]; the evolution of the configuration was then simulated using eq. 5.7. We determine the probability $p(t)$ of a spin *not* flipping up to time t by noting the sign of each spin (i.e., "bin") in the initial configuration, and then keep track of when the first sign change occurs in each bin. Figure 5.10 shows a plot of $\log(p(t))$ vs. $\log(t)$ for a system with 10^4 bins and $t_{max} = 10^2$. 300 separate simulations were performed with different initial configurations, and the results are summed together in Fig. 5.10 (except for the $2 \times 300 - 2$ boundary points, this is roughly equivalent to simulating a system that consists of $10^4 \times 300 = 3 \times 10^6$ bins). The log-log plot is linear and thus follows a power law $p(t) \sim t^{-\theta}$, where we find that $\theta = 0.1209 \pm 0.0003$ for these simulations (the first few points plotted were excluded from the linear fit, since

[6]version 5.2, The Mathworks Inc., 3 Apple Hill Drive, Natick, MA 01760-2098.

[7]Apple, 1 Infinite Loop, Cupertino, CA 95014.

[8]Similar results were obtained using a uniform distribution of random numbers between -1 and 1, which agrees with the findings of Majumdar *et al.* [129]. In addition, they tested a number of different random number generators and did not notice any effect on the simulations.

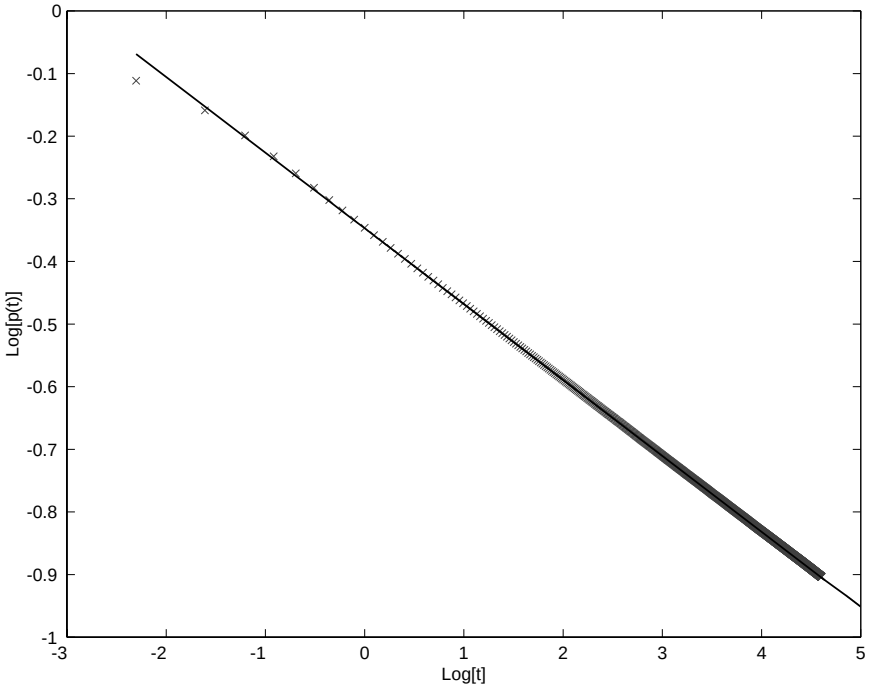

Figure 5.10: Numerical simulation results, showing persistence behavior in 1D diffusion. $p(t)$ is the fractional number of spins not flipped up to time t, and for long times, $p \sim t^{-\theta}$, where $\theta \approx 0.1209 \pm 0.0003$ for the data shown (plotted as solid line). The simulation used an array of 10^4 bins, $t_{max} = 100$, $\Delta t = 0.1$ and $a = D/(\Delta x)^2 = 1$. The plot shown represents the accumulation of 300 runs, each of which used a different random initial configuration drawn from a gaussian distribution of zero mean and unit standard deviation. On an Apple iMac computer (233 MHz G3 processor), the 300 simulations took ~ 100 minutes of processing time.

they represent short times where the diffusion length ($\sqrt{Dt}$) has not exceeded the bin size (Δx)). The result from these simple simulations is in good agreement with the results published by Majumdar *et al.* ($\theta_{\rm 1D} = 0.1207 \pm 0.0005$ [129]) and Derrida *et al.* ($\theta_{\rm 1D} \sim 0.1203$ [130]), and verify that both the diffusion simulator and the analysis scheme have been appropriately implemented.

An alternate way to examine the data is to extract a persistence exponent for each individual simulation, and then calculate the mean value of the distribution of exponents (see Fig. 5.11). The different persistence exponents obtained from the

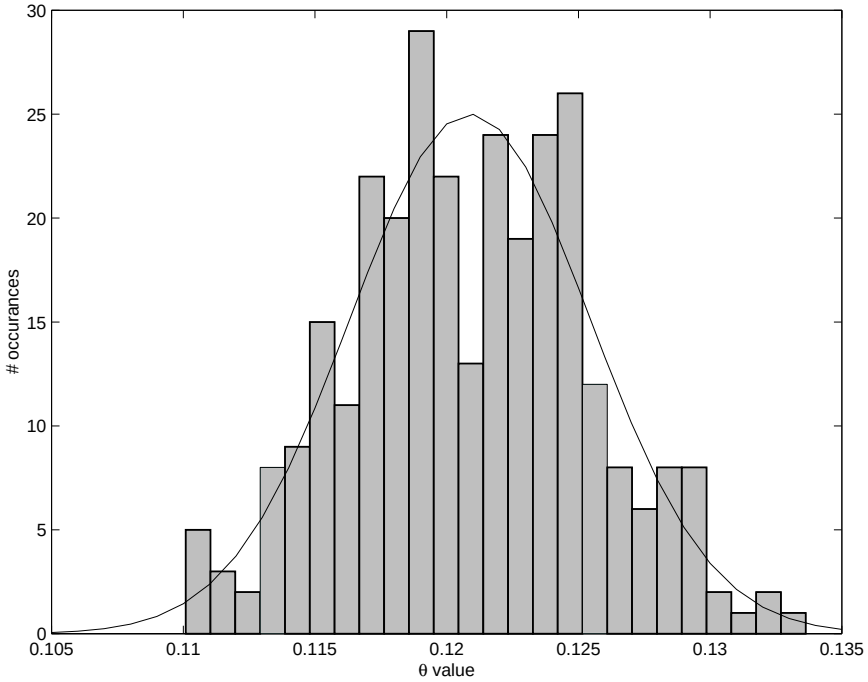

Figure 5.11: Histogram of θ values derived from each of the separate 300 simulations. The mean value of the distribution is 0.1209, with a standard deviation of 0.0046. The solid line represents a gaussian with this mean and standard deviation.

300 simulations are roughly distributed as a gaussian, and have a mean value equal 0.1209 with a standard deviation of 0.0046. Again, this is in good agreement with our former averaging scheme and published results.

5.4.2 Modeling of the quasi-random encoding scheme

We created a numerical model of the NMR quasi-random encoding scheme, which we then used with the diffusion simulator and persistence analysis code to test and verify the feasibility of the NMR experiment. There were numerous inputs to the model, including (in no particular order):

(i) cell length

(ii) imaging resolution

(iii) maximum magnetic field gradient available

(iv) number of (and/or) magnitude of encoding gradients for the quasi-random encoding scheme

(v) encoding gradient pulse duration

(vi) a list of RF flip angles $[\alpha_i]$ to use during quasi-random encoding

(vii) diffusion coefficient

(viii) Larmor frequency of NMR nuclei

The primary role of the NMR model was to create the quasi-random initial configuration; the diffusion simulator would then take this configuration and evolve it in time. The output consists of a history of sign changes in the ensemble and from this data we determine the "amount" of persistence that occurred. The algorithm for the NMR model is as follows:

(1) initialize a 2D magnetization array; one dimension denotes spatial position while the other represents the 3 orthogonal magnetization components M_x, M_y, and M_z. Set $(M_x = 0, M_y = 0, M_z = 1)$ for all positions;

(2) model the RF pulse α_i by mixing M_x, M_y, and M_z using eq. 5.2;

(3) model the gradient pulse of strength g_i by determining the spatial phase that each position accumulates due to the gradient pulse;

(4) mix M_x and M_y so that they accumulate the phase calculated in the previous step appropriate to their position;

(5) loop back to step (2), until steps 2–4 have been executed m times (where m specifies the number of encoding gradients to use);

(6) simulate a $\pi/2$ (storage) pulse.

The resulting configuration in the M_z portion of the magnetization array represents the initial conditions for the NMR persistence experiment, and is used as the input for the diffusion simulator. Analysis proceeds as before.

There are several factors missing from the NMR model. First, we did not incorporate diffusion into the model; in effect, we set $D = 0$ while generating the quasi-random configuration array, and then turn diffusion back on when going through the diffusion simulator. However, since the encoding gradients are pulsed for only 1 ms and the RF pulses themselves last only ~ 10 μs, the total encoding scheme takes less than 10 ms to execute. This is less than 10% of the diffusion time ($(\Delta x)^2/D \sim 0.125$ sec) across an imaging pixel (~ 0.05 cm) in a 3 atm xenon cell, and thus is not an effect that should skew our results. Another factor we did not model is the effect of random noise, especially with respect to our ability to image the magnetization at different times. Random noise is expected to cause erroneous sign changes in the imaging, thus making the magnetization appear to "persist" less than it does in reality, which could be manifested by a larger value for θ. Rather than investigate this in our simulations, we examined our experimental data for the effect that noise (or rather, *signal-to-noise*) had on our analysis (see section 5.5). Finally, we did not incorporate into this model the effect of RF coil inhomogeneity, which would result in spatial variations in both the flip angle and detection sensitivity. Our NMR coil ("X-2") was designed for high B_1 homogeneity and measurements indicate that variations in B_1 across the length of the cell were less than 5%, which we estimate is insignificant for the current persistence measurement (see appendix A).

How quasi-random is random enough?

Though somewhat idealized, the NMR model allows us to investigate some fundamental questions about the design of the experiment. In particular, we used the NMR model to verify our earlier analysis (see section 5.3.2) concerning the degree to which we could generate a quasi-random configuration. Practically, we address

the question, "how many encoding gradients are required?"

In section 5.3.2, we claimed that using m=6–8 encoding gradients of random magnitude were suitable for creating the desired quasi-random initial configuration. Using our numerical model and simulator, we were able to show that this assessment is correct. Figure 5.12 shows a plot of the -("mean slope") from a distribution of linear fits of $\log(p(t))$ vs. $\log(t)$ as a function of m. If the initial configuration is sufficiently (quasi)random, we expect that for the simulation parameters used, the -(mean slope) will approach the 1-D diffusion persistence exponent 0.12 with a standard deviation[9] of ~ 0.033. For $m < 6$, we see that both the mean slope and standard deviation of the distribution do not fit our expectations; however, for $m \geq 6$, the expected standard deviation and mean slope appear, showing that the system is sufficiently random to exhibit persistence behavior. Also, the mean slope appears to be insensitive to the value of $m \geq 6$, and from this, one could deduce that using $m = 9$ or 10 would be acceptable; however, doing so would reduce the mean absolute magnetization in the sample, and thus degrade SNR. Of course, we do not see any such problem in these noiseless simulations, but practically it becomes an issue and we chose to avoid using such large m values in the actual experiment.

Effect of finite data set

Given that m=6–8 creates a sufficient random initial configuration, we next used the NMR model and diffusion simulator to evaluate the effect of different data block sizes. In particular, with the same simulation settings as listed in the caption of Fig. 5.12, we varied the number of data points used in the magnetization array (i.e.,

[9]This is a simple scaling from Fig. 5.11, where $\sigma = 0.0046$ is taken from 300 simulations of arrays with 10^4 points. On the other hand, each data point shown in Fig. 5.12 is taken from 100 simulations of a 2000 point array; furthermore, only ~ 570 of those 2000 points contribute to the persistence simulation, since we assumed a 9 cm long cell and an imaging FOV (field of view) of 31.5 cm.

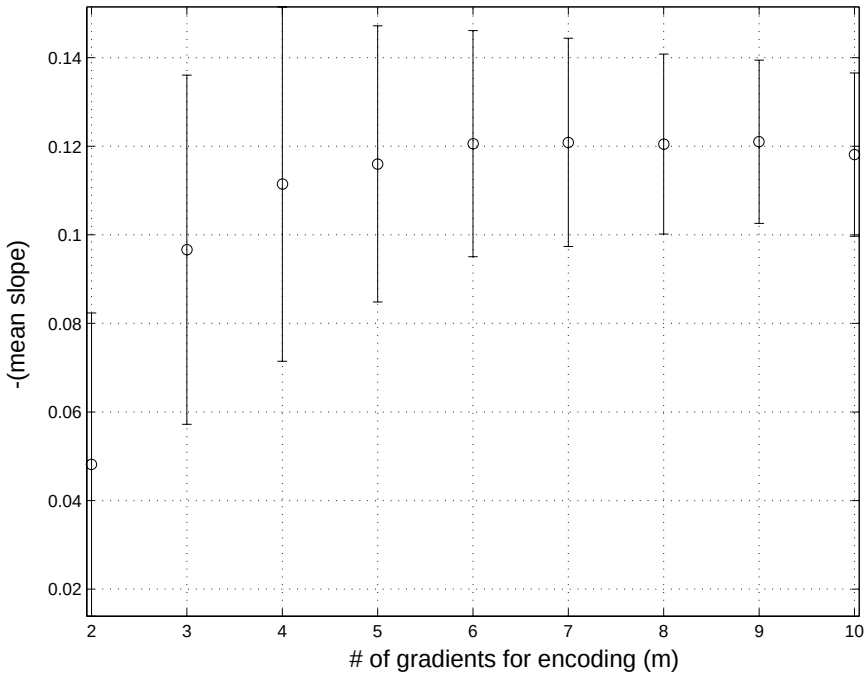

Figure 5.12: Persistence exponent θ derived from simulated data with variable m quasi-random initial configurations. m denotes the number of random-magnitude encoding gradients used. For these simulations, we set $D = 0.0198$ cm^2/s, field of view = 31.5 cm, cell length = 9 cm, number of data points = 2000. 100 different simulation runs (each with random encoding gradient magnitudes $[g_i]$) were completed for each m value. For every individual simulation, $p(t)$ was determined and the slope of a linear least squares fit of $\log(p(t))$ vs. $\log(t)$ was found. Thus, we obtained a distribution of 100 slopes for each m value. If the ensembles created with a given m are random enough for persistence to occur, their distribution of slopes from the linear fit should have a mean to equal $-\theta(\sim -0.12)$ and a standard deviation $\sigma \sim 0.033$ (which is scaled from the data shown in Fig. 5.11 - see text for detail). From the plot, this condition occurs when $m \geq 6$.

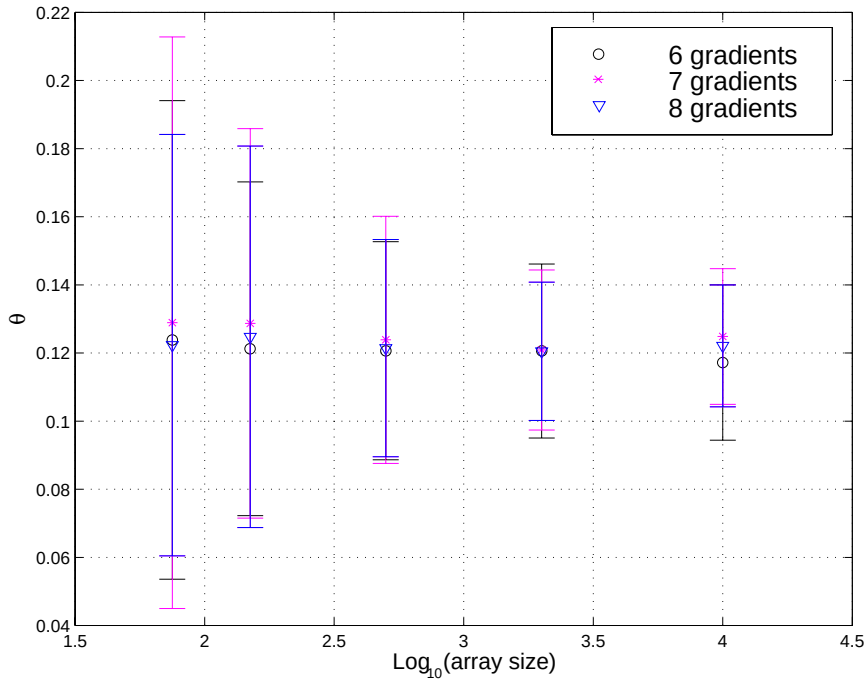

Figure 5.13: Average persistence exponent θ derived from simulated data with varying array sizes. 100 simulations with different random-magnitude encoding gradients were used to determine a mean θ value. The error bars represent the standard deviations of the θ distributions for the 100 simulations, and are proportional to the (array size)$^{-1/2}$. Results for $m = 6, 7, 8$ are shown, with no significant difference between them within the errors of the θ values.

[75 150 500 2000 10000] points). Figure 5.13 represents the mean θ for different data array sizes. For each array size, θ was derived from 100 different simulations (each with different random encoding gradient magnitudes). Unsurprisingly, θ does not change noticeably with array size, but the error bars do. In fact, the error bars simply decrease with array size in a familiar form: $\sigma \propto$ (array size)$^{-1/2}$.

5.5 Signal-to-Noise

As stated in our persistence paper (section 5.2/ref. [128]), we used images with signal-to-noise (SNR) ≥ 40 in our analysis; images with lower SNR were discarded because they yielded erroneous sign change events. In this final section we describe our procedure for filtering the data based on SNR, and justify the cutoff used.

To assign an SNR to each image, we examined the raw time domain echo data. We considered the "signal" as the peak amplitude of the absolute value of the (complex) echo data. "Noise" was calculated taking the mean of a signal-less region; i.e., in the wings of an NMR echo. See Figure 5.14 for an example of how SNR is determined.

In total, we conducted 59 experiments, each with a different quasi-random initial configuration. As specified in 5.2, we expected persistence behavior between 0.1 s$\lesssim t \lesssim$1 s (due to image resolution and finite size effects, respectively). To examine the effect of SNR on the analysis, we attempted to determine a persistence exponent θ from all the data that met a minimum SNR threshold. For low values of the SNR threshold, we found that θ thus derived was much larger than expected, which we attribute to erroneous sign changes arising from low SNR data (i.e., noisy data that made it appear that there were more sign changes occurring than were happening in reality, hence making our θ appear larger). As we increased the SNR threshold, we observed that θ decreased and then leveled off for a SNR threshold $\gtrsim 35$ (see Figure 5.15). We chose to use a more conservative threshold of 40 for the results quoted in the paper.

Similarly, we examined the domain growth exponent α (i.e., domain size $L \sim t^{\alpha}$) as a function of SNR threshold. Unsurprisingly, we found that for low SNR thresholds the domains appeared to grow less quickly (i.e., noise made domains

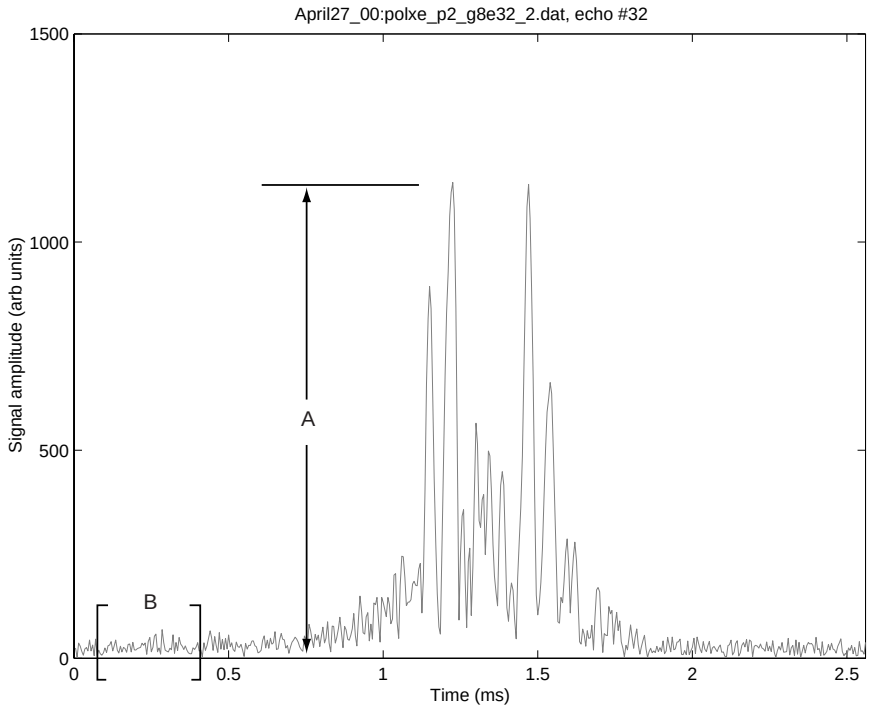

Figure 5.14: Time domain echo data illustrating the manner in which we calculated SNR. The plot shows the absolute value of the last NMR image (time domain echo) recorded from a persistence experiment. The maximum value, A, is taken as the "signal," while the noise is computed from the mean of region B. For this particular echo data, SNR ~ 42.

appear smaller) and hence resulted in smaller values of α; however, as the SNR threshold was increased, α also increased and reached a value of ~ 0.44 for all SNR thresholds $\gtrsim 30$.

Because the SNR threshold criteria was applied to each NMR echo, it was possible for some of the data from a given experiment to be excluded (usually from late times) while higher SNR echoes in the same experiment were retained in the analysis. However, in some cases only a few or none at all of the echoes from a given experiment met a given SNR threshold, thus effectively reducing the number of experiments on which the analysis was based. Hence, in our paper [128] we state that our results with SNR > 40 are derived from ~ 30 experiments, instead of the 59

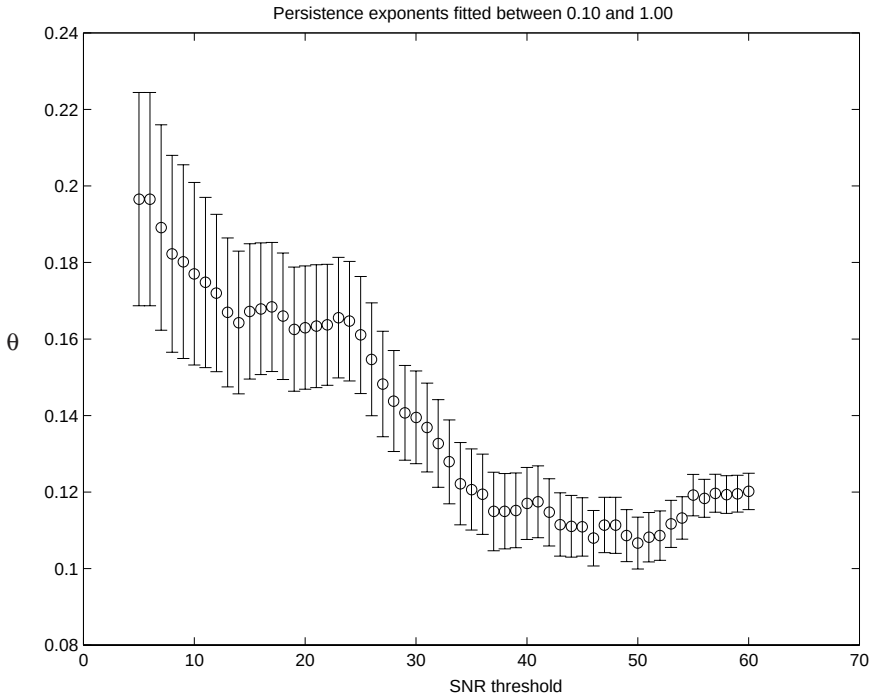

Figure 5.15: Plot of θ vs. SNR threshold, where θ is derived from all data with SNR $>$ (SNR threshold).

total experiments conducted. Roughly half of our experiments were found to have unacceptably low SNR, probably due to poor noble gas polarizations or excessively quasi-random initial configurations when using larger m values (i.e., 7 or 8).

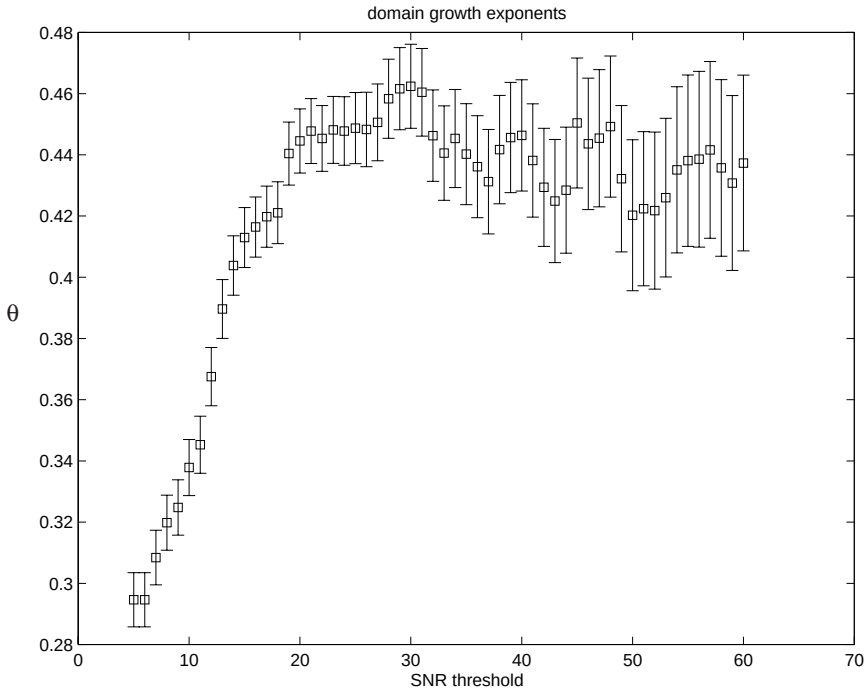

Figure 5.16: Plot of the domain growth exponent α as a function of SNR threshold. Similar to Fig. 5.15, α is derived from all data with SNR $>$ (SNR threshold).

Chapter 6

Low field ^{129}Xe relaxation measurements

This chapter describes ^{129}Xe relaxation experiments performed in OTS-coated[1] glass cells at low magnetic fields (< 70 G). Our goal was to determine whether the ^{1}H-^{129}Xe dipolar interaction (between OTS coating protons and the nuclei of ^{129}Xe adsorbed on the walls) was the dominant spin relaxation mechanism for laser-polarized ^{129}Xe in the OTS-coated cell. In SurfaSil-coated cells, Driehuys, Cates, and Happer [49] found that such a dipolar interaction was indeed the dominant ^{129}Xe relaxation mechanism. In their experiment, polarized ^{129}Xe is spin-locked to a weak rotating magnetic field $H_{1K} \sim 1.1$ G. By driving surface protons at increasing Rabi frequencies, they were able to decouple the ^{1}H-^{129}Xe interaction and observe a significant decrease of the ^{129}Xe relaxation rate. In a subsequent experiment [157], Sauer, Fitzgerald, and Happer successfully used a Hartmann-Hahn double-resonance technique [158] to *increase* the ^{129}Xe spin relaxation rate and thereby verify the dominant effect of the dipolar coupling of ^{129}Xe and ^{1}H in a SurfaSil-coated cell. In this ex-

[1] OTS=octadecyltrichlorosilane.

periment, the Rabi frequency (Ω_H) of surface protons was matched to the ^{129}Xe Larmor frequency (ω_{Xe}), i.e.,

$$\gamma_H B_1 = -\gamma_{Xe} B_0, \tag{6.1}$$

where B_1 denotes the strength of the magnetic field rotating at the ^{1}H Larmor frequency $\gamma_H B_0$, and B_0 is the magnitude of the main applied magnetic field (the minus sign arises from the opposite orientation of the ^{1}H and ^{129}Xe magnetic moments).

In the work presented here, we used this double resonance technique to characterize ^{1}H-^{129}Xe dipolar coupling in OTS-coated glass cells. We find that ^{1}H-^{129}Xe coupling is a minor contributor to ^{129}Xe spin relaxation in OTS-coated cells, as evidenced by a modest increase in the relaxation rate when the matching condition (eq. 6.1) is satisfied. In addition, the correlation time (i.e., the characteristic time of random fluctuations in the ^{1}H and ^{129}Xe dipolar interaction) that we derive from the resonance experiment is much greater than the correlation time we determine from B_0-dependent T_1 measurements, consistent with the conclusion that the dominant relaxation mechanism is not simply dipolar ^{129}Xe-^{1}H coupling. We list some of the possible candidates for this discrepancy and suggest ways to further investigate this issue.

These experiments were performed at the Center for Astrophysics using our home-built low field NMR system, with improvements and modifications made since the work reported in Chapter 4 (low field imaging). We begin with a summary of dipolar relaxation theory. Then we proceed to describe the relevant changes to the low field system, describe the double resonance technique we used, and present results obtained to date. The chapter concludes with a discussion of future studies.

6.1 Dipolar Relaxation

The dipole-dipole relaxation of unlike spins I and K has been treated in great detail by Abragam [70], with additional treatment by Sauer [159] in the case of a rotating magnetic field oscillating at one of the spin Larmor frequencies. Here we present the functional form of the dipolar relaxation rates (following Sauer's notation) and briefly describe the key assumptions used in deriving them with and without the rotating field.

The Hamiltonian $\mathcal{H}_1$ for the dipole-dipole coupling

$$\frac{3(\mu_K \cdot \hat{\mathbf{r}})(\mu_I \cdot \hat{\mathbf{r}})}{r^3} \tag{6.2}$$

can be expressed as a sum of products between spatial functions $F^{(q)}(t)$ and spin dependent functions $A^{(q)}$, i.e.,

$$\mathcal{H}_1 = \sum_q F^{(q)}(t) A^{(q)}, \tag{6.3}$$

where

$$F^{(0)} = \frac{1 - 3\cos^2\theta}{r^3}, \quad F^{(1)} = \frac{\sin\theta\cos\theta e^{-i\phi}}{r^3}, \quad F^{(2)} = \frac{\sin^2\theta e^{-2i\phi}}{r^3} \tag{6.4}$$

$$\begin{aligned} A^{(0)} &= \alpha\left[-\frac{2}{3}K_z I_z + \frac{1}{6}(K_+ I_- + K_- I_+)\right], \\ A^{(1)} &= \alpha\left[K_z I_+ + K_+ I_z\right], \\ A^{(2)} &= \frac{\alpha}{2} K_+ I_+ \end{aligned} \tag{6.5}$$

and $\alpha = -\frac{3}{2}\gamma_K\gamma_I\hbar$. Important assumptions made when determining the relaxation rate are that *(i)* the orientation vector $\mathbf{r}$ undergoes isotropic random motion, and

(ii) the reduced temporal correlation functions of $F^{(q)}$ are the same for all q and vary as $e^{-\tau/\tau_c}$, where τ_c is the correlation time. This last point is responsible for the frequency dependent lorentzian line shape of the relaxation rate (see eq. 6.6 and 6.9 below).

It is straightforward to solve for $\frac{d\langle K(t)\rangle}{dt}$, which is linear in $\frac{(\langle K(t)\rangle - K_0)}{T_1}$ (e.g., see [49,70,159]). One can show that the relaxation rate due to dipolar-coupling between I and K spins is given by

$$\frac{1}{T_1} = \frac{1}{10T_0}\left(\frac{1}{1+(\omega_{0K}-\omega_{0I})^2\tau_c^2} + \frac{3}{1+\omega_{0K}^2\tau_c^2} + \frac{6}{1+(\omega_{0K}+\omega_{0I})^2\tau_c^2}\right). \tag{6.6}$$

ω_{0K} and ω_{0I} are the Larmor frequencies of the K and I spins, respectively, and the zero field relaxation rate $1/T_0$ is given by

$$\frac{1}{T_0} = \frac{4}{3}I(I+1)\frac{\gamma_K^2\gamma_I^2\hbar^2}{r^6}\tau_c. \tag{6.7}$$

Next, consider an applied rotating magnetic field at the Larmor frequency of the I spins ($B_1(\omega_{0I})$), which leads to an interaction Hamiltonian

$$\mathcal{H}_{rot} = \hbar\omega_{1I}\left(I_x\cos\omega_{0I}t + I_y\sin\omega_{0I}t\right), \tag{6.8}$$

where $\omega_{1I} = \gamma_I B_1(\omega_{0I})$ is the Rabi frequency of the I spins. Transforming into the doubly rotating frame[2], Sauer [159] derives an expression for the K spin relaxation rate $1/T_1$ as a function of the I spin Rabi frequency ω_{1I}:

[2]i.e., first transforming into the frame of the unperturbed Hamiltonian $\mathcal{H}_0 = \hbar(\omega_{0K}K_z + \omega_{0I}I_z)$, and then into the frame of the Rabi oscillation, $\mathcal{H}_{rot}$.

$$\frac{1}{T_1} = \frac{1}{40T_0}\left[\frac{6}{1+(\omega_{1I}+\omega_{0K})^2\tau_c^2} + \frac{6}{1+(\omega_{1I}-\omega_{0K})^2\tau_c^2} + \frac{12}{1+(\omega_{0I}+\omega_{0K})^2\tau_c^2} + \frac{6}{1+(\omega_{0I}-\omega_{1I}+\omega_{0K})^2\tau_c^2} + \frac{6}{1+(\omega_{0I}+\omega_{1I}+\omega_{0K})^2\tau_c^2} + \frac{1}{1+(\omega_{0I}+\omega_{1I}-\omega_{0K})^2\tau_c^2} + \frac{2}{1+(\omega_{0I}-\omega_{0K})^2\tau_c^2} + \frac{1}{1+(\omega_{)i}-\omega_{1I}-\omega_{0K})^2\tau_c^2}\right]. \quad (6.9)$$

For ^{1}H-^{129}Xe coupling, the first resonance condition is met when the sum ($\omega_{1I} + \omega_{0K}$) goes to zero. This is equivalent to the matching condition mentioned earlier in eq. 6.1.

6.2 Experimental

Figure 6.1 illustrates the low field NMR configuration for the experiments described in this chapter. Using the same wire-wound solenoid as described in our low field imaging experiments, we constructed several current monitoring circuits and carefully oriented the solenoid with respect to the Earth's magnetic field. We tested the magnetic field stability by acquiring FIDs from a polarized ^{129}Xe cell at different times and recording the change in the ^{129}Xe Larmor frequency over time ($\sim$ 0.5 Hz drift over $\sim$ an hour at 60 kHz). Furthermore, when the magnet was properly shimmed we observed long ^{129}Xe transverse dephasing times ($T_2{}^* \sim$ 1–2 seconds). Thus, we improved the stability and homogeneity of the magnetic field by at least a factor of 2 as compared to the arrangement for our earlier low field imaging.

We also constructed a new detection and excitation coil setup that is specifically designed for dual frequency operation (i.e., for driving ^{1}H's and detecting ^{129}Xe NMR signals; see Fig. 6.5). The NMR experiment was controlled by an Apple Macintosh

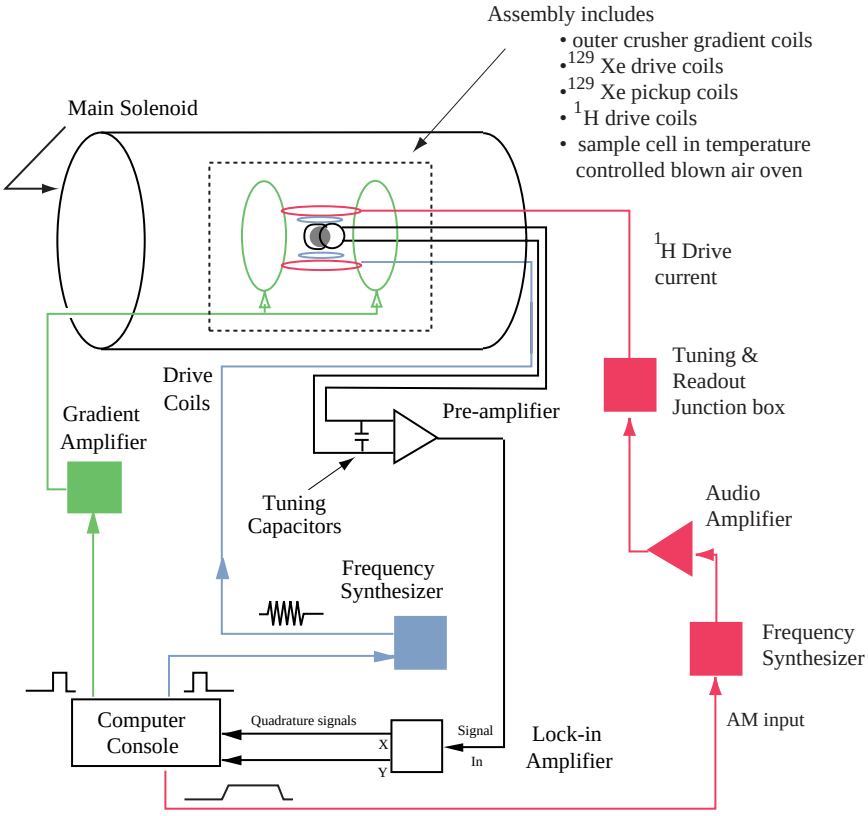

Figure 6.1: Low field NMR system block diagram. In contrast to the setup shown in Fig. 4.1, the setup shown here has no imaging gradients installed. Instead, another pair of RF coils (for driving ^{1}H at different Rabi frequencies) is in place.

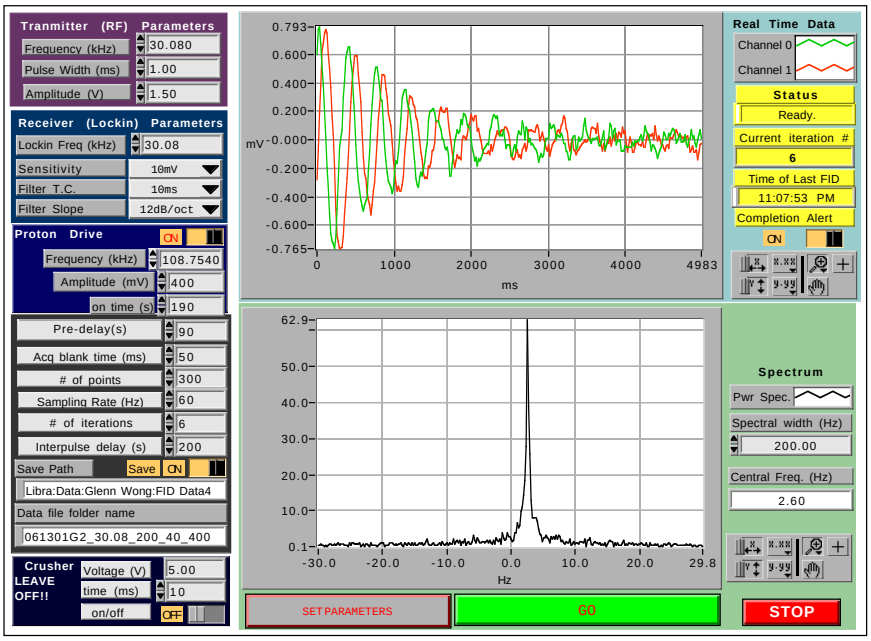

Figure 6.2: LabVIEW VI for experimental control and data collection. The lockin amplifier and two frequency synthesizers could be configured remotely from this VI, while two digital-to-analog outputs sent by the VI triggered RF pulses and ramped up/down the applied ^{1}H drive field. Acquisition parameters, including iterative control of the experiment, could also set from this VI. The two graphs on the right side of the VI show the components of the acquired FID and its power spectrum.

computer running LabVIEW[3] – in contrast to the commercial Bruker AMX console used in the low field imaging. Figure 6.2 shows the LabVIEW "virtual instrument" (VI) created for controlling the experiments.

To improve the stability and ease of control for the main magnetic field, we constructed current regulator circuits which allowed us to control the current supplied to the solenoid and shim coils. As we described in section 4.2.2, the original scheme powered the solenoid directly from two HP6200B DC power supplies that provided ~0.4 A to each of the four winding layers. Using a single HP6274B DC power supply with a simple current monitoring circuit (see Fig. 6.6), we achieved greater magnetic

[3]version 4, National Instruments, 6504 Bridge Point Parkway, Austin TX 78730.

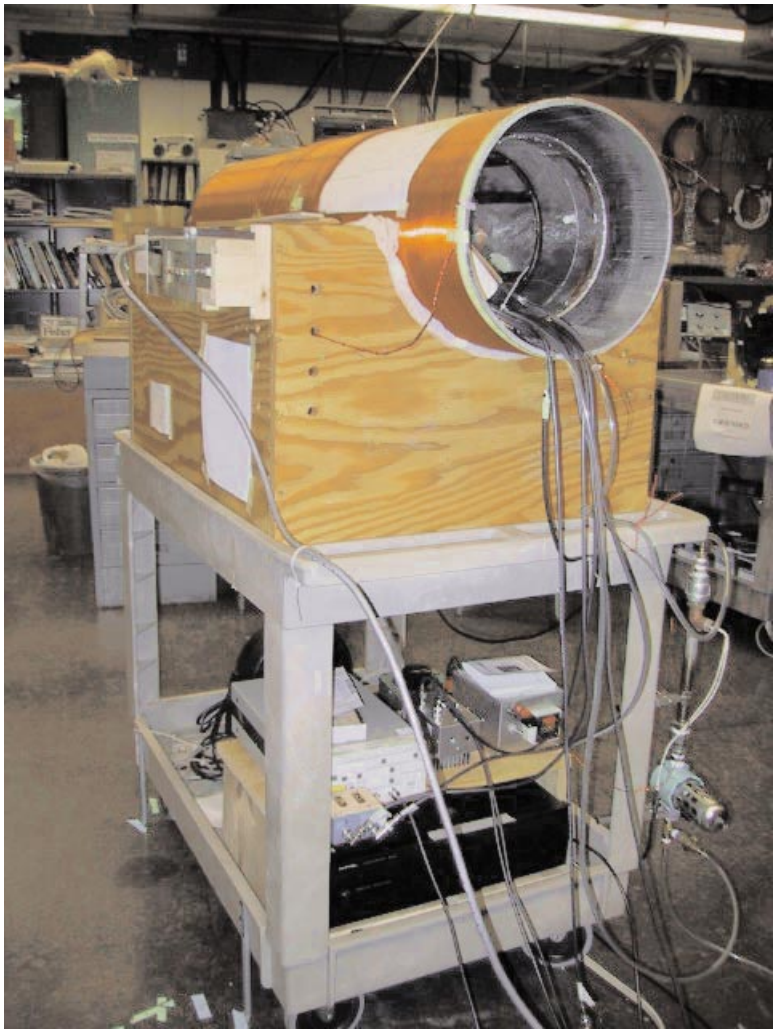

Figure 6.3: Photo of the low field solenoid and associated electronics. This is the same solenoid used for the low field imaging experiments described in Chapter 4 (see section 4.2.2). The pre-amplifier for the pickup coils, audio amplifier for the proton drive field, and the temperature controller for the cell holder are seated at the bottom of the cart.

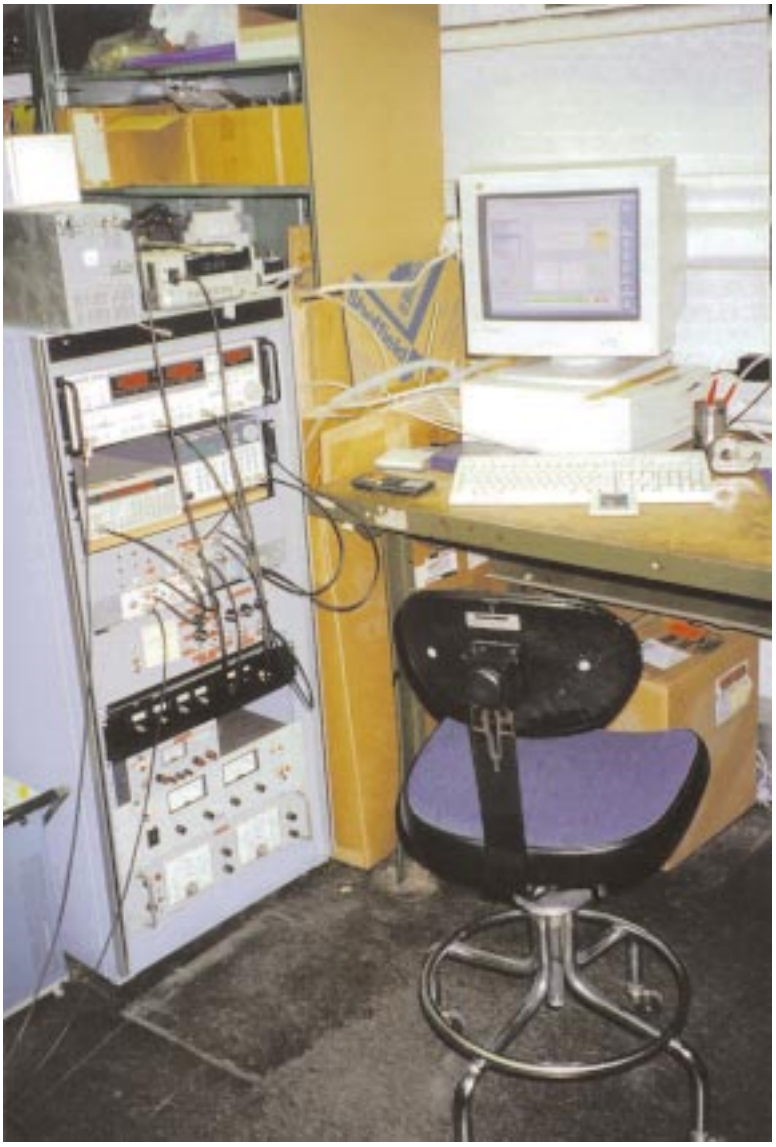

Figure 6.4: Photo of the low field instrumentation and computer console at the CfA.

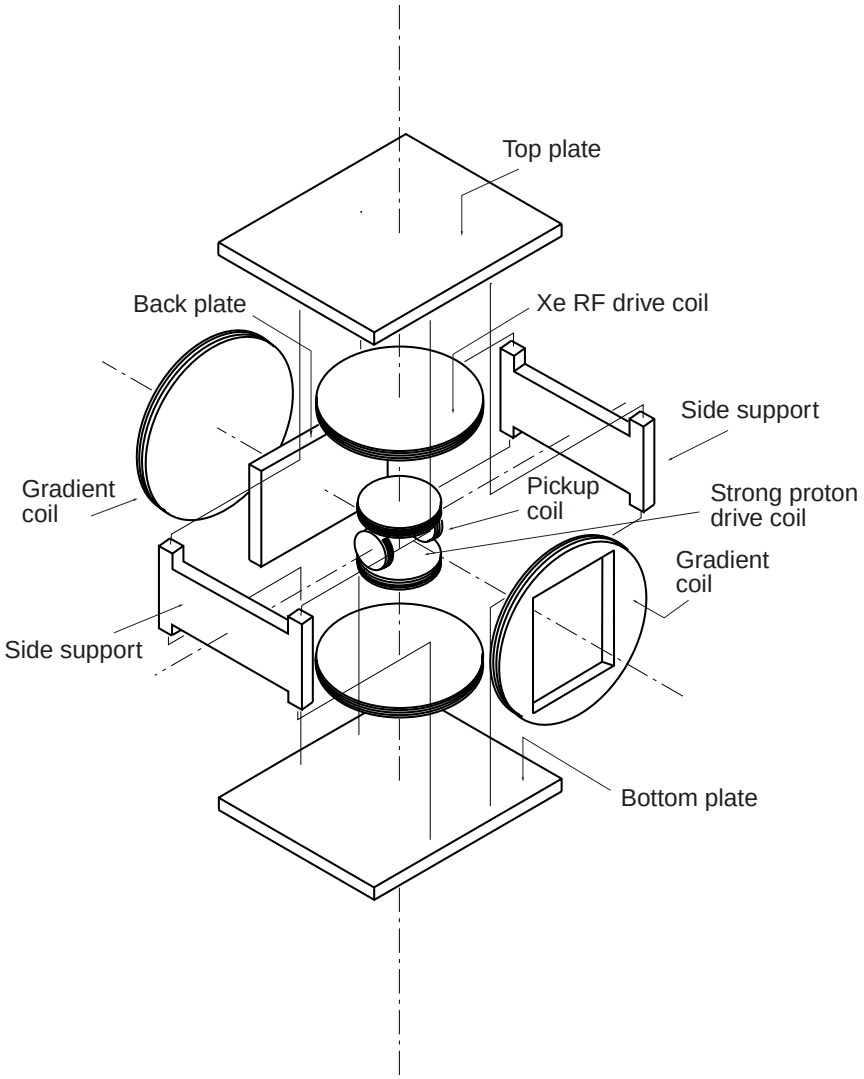

Figure 6.5: Low field pickup assembly drawing. Pickup coils for NMR detection were small to allow the closest proximity to the cell and each one was wound with approximately 150 turns of 32 gauge copper wire. Coils used to drive a strong oscillating field at the ^{1}H Larmor frequency were also fairly close to the cell in order to obtain a large B_1 with reasonable current. The xenon RF drive coils were made as large as possible to maximize the homogeneity of the flip angle inside the spherical cells.

fields (up to ∼70 G) with better stability than previously possible with the HP6200B supplies[4]. Furthermore, we oriented the axis of the solenoid perpendicular to the local magnetic field in the laboratory (see Fig. 6.7) which resulted in the longest T_2^* dephasing times observed.

Figure 6.8 illustrates the pulse sequence used for the double resonance ^{129}Xe relaxation measurements. This sequence is similar to the one for determining flip angles and T_1's (see Fig. 3.3). One difference is that instead of a crusher gradient pulse after FID acquisition, here we have a strong magnetic field applied for a time τ that is oscillating at the ^{1}H Larmor frequency. The ^{1}H Rabi frequency is directly proportional to the amplitude of the "^{1}H-drive," and was powered by a commercially available audio amplifier[5]. Flip angles and T_1 values were determined as described in Section 3.3.1.

As a final experimental note, we constructed a temperature controlled cell holder to maintain the ^{129}Xe cell at a constant temperature during a T_1 measurement (this was necessary because as Fig. 6.9 shows, the ^{129}Xe T_1 varies significantly with temperature in our OTS-coated cell). Compressed air was blown through the cell holder, which had an interior volume only slightly larger than a cell. A 100 Ω platinum RTD was placed inside the holder (without touching the walls or cell) to sense the temperature of the air, which could be heated by a cartridge heater placed upstream of the cell holder. Temperature monitoring and control was performed with an Omega CN8500 controller.

Our first step was to measure the ^{129}Xe relaxation rate as a function of the main

[4]Magnetic field stability was frequently better than 1 part in 10^5 over ∼ hour timescales, with significantly less transient warm-up drift than shown in Fig. 4.6. Short of incorporating active feedback from an *in situ* magnetometer, the field stability of this solenoid could probably be improved by better temperature regulation of the resistive elements (including the solenoid itself) in the current supply circuit.

[5]Model RB-981, Rotel of America, 54 Concord Street, North Reading, MA 01864-2699.

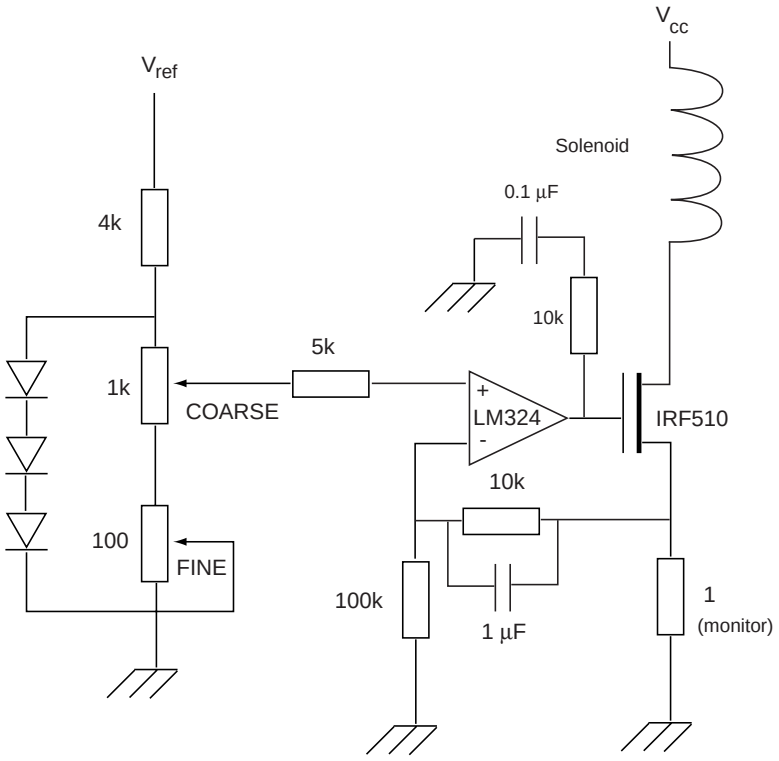

Figure 6.6: Schematic of the current regulator circuit. This circuit was used to control the current supplied to the main solenoid, and with slight modification was also used for the shim coils. The diodes and variable resistors used depended on the range of the output current desired (i.e., $\sim$100 mA for the shim coils and $\sim$1 A for the main solenoid). The voltage across the 1 Ω monitor resistor shown on the lower right is directly proportional to the current through the solenoid. For supplying current to the main solenoid, it was important to heat sink the IRF510 MOSFET and provide blown air to keep it cool. V_{ref} was provided by a REF01C precision voltage chip.

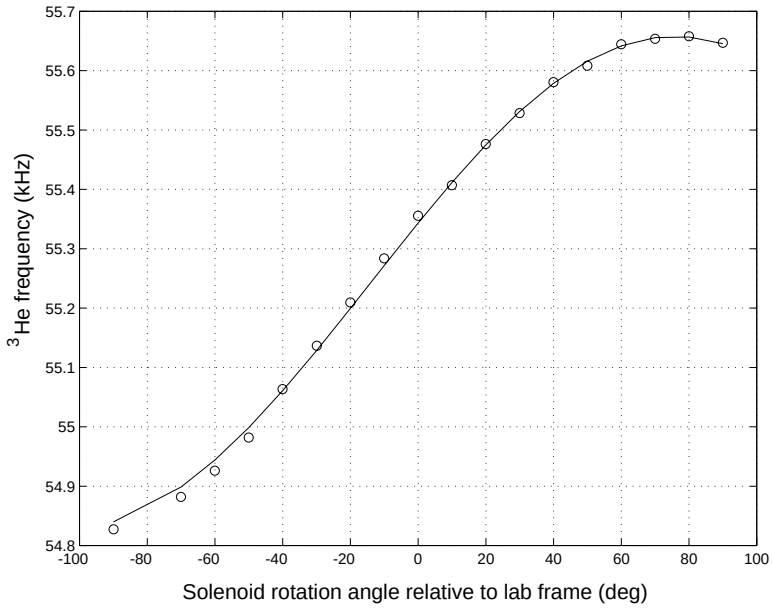

Figure 6.7: Rotational shimming of the solenoid. The solenoid was rotated in the laboratory through 180° in 10° increments, and at each position a ^{3}He free induction decay (FID) was acquired from a polarized ^{3}He cell (TS-2) centered in the solenoid. From the FID we could determine the ^{3}He Larmor frequency, which is plotted above as a function of rotation angle (∘). The frequency shifts reflect the change in orientation of the solenoid field ($\sim$ 17 G) relative to the component of the local Earth's magnetic field in the plane of the solenoid rotation. From this plot, we determined that the horizontal component of the Earth's field is $\sim$ 0.128 G. The solid line in the plot is a χ^2 (least squares) fit to the frequency data using a sine function with phase ϕ. χ^2 is minimized when $\phi = +14°$, thus indicating the direction of the Earth's magnetic field with respect to the laboratory. We have found that ${T_2}^*$ is optimized when the solenoid is oriented perpendicular to the Earth's magnetic field, and is therefore situated at an angle $\sim$ 14° relative to the lab "zero" (which runs across the width of PG-07).

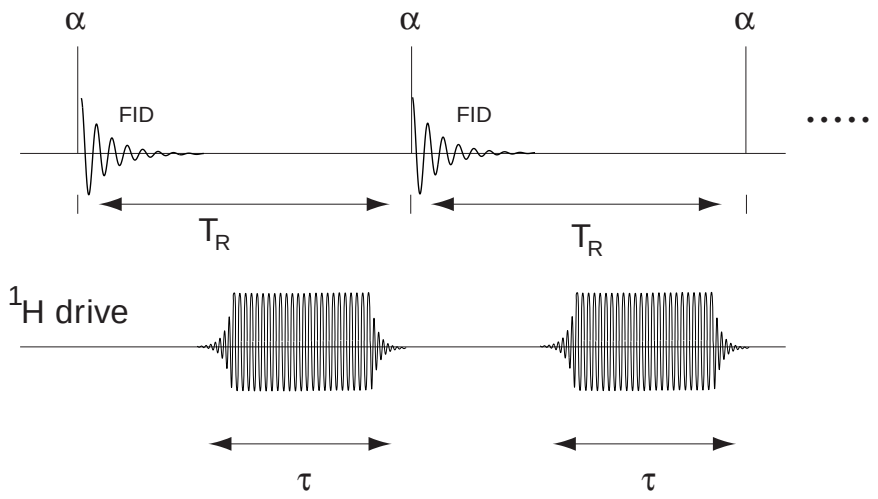

Figure 6.8: Pulse sequence for ^{129}Xe relaxation measurements with an applied ^{1}H RF oscillating field. The upper part shows RF excitation pulses (α) and FIDs at the ^{129}Xe Larmor frequency repeated at intervals T_R. A strong ^{1}H drive field is applied for time τ in the deadtime between α pulses. The amplitude of the ^{1}H drive field determines the ^{1}H Rabi frequency.

magnetic field B_0. This allows us to use eq. 6.6 to determine a correlation time τ_c of the ^{1}H-^{129}Xe coupling, if that is indeed the dominant relaxation mechanism. Once we have determined a representative τ_c, we chose a magnetic field such that $\omega_{0K}\tau_c > 1$. At such a field, the ^{1}H-^{129}Xe coupling should be reduced and effectively "turned off" because there will be no Fourier components of the fluctuating dipolar interaction at the ^{129}Xe Larmor frequency. We can then turn a portion of the ^{1}H-^{129}Xe coupling back "on" by driving the protons with a sufficiently strong rotating magnetic field such that its Rabi frequency matches the ^{129}Xe Larmor frequency. From eq. 6.9, we see that varying the ^{1}H Rabi frequency will result in a lorentzian resonance in the ^{129}Xe relaxation rate.

For these measurements, we used OTS-coated cell G-2, which contained ∼1 atm of 90% enriched ^{129}Xe ∼80 torr of N_2, and a small amount of rubidium.

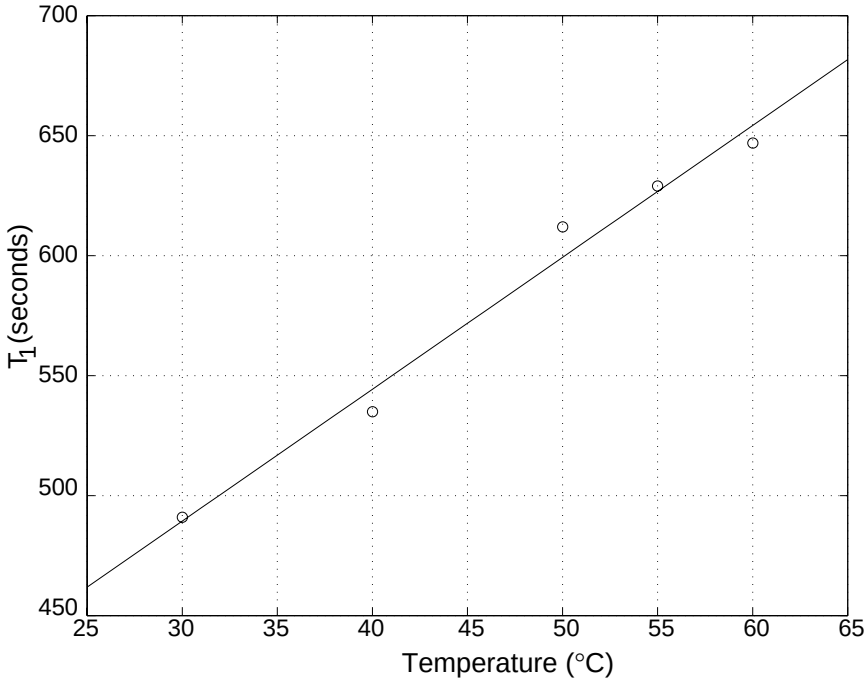

Figure 6.9: Temperature dependence of ^{129}XeT_1 at ∼17 G. Over a 30°C range the ^{129}Xe T_1 in OTS-coated cell G-2 varies by more than 25%. The line is a guide to the eye.

6.3 Results

Figure 6.10 shows the ^{129}Xe relaxation rate $1/T_1$ as a function of main magnetic field B_0. The data was poorly fit by a single function of the form of eq. 6.6. However, using a sum of two such expressions with different amplitudes and correlation times (plus a constant background), the fit was much better. In particular, we compared fits using one, two, and three correlation times, and calculated

$$F_\chi = \frac{\chi^2(m_1) - \chi^2(m_2)}{\chi^2(m)/(N - m_2)} = \frac{\Delta\chi}{\chi^2_\nu}, \tag{6.10}$$

which is the difference between χ^2's of two different fitting functions (with $m_1 < m_2$ number of terms) divided by the reduced χ^2 of the fit with m_2 terms (see Beving-

ton, section 11.4 [160]). Comparing the results to calculated F distribution tables (see Tables C.5 and C.6 of [160]), it was clear at least two correlation times were needed. However, adding a third correlation time to the fit yielded a value of $F_\chi \sim 0$, indicating that two correlation times were sufficient to fit the data. Similarly, both Driehuys *et al.* [49] and Sauer *et al.* [157] found that using two correlation times gave the most reasonable fit to their measurements. Sauer determined that the two correlation times were 9.3 ± 0.6 μs and 0.6 ± 0.2 μs for ^{129}Xe in their SurfaSil-coated cell at 250 K (in agreement with Driehuys' earlier work). In contrast, we find $\tau_{c1} = 28.1 \pm 2.5$ μs and $\tau_{c2} = 1.04 \pm 0.02$ μs for ^{129}Xe relaxation data in an OTS-coated cell (G-2) at 40°C. The amplitude of the expression with τ_{c2} is about twice that of the expression with τ_{c1}.

We measured the ^{129}Xe relaxation rate at 25.535 G as a function of ^{1}H Rabi frequency. Assuming $\tau_c = 28\mu$s, $\omega_{0K}\tau_c > 1$ at this main magnetic field strength. When we applied an increasing strength rotating magnetic field at the ^{1}H Larmor frequency, we observed a resonance peak at the point where the matching condition eq. 6.1 is fulfilled (see Fig. 6.11). However, the extracted correlation time from this data ($\tau_c = 197 \pm 49$ μs) is significantly different from the 28 μs found in the field-dependent T_1 measurement. Furthermore, the ^{129}Xe relaxation rate continues to increase with increasing ^{1}H Rabi frequency (see Fig. 6.11).

6.4 Discussion

In contrast to the experiments performed by Driehuys *et al.* [49] and Sauer *et al.* [157] for SurfaSil-coated cells, we conclude that ^{1}H-^{129}Xe coupling is *not* the dominant relaxation mechanism in our OTS-coated cell. Specifically, when matching the ^{1}H Rabi frequency to the ^{129}Xe Larmor frequency, we observed a small enhancement of

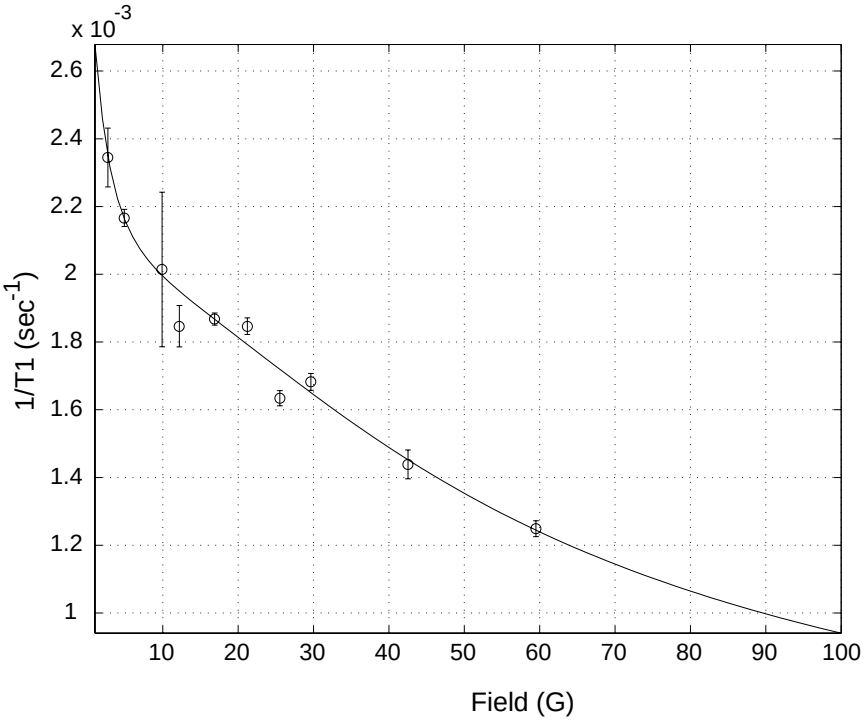

Figure 6.10: ^{129}Xe T_1 in an OTS-coated cell as a function of applied magnetic field B_0. The solid line is a fit using a sum of two expressions of the form of eq. 6.6, each with an independent amplitude and τ_c (see text). All measurements shown were made at 40°C.

the ^{129}Xe relaxation rate, indicating that the ^{1}H-^{129}Xe coupling is a modest contributor to ^{129}Xe relaxation. It may be worth noting here that the low magnetic field ^{129}Xe relaxation rates in our cell are approximately four times faster than the rates reported in Sauer's SurfaSil-coated cell; however, at high fields (∼1 T) the difference between ^{129}Xe relaxation rates in OTS and SurfaSil-coated cells is small.

The mismatch of correlation times determined from the field dependent ^{129}Xe T_1 measurements and the double resonance technique τ_c suggests that the former is unlikely to be the result of pure ^{1}H-^{129}Xe dipolar coupling, and either involves a more complex interaction between ^{129}Xe and ^{1}H, or impurities in the coating or glass. For example, Saam and coworkers very recently identified ferromagnetism in

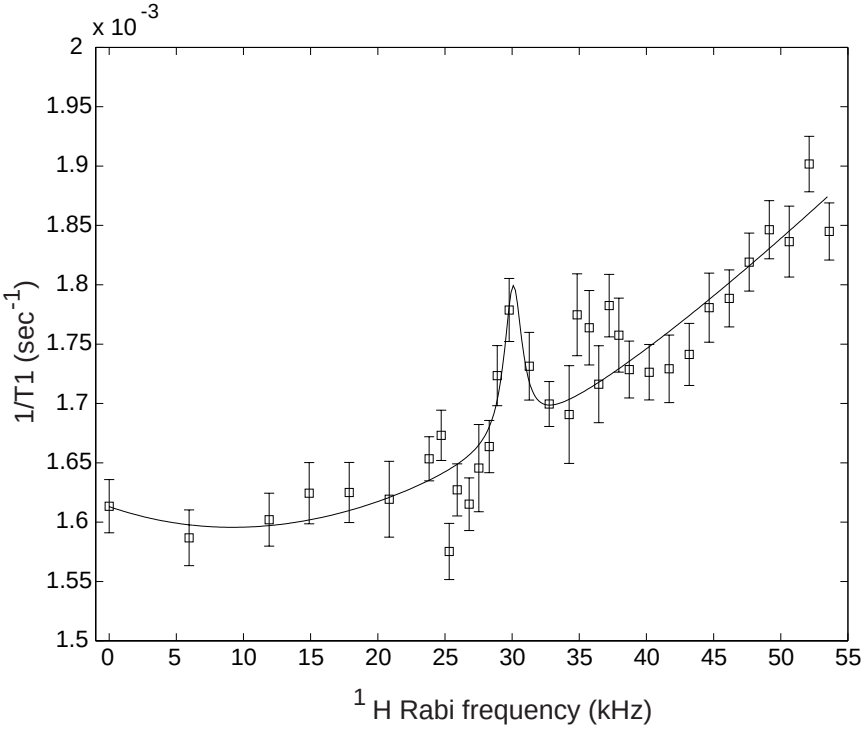

Figure 6.11: ^{129}Xe relaxation rate at 25.535 G as a function of ^{1}H Rabi frequency. The line shown is a fit to the data of a sum of eq. 6.9 and a polynomial (cubic) background. The strength of the Rabi frequency was calibrated by using a small pickup loop and measuring the induced *EMF* by the ^{1}H-drive coils. This calibration resulted in an x-axis scale with about 10% accuracy and was close to what is shown here. In this figure, we have assumed that the peak is exactly on resonance (i.e., $\gamma_H B_1 = -\gamma_{Xe} B_0$), and the x-axis is scaled accordingly. The least-squares fit yields a value of $\tau_c = 197 \pm 49 \mu$s.

glass cells as a previously unrecognized source of ^{3}He nuclear spin relaxation [161]. This ferromagnetism is a function of the cell's past exposure to high magnetic fields, and is reversible with a standard "de-Gaussing" procedure. It is possible that such cell ferromagnetism has played a role in our ^{129}Xe relaxation experiments. In fact, preliminary data indicates that this is certainly an interesting point to investigate. We recently noticed that after placing our OTS-coated ^{129}Xe cell (G-2) briefly in the bore of a high field 4.7 T magnet (for about a minute), the measured ^{129}Xe T_1 back at 25.535 G *decreased* by $\sim$ 100 s ($\sim$ 17% decrease in ^{129}Xe T_1). Attempts to degauss the cell improved the ^{129}Xe T_1, but only by 40–50 s.

It is clear that further studies of ^{129}Xe relaxation in OTS-coated cells are needed. To begin with, it would be useful to make many more cells and test for repeatability. Having said that, a few other cells of similar quality were made and exhibited similar ^{129}Xe T_1's at low fields to the G-2 cell. Also, it would be interesting to continue ^{129}Xe relaxation rate measurements with increasing ^{1}H Rabi frequencies; Fig. 6.11 does not extend past a ^{1}H Rabi frequency of 55 kHz because that is the limit of the present amplifiers in use. However, should another resonance peak be observed at a greater ^{1}H Rabi frequency, it would shed light on the appropriate interaction expression between ^{129}Xe and ^{1}H. It would also be helpful to repeat these experiments at different temperatures in the OTS-coated cell to see if the variation of ^{129}Xe relaxation rate is indicative of the ^{129}Xe dwell time on the coating surface. Finally, there is certainly a strong possibility of ferromagnetism in our glass cell, and investigating this point may yield some very important insights concerning the relaxation mechanisms which limit ^{129}Xe T_1 in glass cells.

Appendix A

RF solenoid coil design: minimizing field variance

This appendix presents an analytical calculation for determining the optimal winding of an RF solenoid coil by minimizing the variance in its axial field. Constraints include: *(i)* the winding must be made from a single conductor (no composite windings)[1], and *(ii)* the winding cannot double back on itself (i.e., winding should be consistent in its helical sense).

Using the law of Biot-Savart, an expression is derived for the axial solenoid field where the pitch of the winding is allowed to vary as a polynomial. By examining an expression for the variance of this field from the mean, one can numerically determine the coefficients of the winding polynomial.

Special thanks to Patrick Ledden for insightful conversations.

[1]This constraint exists because at high frequencies (tens of MHz), the inductance and self-capacitance of composite windings limit the achievable resonance frequency of the coil.

A.1 Definitions

We begin by defining position $\mathbf{l}$ along the conductor path in cartesian coordinates; it is easily parameterized by ϕ and z

$$\mathbf{l} = (R\cos(\phi), R\sin(\phi), z)$$

where $\phi = \phi(z)$, $R =$ coil radius. Thus, we can write

$$d\mathbf{l} = (-R\sin(\phi)\phi', R\cos(\phi)\phi', 1)$$

where $\phi' = d\phi/dz$. Recall that the law of Biot-Savart is

$$d\mathbf{B} = \frac{Id\mathbf{l} \times \mathbf{r}}{cr^3} \tag{A.1}$$

Assume we want to look at $\mathbf{B}$ along the z-axis; denote the observation point $\mathbf{r}' = (0, 0, z')$. The displacement vector $\mathbf{r}$ is then given by

$$\mathbf{r} = \mathbf{l} - \mathbf{r}' = (R\cos(\phi), R\sin(\phi), z - z')$$

Using these expressions, we can now write equation [A.1] in cartesian coordinates:

$$\begin{aligned} d\mathbf{B} &= \frac{I}{c[R^2 + (z-z')^2]^{3/2}} \begin{vmatrix} \hat{\mathbf{i}} & \hat{\mathbf{j}} & \hat{\mathbf{k}} \\ -R\phi'\sin(\phi) & R\phi'\cos(\phi) & 1 \\ R\cos(\phi) & R\sin(\phi) & z-z' \end{vmatrix} \\ &= \frac{I}{c[R^2 + (z-z')^2]^{3/2}} \begin{pmatrix} (\phi' R\cos(\phi)(z-z') - R\sin(\phi))\hat{\mathbf{i}} \\ +(R\phi'(z-z')\sin(\phi) + R\cos(\phi))\hat{\mathbf{j}} \\ +(-R^2\phi'\sin^2(\phi) - R^2\phi'\cos^2(\phi)))\hat{\mathbf{k}} \end{pmatrix} \end{aligned}$$

$$= \frac{IR}{c[R^2+(z-z')^2]^{3/2}} \begin{pmatrix} (\phi' \cos(\phi)(z-z') - \sin(\phi))\hat{\mathbf{i}} \\ +(\phi'(z-z')\sin(\phi) + \cos(\phi))\hat{\mathbf{j}} \\ -(R\phi')\hat{\mathbf{k}} \end{pmatrix} \tag{A.2}$$

The z-component of the field, $B_z(\mathbf{r}')$, can be written as follows:

$$\begin{aligned} B_z(\mathbf{r}') &= \int d\mathbf{B} \cdot \hat{\mathbf{k}} \\ &= \frac{IR}{c} \int_{-L/2}^{+L/2} \frac{-R\phi' dz}{[R^2+(z-z')^2]^{3/2}} \end{aligned} \tag{A.3}$$

for a coil of length L.

The problem now is to find a suitable function for $\phi(z)$ which will optimize the field profile $B_{z'}(\mathbf{r}')$. For a regularly wound solenoid, $\phi(z) = \gamma z$, where γ is a constant in units [radians/unit distance]. It is therefore reasonable to "tweak" $\phi(z)$ by adding higher order terms. In particular, because we should not have the coil wind back on itself, only *odd* powers are acceptable. *(Note that $B_z(\mathbf{r}')$ is an even integral of [$\phi' \times$ (even function)], and thus ϕ must be an odd function of z)*

If we define $\phi(z)$ as

$$\phi(z) = \frac{\alpha}{5}z^5 + \frac{\beta}{3}z^3 + \gamma z \tag{A.4}$$

then we have

$$\phi'(z) = \alpha z^4 + \beta z^2 + \gamma \tag{A.5}$$

using Eqn [A.5] in Eqn [A.3], and factoring out constant terms, we can write:

$$B_z(z') \propto \mathcal{F}(z') \tag{A.6}$$

$$\begin{aligned}\mathcal{F}(z') &\equiv \int_{-L/2}^{L/2} \frac{\alpha z^4 + \beta z^2 + \gamma}{[R^2 + (z - z')^2]^{3/2}} dz \\ &= \alpha \mathcal{F}_1(z') + \beta \mathcal{F}_2(z') + \gamma \mathcal{F}_3(z') \end{aligned} \tag{A.7}$$

where we have made the following definitions:

$$\begin{aligned}\mathcal{F}_1(z') &\equiv \int_{-L/2}^{L/2} \frac{z^4 dz}{[R^2 + (z - z')^2]^{3/2}} \\ \mathcal{F}_2(z') &\equiv \int_{-L/2}^{L/2} \frac{z^2 dz}{[R^2 + (z - z')^2]^{3/2}} \\ \mathcal{F}_3(z') &\equiv \int_{-L/2}^{L/2} \frac{dz}{[R^2 + (z - z')^2]^{3/2}} \end{aligned} \tag{A.8}$$

A.2 Selection Criteria

A reasonable selection criteria to use is the variance σ of the axial field $B_z(z')$ along the axis away from its mean value, $\langle B_z \rangle$, along some length of the axis L'. Note that, while L' can be set equal to the coil length L, it is more general to allow L' to be an independent variable, and may be chosen to reflect the length over which a homogeneous field is desired (*e.g., the length of the sample*). In particular, let us define σ as follows:

$$\begin{aligned}\sigma &= \langle (B_z(z') - \langle B_z \rangle)^2 \rangle \\ &= \frac{1}{L'} \int_{-L'/2}^{L'/2} [B_z(z') - \langle B_z \rangle]^2 dz' \end{aligned} \tag{A.9}$$

Since we have $B_z(z') \propto \mathcal{F}(z')$ (see Eqn [A.6]), we can use a variance σ':

$$\sigma' = \frac{1}{L'} \int_{-L'/2}^{L'/2} [\mathcal{F}(z') - \langle \mathcal{F} \rangle]^2 dz' \tag{A.10}$$

We can write the average field over the length L' as

$$\begin{aligned}\langle \mathcal{F} \rangle &= \frac{1}{L'} \int_{-L'/2}^{L'/2} \mathcal{F}(z) dz \\ &= \frac{1}{L'} \left(\alpha \int_{-L'/2}^{L'/2} \mathcal{F}_1(z) dz + \beta \int_{-L'/2}^{L'/2} \mathcal{F}_2(z) dz + \gamma \int_{-L'/2}^{L'/2} \mathcal{F}_3(z) dz \right) \\ &\equiv \frac{1}{L'} (\alpha I_1 + \beta I_2 + \gamma I_3) \end{aligned} \tag{A.11}$$

Putting together Eqns [A.10] and [A.11], we can write σ' as

$$\begin{aligned}\sigma' &= \frac{1}{L'} \int_{-L/2}^{L/2} \left(\alpha \mathcal{F}_1(z') + \beta \mathcal{F}_2(z') + \gamma \mathcal{F}_3(z') - \frac{1}{L'} (\alpha I_1 + \beta I_2 + \gamma I_3) \right)^2 dz' \\ &= \frac{1}{L'} \int_{-L'/2}^{L'/2} \left(\alpha (\mathcal{F}_1(z') - \frac{I_1}{L'}) + \beta (\mathcal{F}_2(z') - \frac{I_2}{L'}) + \gamma (\mathcal{F}_3(z') - \frac{I_3}{L'}) \right)^2 dz' \end{aligned} \tag{A.12}$$

We proceed by assuming that γ is given; this is not unreasonable, and shows that we have some baseline (linear) coil winding parameter in mind. α and β are the coefficients for the higher order corrections, and will naturally depend on the value of γ chosen. Thus, in order to reach an extrema of σ' (i.e., a minima), the partial derivatives of σ' with respect to α and β must go to zero:

$$\frac{\partial \sigma'}{\partial \alpha} = 0$$

and

$$\frac{\partial \sigma'}{\partial \beta} = 0 \tag{A.13}$$

Taking the partial derivatives of Eqn [A.12] with respect to α, we have:

$$\begin{aligned}\frac{\partial\sigma'}{\partial\alpha} &= \frac{2}{L'}\int_{-L'/2}^{L'/2}\left(\alpha(\mathcal{F}_1(z')-\frac{I_1}{L'})+\beta(\mathcal{F}_2(z')-\frac{I_2}{L'})+\gamma(\mathcal{F}_3(z')-\frac{I_3}{L'})\right)\times \\ &\qquad\qquad (\mathcal{F}_1(z')-\frac{I_1}{L'})dz' \\ &= \alpha a_1+\beta b_1+\gamma c_1 \end{aligned} \tag{A.14}$$

where we have define a_1, b_1, and c_1 as

$$\begin{aligned} a_1 &\equiv \int_{-L'/2}^{L'/2}\left(\mathcal{F}_1(z')-\frac{I_1}{L'}\right)^2 dz' \\ b_1 &\equiv \int_{-L'/2}^{L'/2}(\mathcal{F}_2(z')-\frac{I_2}{L'})(\mathcal{F}_1(z')-\frac{I_1}{L'})dz' \\ c_1 &\equiv \int_{-L'/2}^{L'/2}(\mathcal{F}_3(z')-\frac{I_3}{L'})(\mathcal{F}_1(z')-\frac{I_1}{L'})dz' \end{aligned} \tag{A.15}$$

In a similar fashion, we can write

$$\frac{\partial\sigma'}{\partial\beta} = \alpha a_2+\beta b_2+\gamma c_2 \tag{A.16}$$

where a_2, b_2, and c_2 are given by equations analogous to Eqns [A.15]

$$\begin{aligned} a_2 = b_1 &\equiv \int_{-L'/2}^{L'/2}(\mathcal{F}_2(z')-\frac{I_2}{L'})(\mathcal{F}_1(z')-\frac{I_1}{L'})dz' \\ b_2 &\equiv \int_{-L'/2}^{L'/2}\left(\mathcal{F}_2(z')-\frac{I_2}{L'}\right)^2 dz' \\ c_2 &\equiv \int_{-L'/2}^{L'/2}(\mathcal{F}_3(z')-\frac{I_3}{L'})(\mathcal{F}_2(z')-\frac{I_2}{L'})dz' \end{aligned} \tag{A.17}$$

The coefficients a_1, b_1, c_1, a_2, b_2, and c_2 may all be determined through numerical integration, once the coil radius, coil length, and length of interest (namely, R, L,

and L') are chosen.

Using Eqns [A.13, A.14, A.16], we can solve for α and β in terms of γ:

$$\begin{aligned} \alpha &= \frac{-\gamma}{a_1}\left[c_1 + \left(\frac{a_1c_2 - a_2c_1}{a_2b_1 - b_2a_1}\right)b_1\right] \\ \beta &= \gamma\left(\frac{a_1c_2 - a_2c_1}{a_2b_1 - b_2a_1}\right) \end{aligned} \tag{A.18}$$

A.3 Examples

A.3.1 Coil X-1

For the persistence experiments at the Omega/CSI 4.7 T horizontal bore magnet at the Brigham and Women's Hospital, the sample cell (containing ^{129}Xe gas) is a glass cylinder, roughly 2.5 cm in diameter and 10 cm long. "Coil X-1", the first coil made using the calculations presented here, was based on the following parameters:

$$\begin{aligned} R &= 1.6 \text{ cm} \\ L = L' &= 15 \text{ cm} \\ \gamma &= 4.94739 \text{ radians/cm} \end{aligned}$$

The magnet bore diameter, with gradient coils and an RF shield inserted, restricts the length of the transversely placed solenoid coil to under 18 cm; thus a length of 15 cm is chosen for convenience. The value of γ is equivalent to 2 turns per inch, and is roughly the same as a similar coil I had been using that John Montalbano made for me. This turn density was known to allow the coil to be tuned to 55.38 MHz (the resonance frequency of ^{129}Xe) while requiring a reasonably low amount of capacitance. Table A.1 lists the resulting values given the above parameters.

Figure A.1 shows a plot of $\mathcal{F}$(z') (Eqn [A.7]) over the length of the coil L; Figure

a_1	=	1.33386×10^6	a_2	=	29109.2
b_1	=	29109.2	b_2	=	680.556
c_1	=	-327.5	c_2	=	-6.12894
α	=	0.00364136	σ'	=	0.031568
β	=	-0.111196			
γ	=	4.94739			

Table A.1: Calculated values for $L = L' = 15$ cm, $R = 1.6$ cm, $\gamma = 4.94739$ rad/cm.

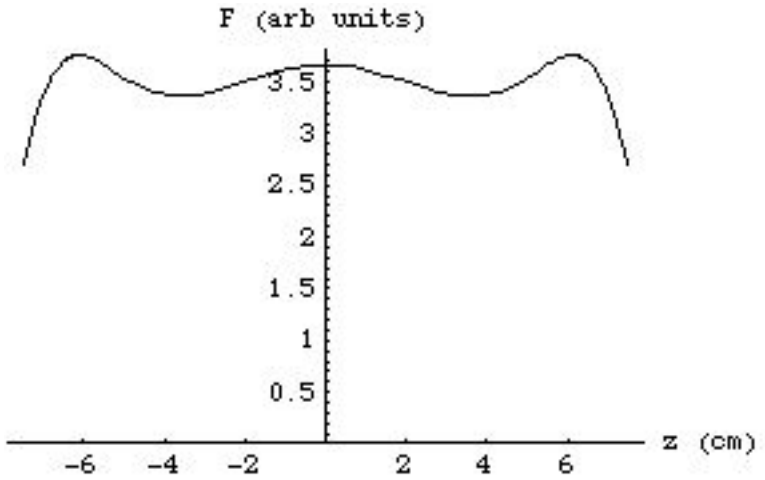

Figure A.1: Optimized field profile $\mathcal{F}(z')$ for $L = L' = 15$ cm, $R = 1.6$ cm, $\gamma = 4.94739$ rad/cm.

A.2 shows a plot of the parameter $\phi(z')$ (Eqn [A.4]) given the calculated values of α, β, and γ.

A.3.2 Coil X-2

As another illustration, I include the calculations for the same parameters, except that the length L' over which the σ' is minimized has been reduced to 11 cm, reflecting the fact that the Xe sample cells are in fact slightly shorter than the coil's total length (of 15 cm). By using $L' < L$, it is possible to achieve a much more uniform field over the desired length L', as we shall see below. "Coil X-2" is the coil

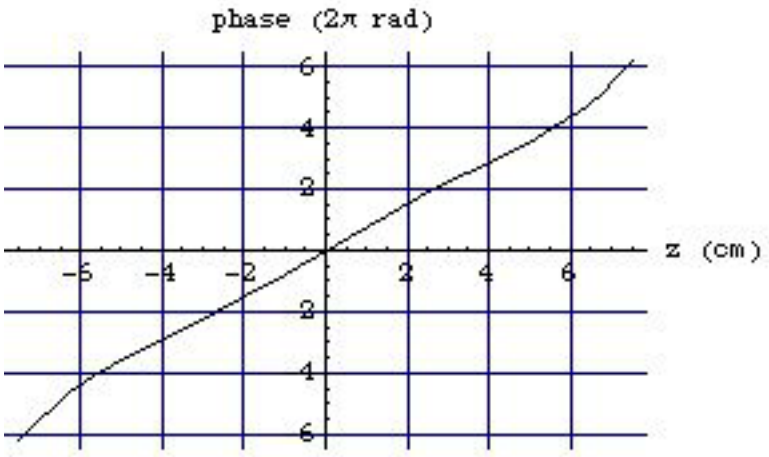

Figure A.2: Optimized $\phi(z')$ for $L = L' = 15$ cm, $R = 1.6$ cm, $\gamma = 4.94739$ rad/cm.

a_1	=	357748	a_2	=	10454.7
b_1	=	10454.7	b_2	=	316.258
c_1	=	-35.7632	c_2	=	-1.0235
α	=	0.000786011	σ'	=	0.000047
β	=	-0.00997243			
γ	=	4.94739			

Table A.2: Calculated values for $L = 15$ cm, $L' = 11$ cm, $R = 1.6$ cm, $\gamma = 4.94739$ rad/cm.

we built according to the calculations in this section.

A.4 Other practical considerations

This section includes some practical notes for using the calculations presented here to construct an RF solenoid coil. Examples from coil X-2 are included.

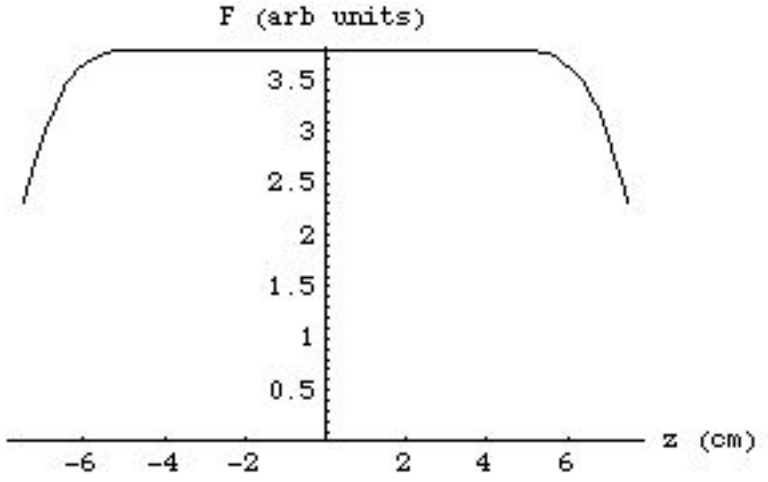

Figure A.3: Optimized field profile $\mathcal{F}(z')$ for $L = 15$ cm, $L' = 11$ cm, $R = 1.6$ cm, $\gamma = 4.94739$ rad/cm.

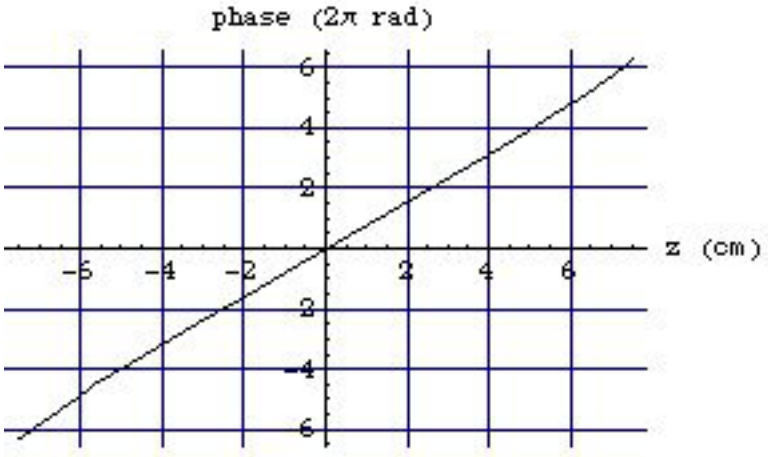

Figure A.4: Optimized $\phi(z')$ for $L = 15$ cm, $L' = 11$ cm, $R = 1.6$ cm, $\gamma = 4.94739$ rad/cm.

A.4.1 Winding the coil

To wind a solenoid coil in accordance with the calculations made in section A.3, we wrote a macro for TurboCAD[2] running on an Apple Macintosh computer. The macro is listed below:

```
{ TurboCad macro for drawing a coil winding pattern }
{ used for Persistence Measurement expt }
{ gpw, 10/28/99 }
{ based on a phase equation given by alpha/5*z^5 + beta/3*z^3 + gamma*z }
{ where alpha, beta, gamma are determined elsewhere, and are functions }
{ of both the coil radius R and length L of the solenoid }

&pi = 3.1415927
&twopi = 2 * &pi;

{ the following would give a constant pitch winding of }
{ 2 turns/inch = 0.7874 turns/cm }
&gamma = 4.94739
{ in units radians/cm }

{ the following are determined from &gamma and assuming R=1.6 cm, L=15 cm }
{ L' = 11 cm }
&alpha = 0.000786011
&beta = -0.00997243

&length = 15
&radius = 1.6
&xoffset = 10
&yoffset = 10

{ set work units to cm }
SETUP Work=cm

&zincr = .01;
&zz = -(&length/2);

LOOP_TOP:
        &phi = &alpha/5*(&zz**5) + (&beta/3)*(&zz**3) + (&gamma)*(&zz);
```

[2]ver. 3, IMSI, 1895 Francisco Blvd. East, San Rafael, CA 94901.

```
&psi = MOD(&phi &twopi)
&sign = 1
if (&psi < 0), &sign = -1
if ((&sign * &psi) > &pi), &psi = &psi - (&sign*(2 * &pi))

Point marker=period [a,(&zz + &xoffset),((&radius * &psi) + &yoffset),0,‘ ‘]
[a,(&zz + &xoffset),((&radius * &psi) + &yoffset),0,‘;‘]
&zz = &zz + &zincr
```

if (&zz < (&length/2)), GOTO LOOP_TOP:

return

Figure A.5 shows a plot that this macro produced; to use it, we printed it and were able to overlay it directly on our acrylic solenoid form. By perforating the pattern, we could trace it to the form underneath, and then wind the solenoid using 1/4” copper tape.

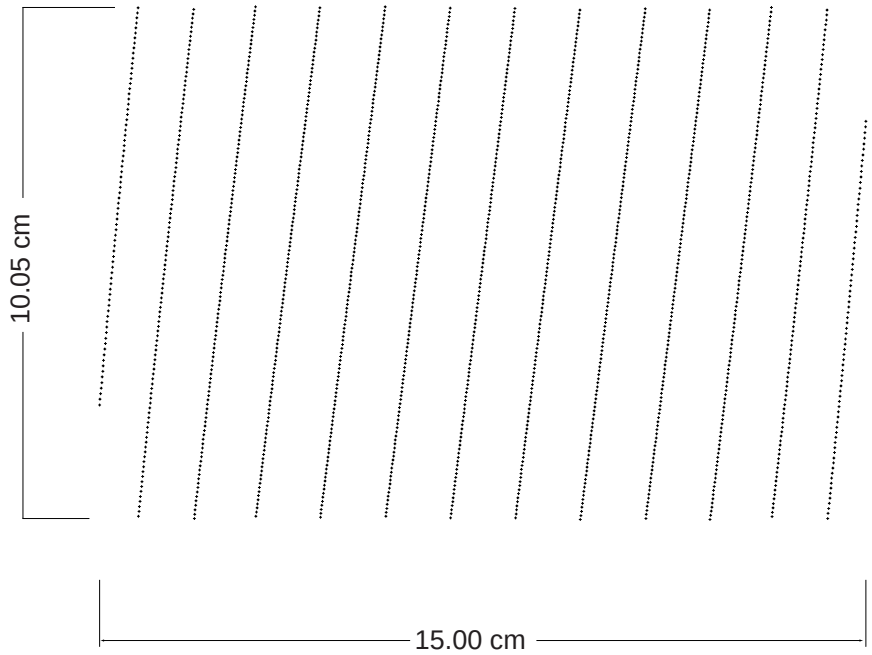

Figure A.5: Coil X-2 winding plan. This plot was produced with TurboCAD, assuming L'=11 cm, L=15 cm.

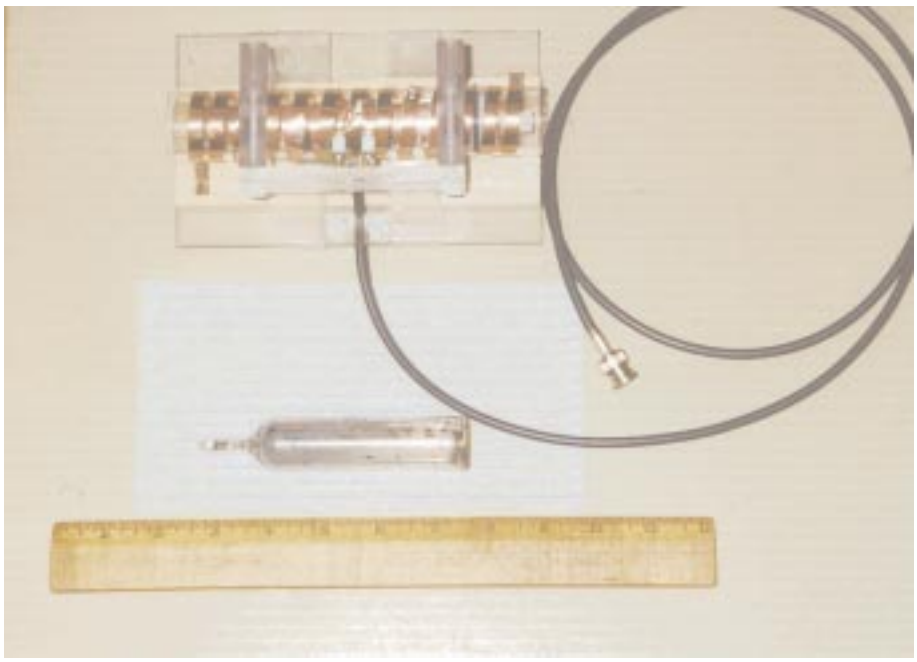

Figure A.6: Photo of Coil X-2. Cell P-2 (3 atm enriched ^{129}Xe, 0.5 atm N_2, Rb) is shown in the foreground, along with a ruler for scale.

A.4.2 Capacitors

Low leakage, non-magnetic capacitors were important for producing a high-Q coil[3]. For tuning and matching the coil, we used Johanson[4] variable capacitors. Chip capacitors by ATC[5] were uniformly distributed along the length of the solenoid (see Fig. A.7). Using these capacitors we achieved a coil Q of ~ 380 (see Fig. A.8).

[3]It is important that they be *non*-magnetic! I struggled with shimming the 4.7 T magnet for a day or two before realizing the coil I had just made used the wrong type of capacitors (they were magnetic).

[4]part no. 5641 (1.0–30 pF) Johanson Mfg. Corp., Rockaway Valley Road, Boonton, NJ 07005

[5]5.6 pF, 22 pF, 47 pF (± 2 pF, 250 VDC), American Technical Ceramics, One Norden Lane, Huntington Station, NY 11746, www.atceramics.com.

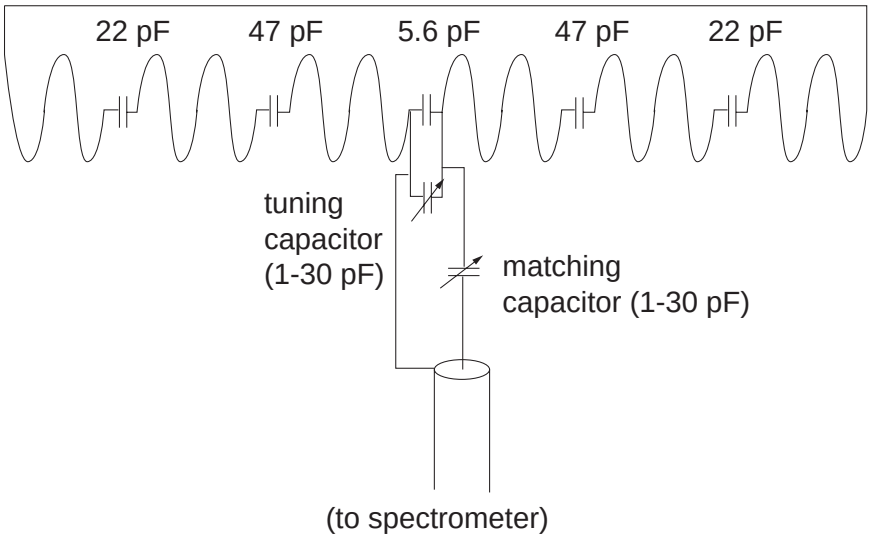

Figure A.7: Schematic for capacitor placement on Coil X-2.

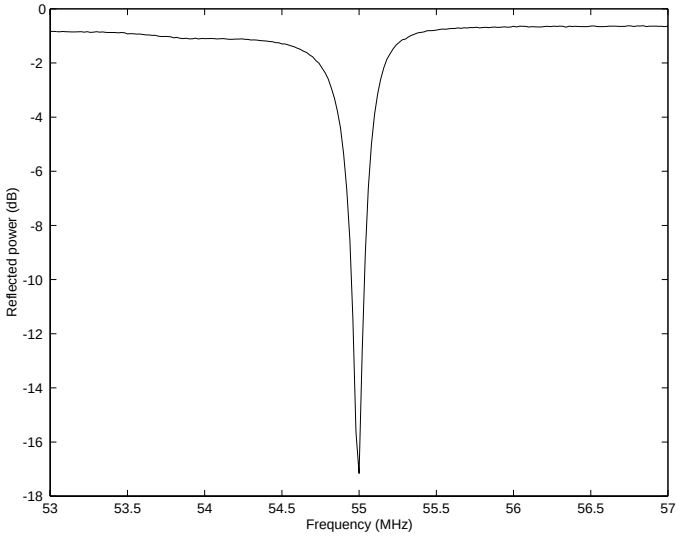

Figure A.8: Tuning plot for Coil X-2. Shown is the reflected power from Coil X-2 as a function of frequency using an HP8712C network analyzer. The *linear* FWHM of the coil resonance at 55 MHz is ≈ 0.145 MHz (note: the plot shown is on a log scale); this gives a Q of ~ 380.

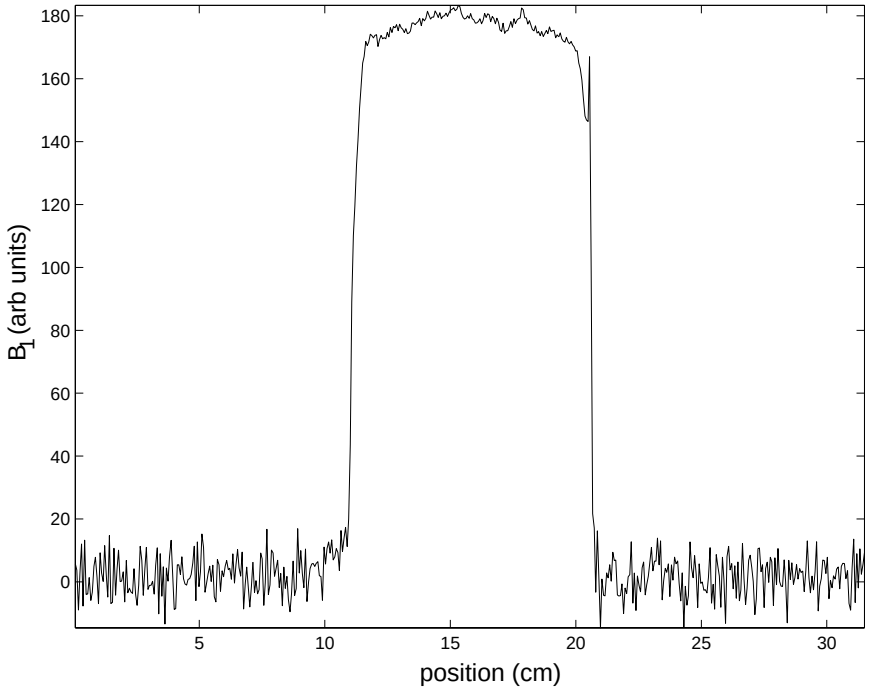

Figure A.9: B_1 (partial) profile for Coil X-2. This is a normalized plot of the B_1 profile for RF Solenoid coil X-2. It was created by taking the 1-D FLASH image of a polarized ^{129}Xe cell ($\sim$ 9 cm cylindrical sample), which is proportional to B_1^2 given a homogeneous sample; the point-wise square root of the image is shown above, and indicates that B_1 varies by at most 5% along the length of the ^{129}Xe sample.

Bibliography

[1] M. A. Bouchiat, T. R. Carver, and C. M. Varnum, Phys. Rev. Lett. **5**, 373 (1960).

[2] G. K. Walters, F. D. Colegrove, and L. D. Schearer, Phys. Rev. Lett. **8**, 439 (1962).

[3] L. D. Schearer, F. D. Colegrove, and G. K. Walters, Phys. Rev. Lett. **10**, 108 (1963).

[4] F. D. Colegrove, L. D. Schearer, and G. K. Walters, Phys. Rev. **132**, 2561 (1963).

[5] R. L. Gamblin and T. R. Carver, Phys. Rev. **138**, A946 (1965).

[6] R. M. Herman, Phys. Rev. **137**, A1062 (1965).

[7] B. C. Grover, Phys. Rev. Lett. **40**, 391 (1978).

[8] W. Happer, Rev. Mod. Phys. **44**, 169 (1972).

[9] W. Happer, E. Miron, S. Schaefer, D. Schreiber, W. A. van Wijngaarden, and X. Zeng, Phys. Rev. A **29**, 3092 (1984).

[10] T. G. Walker and W. Happer, Rev. Mod. Phys. **69**, 629 (1997).

[11] G. C. Phillips, R. R. Perry, P. M. Windham, G. K. . Walters, L. D. Schearer, and F. D. Colegrove, Phys. Rev. Lett. **9**, 502 (1962).

[12] T. E. Chupp, M. E. Wagshul, K. P. Coulter, A. B. McDonald, and W. Happer, Phys. Rev. C **36**, 2244 (1987).

[13] T. E. Chupp and R. J. Hoare, Phys. Rev. Lett. **64**, 2261 (1990).

[14] R. E. Stoner, M. A. Rosenberry, J. T. Wright, T. E. Chupp, E. R. Oteiza, and R. L. Walsworth, Phys. Rev. Lett. **77**, 3971 (1996).

[15] D. Bear, T. E. Chupp, K. Cooper, S. DeDeo, M. Rosenberry, R. E. Stoner, and R. L. Walsworth, Phys. Rev. A **57**, 5006 (1998).

[16] D. Bear, R. E. Stoner, R. L. Walsworth, V. A. Kostelecky, and C. D. Lane, Phys. Rev. Lett. **85**, 5038 (2000).

[17] D. Raftery, H. Long, T. Meersmann, P. J. Grandinetti, L. Reven, and A. Pines, Phys. Rev. Lett. **66**, 584 (1991).

[18] M. S. Albert, G. D. Cates, B. Driehuys, W. Happer, B. Saam, C. S. Springer, Jr., and A. Wishnia, Nature **370**, 199 (1994).

[19] R. W. Mair, G. P. Wong, D. Hoffmann, M. D. Hürlimann, S. Patz, L. M. Schwartz, and R. L. Walsworth, Phys. Rev. Lett. **83**, 3324 (1999).

[20] K. Sakai, A. M. Bilek, E. Oteiza, R. L. Walsworth, D. Balamore, F. a. Jolesz, and M. S. Albert, J. Mag. Res. B **111**, 300 (1996).

[21] S. D. Swanson, M. S. Rosen, K. P. Coulter, R. C. Welsh, and T. E. Chupp, Magn. Reson. Med. **42**, 1137 (1999).

[22] C. H. Tseng, R. W. Mair, G. P. Wong, D. Williamson, D. G. Cory, and R. L. Walsworth, Phys. Rev. E **59**, 1785 (1999).

[23] R. W. Mair, C.-H. Tseng, G. P. Wong, D. G. Cory, and R. L. Walsworth, Phys. Rev. E **61**, 2741 (2000).

[24] G. Navon, Y.-Q. Song, T. Rõõm, S. Appelt, R. E. Taylor, and A. Pines, Science **271**, 1848 (1996).

[25] Y.-Q. Song, B. M. Goodson, R. E. Taylor, D. D. Laws, G. Navon, and A. Pines, Angew. Chemie **36**, 2368 (1997).

[26] S. Peled, C.-H. Tseng, A. A. Sodickson, R. W. Mair, R. L. Walsworth, and D. G. Cory, J. Mag. Res. **140**, 320 (1999).

[27] S. Appelt, A. Ben-Amar Baranda, C. J. Erickson, M. V. Romalis, A. R. Young, and W. Happer, Phys. Rev. A **58**, 1412 (1998).

[28] M. E. Wagshul, Ph.D. thesis, Harvard University, 1991.

[29] M. E. Wagshul and T. E. Chupp, Phys. Rev. A **49**, 3854 (1994).

[30] M. V. Romalis, E. Miron, and G. D. Cates, Phys. Rev. A **56**, 4569 (1997).

[31] E. S. Hrycyshyn and L. Krause, Can. J. Phys. **48**, 2761 (1970).

[32] J. K. Link, J. Opt. Soc. Am. **56**, 1195 (1966).

[33] A. Gallagher, Phys. Rev. **157**, 68 (1967).

[34] B. R. Bulos and W. Happer, Phys. Rev. A **4**, 849 (1971).

[35] X. Zeng, Z. Wu, T. Call, E. Miron, D. Schreiber, and W. Happer, Phys. Rev. A **31**, 260 (1985).

[36] G. D. Cates, R. J. Fitzgerald, A. S. Barton, P. Bogorad, M. Gatzke, N. R. Newbury, and B. Saam, Phys. Rev. A **45**, 4631 (1992).

[37] R. A. Bernheim, J. Chem. Phys. **36**, 135 (1962).

[38] C. C. Bouchiat, M. A. Bouchiat, and L. C. L. Pottier, Phys. Rev. **181**, 144 (1969).

[39] M. A. Bouchiat, J. Brossel, and L. C. Pottier, J. Chem. Phys. **56**, 3703 (1972).

[40] A. Ben-Amar Baranda, S. Appelt, M. V. Romalis, C. J. Erickson, A. R. Young, G. D. Cates, and W. Happer, Phys. Rev. Lett. **80**, 2801 (1998).

[41] Z. Wu, T. G. Walker, and W. Happer, Phys. Rev. Lett. **54**, 1921 (1985).

[42] K. P. Coulter, A. B. McDonald, W. Happer, T. E. Chupp, and M. E. Wagshul, Nucl. Instrum. Methods Phys. Res. **A270**, 90 (1988).

[43] W. A. Fitzsimmons and G. K. Walters, Phys. Rev. Lett. **19**, 943 (1967).

[44] W. A. Fitzsimmons, L. L. tankersley, and G. K. Walters, Phys. Rev. **179**, 156 (1969).

[45] R. S. Timsit, J. M. Daniels, and A. D. May, Can. J. Phys. **49**, 560 (1971).

[46] N. R. Newbury, A. S. Barton, G. D. Cates, w. Happer, and H. Middleton, Phys. Rev. A **48**, 4411 (1993).

[47] T. E. Smith, T. E. Chupp, K. P. Coulter, and R. C. Welsh, Nucl. Instrum. Methods Phys. Res. **A402**, 247 (1998).

[48] X. Zeng, E. Miron, W. A. van Wijngaarden, D. Schreiber, and W. Happer, Phys. Lett. **96A**, 191 (1983).

[49] B. Driehuys, G. D. Cates, and W. Happer, Phys. Rev. Lett. **74**, 4943 (1995).

[50] L. D. Schearer and G. K. Walters, Phys. Rev. **139**, A1398 (1965).

[51] G. D. Cates, S. R. Schaefer, and W. Happer, Phys. Rev. A **37**, 2877 (1988).

[52] T. J. Killian, Phys. Rev. **27**, 578 (1926).

[53] *Oxford English Dictionary*, 2nd ed., edited by J. A. Simpson and E. S. C. Weiner (Oxford University Press, New York, New York, 1989).

[54] C. B. Alcock, V. P. Itkin, and M. K. Horrigan, Can. Metal. Quar. **23**, 309 (1984).

[55] *CRC Handbook of Chemistry and Physics*, 75th ed., edited by D. R. Lide (CRC Press, Inc., Boca Raton, Florida 33431, 1994).

[56] D. K. Walter, W. M. Griffith, and W. Happer, in *Bulletin of the American Physical Society*, No. 3 in *II* (American Institute of Physics, Melville, NY, 2000), p. 64.

[57] W. J. Cummings, O. Häusser, W. Lorenzon, D. R. Swenson, and B. Larson, Phys. Rev. A **51**, 4842 (1995).

[58] D. F. Phillips, G. P. Wong, D. Bear, R. E. Stoner, and R. L. Walsworth, Rev. Sci. Instrum. **70**, 2905 (1999).

[59] V. R. Pomeroy, Ph.D. thesis, University of New Hampshire, 1998.

[60] E. R. Oteiza, Ph.D. thesis, Harvard University, 1992.

[61] M. S. Rosen, Ph.D. thesis, The University of Michigan, 2001.

[62] S. R. Breeze, S. Lang, I. Moudrakovski, C. I. Ratcliffe, J. A. Ripmeester, G. Santyr, B. Simard, and I. Zuger, J. Appl. Phys. **87**, 8013 (2000).

[63] L.-H. Lee, J. Coll. Interface Sci. **27**, 751 (1968).

[64] J. Sagiv, J. Am. Chem Soc. **102**, 92 (1980).

[65] J. A. Fedchak, P. Cabauy, W. J. Cummings, C. E. Jones, and R. S. Kowalczyk, Nucl. Instrum. Methods Phys. Res. **A 391**, 405 (1997).

[66] J. Sagiv, Israel J. Chem. **18**, 346 (1979).

[67] C. P. Slichter, *Principles of Magnetic Resonance*, 3rd ed. (Springer, Berlin, 1996).

[68] C. Cohen-Tannoudji, B. Diu, and F. Laloë, *Quantum Mechanics* (Hermann and John Wiley & Sons, Paris, France, 1977).

[69] E. L. Hahn, Phys. Rev. **80**, 580 (1950).

[70] A. Abragam, *The Principles of Nuclear Magnetism* (Clarendon Press, Oxford, 1961).

[71] *Biomedical magnetic resonance imaging : principles, methodology, and applications*, edited by F. W. Wehrli, D. Shaw, and J. B. Kneeland (VCH, New York, 1988).

[72] P. T. Callaghan, *Principles of Nuclear Magnetic Resonance Microscopy* (Clarendon Press, Oxford, 1991).

[73] R. R. Ernst, C. Bodenhausen, and A. Wokaun, *Principles of Nuclear Magnetic Resonance in One and Two Dimensions* (Clarendon Press, Oxford, 1987).

[74] R. L. Vold, J. S. Waugh, M. P. Klein, and D. E. Phelps, J. Chem. Phys. **48**, 3831 (1968).

[75] R. W. Mair, D. Hoffmann, S. A. Sheth, G. P. Wong, J. P. Butler, S. Patz, G. P. Topulos, and R. L. Walsworth, NMR in Biomed. **13**, 229 (2000).

[76] E. O. Stejskal and J. E. Tanner, J. Chem. Phys. **42**, 288 (1965).

[77] L. L. Latour, L. Li, and C. H. Sotak, J. Mag. Res. B **101**, 72 (1993).

[78] R. W. Mair, D. G. Cory, S. Peled, C.-H. Tseng, S. Patz, and R. L. Walsworth, J. Mag. Res. **135**, 478 (1998).

[79] G. R. Davies, T. K. Halstead, R. C. Greenhow, and K. J. Packer, Chem. Phys. Lett. **230**, 237 (1994).

[80] D. M. Schmidt, J. S. George, S. I. Penttila, A. Caprihan, and E. Fukushima, J. Mag. Res. **129**, 184 (1997).

[81] I. E. Dimitrov, S. R. Charagundla, R. Rizi, R. Reddy, and J. S. Leigh, Magn. Res. Imag. **17**, 267 (1999).

[82] A. Haase, J. Frahm, D. Matthaei, W. Hänicke, and K.-D. Merboldt, J. Mag. Res. **67**, 258 (1986).

[83] W. A. Edelstein, J. M. S. Hutchison, G. Johnson, and T. Redpath, Phys. Med. Biol. **25**, 751 (1980).

[84] L. Zhao and M. S. Albert, Nucl. Instrum. Methods **A 402**, 454 (1998).

[85] P. G. Morris, *NMR Imaging in Biology and Medicine* (Clarendon, Oxford, 1986).

[86] S. A. Engel, D. E. Rumelhart, B. A. Wandell, A. T. Lee, G. H. Glover, E.-J. Chichilnisky, and M. N. Shadien, Nature **369**, 525 (1994).

[87] E. E. Ehrichs, H. M. Jaeger, G. S. Karczmar, J. B. Knight, V. Y. Kuperman, and S. R. Nagel, Science **267**, 1632 (1995).

[88] C. P. Gonatas, J. S. Leigh, and A. G. Yodh, Phys. Rev. Lett. **75**, 573 (1995).

[89] Conventional MRI systems have been operated at magnetic fields as low as 160 G using a simple, low-cost electromagnet [see G.C. do Nascimento, R.E. de Souza, and M. Engelsberg, J. Phys. E **22**, 774 (1989); G. C. do Nascimento, M. Engelsberg, and R. E. de Souza, Measur. Sci. Tech. **3**, 370 (1992)]. However, the inherently low thermal spin polarization attainable at such magnetic fields leads to lower image resolution and greater data acquisition times, and is not feasible for gas-phase MRI without laser polarization.

[90] ^{3}He can be laser polarized using either of two techniques: spin-exchange optical pumping [see the recent review article T. G. Walker and W. Happer, Rev. Mod. Phys. **69**, 629 (1997)], or metastability exchange optical pumping [see, e.g., G. Eckert *et al.*, Nucl. Instrum. Methods Phys. Res., Sect. A **320**, 53 (1992)]. ^{129}Xe can be effectively laser polarized using only the first of these techniques. All optical pumping methods have their origin in the work of Kastler and co-workers in the 1950s [see the classic review article W. Happer, Rev. Mod. Phys. **44**, 169 (1972)].

[91] J. R. MacFall and et al., Radiology **200**, 553 (1996).

[92] M. Ebert and et al., Lancet **347**, 1297 (1996).

[93] P. Bachert, L. R. Schad, M. Bock, M. v. Knopp, M. Ebert, T. Großman, W. Heil, D. Hofmann, R. Surkau, and E. W. Otten, Magn. Reson. Med. **36**, 192 (1996).

[94] H. U. Kauczor and et al., Radiology **201**, 564 (1996).

[95] J. P. Mugler and et al., Magn. Reson. Med. **37**, 809 (1997).

[96] Currently, laser polarized noble gas MRI is being tested as a diagnostic tool for chronic obstructive pulmonary disease (COPD), the fourth leading cause of death in the United States. The production of laser polarized noble gas is being commercialized [e.g., by Magnetic Imaging Technologies, Inc., 2500 Meridian Parkway, Suite 175, Durham, NC 27713].

[97] F. G. Shellock, S. Morisoli, and E. Kanal, Radiology **189**, 587 (1993).

[98] Y. S. Greenberg, Rev. Mod. Phys. **70**, 175 (1998).

[99] R. D. Black and et al., Radiology **199**, 867 (1996).

[100] A. Bifone and et al, Proc. Natl. Acad. Sci. U.S.A. **93**, 12932 (1996).

[101] S. Peled and et al., Magn. Reson. Med. **36**, 340 (1996).

[102] M. E. Wagshul and et al, Magn. Reson. Med. **36**, 183 (1996).

[103] B. M. Goodson and et al., Proc. Natl. Acad. Sci. U.S.A. **94**, 14725 (1997).

[104] Y.-Q. Song, H. C. Gaege, T. Pietrass, G. A. Barrall, G. C. Chingas, M. R. Ayers, and A. Pines, J. Mag. Res. A **115**, 127 (1995).

[105] K. L. Sauer, R. J. Fitzgerald, and W. Happer, Chem. Phys. Lett. **277**, 153 (1997).

[106] T. E. Chupp, R. J. Hoare, R. L. Walsworth, and B. Wu, Phys. Rev. Lett. **72**, 2363 (1994).

[107] Researchers at Princeton have previously reported 1D low-field NMR images of laser polarized ^{3}He gas: B. Saam, N. Drukker, and W. Happer, Chem. Phys. Lett. **263**, 481 (1996). Also scientists in France are pursuing MRI of laser polarized ^{3}He gas in human lungs at 0.1 T: L. Darrasse, G. Guillot, P.-J. Nacher, and G. Tastevin, C.R. Acad. Sci. Paris, Ser. IIb **324**, 691 (1997); L. Darrasse, G. Guillot, P.-J. Nacher, and G. Tastevin, Proc. Int. Soc. Magn. Reson. Meet., 6th Meeting, 449 (1998).

[108] R. J. Hanson and F. M. . Pipkin, Rev. Sci. Instrum. **36**, 179 (1965).

[109] J. M. Blackledge, *Quantitative Coherent Imaging* (Academic Press, London, 1989).

[110] P. T. Callaghan and C. D. Eccles, J. Mag. Res. **78**, 1 (1988).

[111] For example, at room temperature the molecular diffusion coefficient of liquid water is 1.7 $\times 10^{-2}$ cm^{2}s^{-1} and the ^{3}He gas self-diffusion coefficient is 1.8 cm^{2}s^{-1}.

[112] R. Surkau, P. Bachert, M. Bock, M. Ebert, T. Grossmann, W. Heil, D. Hofmann, H. U. Kauczor, K. F. Frietner, M. Leduc, E. W. Otten, T. Roberts, and M. Thelen, in *Proc. Intl. Soc. Magn. Reson. Med. 5th Sci. Meeting* (ISMRM, Vancouver, 1997), p. 182.

[113] X. J. Chen, M. S. Chawla, G. Cates, and C. P. Cofer, in *Proc. Intl. Soc. Magn. Reson. Med. 5th Sci. Meeting* (ISMRM, Vancouver, 1997), p. 2108.

[114] For a review, see H.-U. Kauczor, R. Surkau, and T. Roberts, *Eur. Radiol.* **8**, 820–827 (1998) and references therein.

[115] G. Eckert, W. Heil, M. Meyerhoff, E. W. Otten, R. Surfaku, M. Werner, M. Leduc, P. J. Nacher, and L. D. Schearer, Nucl. Instrum. Methods Phys. Res. **A 320**, 53 (1992).

[116] L. Darrasse, G. Guillot, P.-J. Nacher, and G. Tastevin, in *Proc. Intl. Soc. Magn. Reson. Med. 6th Sci. Meeting* (ISMRM, Sydney, 1998), p. 449.

[117] B. Saam, N. Drukker, and W. Happer, Chem. Phys. Lett. **263**, 481 (1996).

[118] M. P. Augustine, A. Wong-Foy, J. L. Yarger, M. Tomaselli, A. Pines, D. M. T. That, and J. Clarke, Appl. Phys. Lett. **72**, 1908 (1998).

[119] C. H. Tseng, G. P. Wong, V. R. Pomeroy, R. W. Mair, D. P. Hinton, D. Hoffmann, R. E. Stoner, F. W. Hersman, D. G. Cory, and R. L. Walsworth, Phys. Rev. Lett. **81**, 3785 (1998).

[120] X. J. Chen, M. S. Chawla, G. P. Cofer, L. W. Hedlund, H. E. Möller, and G. A. Johnson, Magn. Reson. Med. **40**, 61 (1998).

[121] D. I. Hoult and R. E. Richards, J. Mag. Res. **24**, 71 (1976).

[122] P. T. Callaghan, C. D. Eccles, T. G. Haskell, P. J. Langhorne, and J. D. Seymour, J. Mag. Res. **133**, 148 (1998).

[123] A. Mohoric, J. Stepisnik, M. Kos, and G. Planinsic, J. Mag. Res. **136**, 22 (1999).

[124] R. A. Waggoner and E. Fukushima, Magn. Res. Imag. **14**, 1085 (1996).

[125] D. J. Griffiths, *Introduction to Electrodynamics*, 2nd ed. (Prentice Hall, New Jersey, 1989).

[126] N. Bloembergen and R. V. Pound, Phys. Rev. **95**, 8 (1954).

[127] H. G. Robinson and T. Myint, Appl. Phys. Lett. **5**, 116 (1964).

[128] G. P. Wong, R. W. Mair, R. L. Walsworth, and D. G. Cory, Phys. Rev. Lett. **86**, 4156 (2001).

[129] S. N. Majumdar, C. Sire, A. J. Bray, and S. J. Cornell, Phys. Rev. Lett. **77**, 2867 (1996).

[130] B. Derrida, V. Hakim, and R. Zeitak, Phys. Rev. Lett. **77**, 2871 (1996).

[131] T. J. Newman and Z. Toroczkai, Phys. Rev. E **58**, R2685 (1998).

[132] B. Derrida, A. Bray, and C. Godrèche, J. Phys. A. **27**, L357 (1994).

[133] B. Derrida, V. Hakim, and V. Pasquier, Phys. Rev. Lett. **75**, 751 (1995).

[134] S. N. Majumdar and C. Sire, Phys. Rev. Lett. **77**, 1420 (1996).

[135] S. N. Majumdar, A. Bray, S. Cornell, and C. Sire, Phys. Rev. Lett. **77**, 3704 (1996).

[136] S. N. Majumdar and A. J. Bray, Phys. Rev. Lett. **81**, 2626 (1998).

[137] C. Sire, S. N. Majumdar, and A. Rüdinger, Phys. Rev. E **60**, 1258 (2000).

[138] V. M. Kendon, M. E. Cates, and J.-C. Desplat, Phys. Rev. E **61**, 4029 (2000).

[139] M. Marcos-Martin, D. Beysens, J. P. Bouchaud, C. Godrèche, and I. Yekutieli, Physica A **214**, 396 (1995).

[140] B. Yurke, A. N. Pargellis, S. N. Majumdar, and C. Sire, Phys. Rev. E **56**, R40 (1997).

[141] W. Y. Tam, R. Zeitak, K. Y. Szeto, and J. Stavans, Phys. Rev. Lett. **78**, 1588 (1997).

[142] A. J. Bray, Adv. Phys. **32**, 357 (1994).

[143] A. Bray, B. Derrida, and C. Godrèche, Eur. Phys. Lett. **27**, 175 (1994).

[144] B. Derrida, P. M. C. de Oliveira, and D. Stauffer, Physica A **224**, 604 (1996).

[145] J. Krug, H. Kallabis, S. N. Majumdar, S. J. Cornell, A. J. Bray, and C. Sire, Phys. Rev. E **56**, 2702 (1997).

[146] B. P. Lee and A. D. Rutenberg, Phys. Rev. Lett. **79**, 4842 (1997).

[147] C. M. Newman and D. L. Stein, Phys. Rev. Lett. **82**, 3944 (1999).

[148] S. Jain, Phys. Rev. E **60**, R2445 (1999).

[149] A. J. Bray, Phys. Rev. E **62**, 103 (2000).

[150] We used a wall coating of octadecyltrichlorosilane (OTS) to reduce Xe-wall interactions and hence increase longitundinal relaxation times.

[151] A more detailed description of the NMR pulse sequence used in this experiment will be presented elsewhere.

[152] W. H. Press, B. P. Flannery, S. A. Teukolsky, and W. T. Vetterling, *Numerical Recipes in C* (Cambridge University Press, Cambridge, U.K., 1988).

[153] C. B. Ahn and Z. H. Cho, IEEE Trans. Med. Imag. **MI-6**, 32 (1987).

[154] S. N. Majumdar, Curr. Sci. **77**, 370 (1999).

[155] J. Hennig, J. Mag. Res. **78**, 397 (1988).

[156] A. Sodickson and D. G. Cory, Prog. Nucl. Magn. Res. Spec. **33**, 77 (1998).

[157] K. L. Sauer, R. J. Fitzgerald, and W. Happer, Phys. Rev. A **59**, R1746 (1999).

[158] S. R. Hartmann and E. L. Hahn, Phys. Rev. **128**, 2042 (1962).

[159] K. L. Sauer, Ph.D. thesis, Princeton University, 1998.

[160] P. R. Bevington and D. K. Robinson, *Data Reduction and Error Analysis for the Physical Sciences*, 2nd ed. (McGraw-Hill, Inc., New York, 1992).

[161] R. E. Jacob, S. W. Morgan, and B. Saam, in *2001 Meeting of the Division of Atomic, Molecular, and Optical Physics* (APS, London, Ontario, 2001), p. B2.009.